Actin-like filament A (AlfA) and AlfA-driven plasmid segregation

Gulsima Dilek Usluer

A dissertation

submitted in partial fulfillment of the

requirements for the degree of

Doctor of Philosophy

University of Washington

2018

Reading Committee:

Justin M. Kollman, Chair

Linda Wordemann

Frank DiMaio

Program Authorized to Offer Degree:

Biochemistry

University of Washington

Abstract

Actin-like filament A (AlfA) and AlfA-driven plasmid segregation

Gulsima Dilek Usluer

Chair of the Supervisory Committee:

Justin M. Kollman, PhD.

Biochemistry

For a long time, the cytoskeleton was considered an exclusive feature of eukaryotic cells. In 1992, it was proposed that bacteria might contain actin and tubulin homologs. Cell biology and structural biology research within the last two decades led to a paradigm shift in our understanding of the cytoskeleton. Discovery of actin and tubulin homologs in bacteria that can form filaments upon nucleotide binding and their involvement in various cellular processes including cell shape determination, cell division, and DNA segregation led to a reconsideration of the evolutionary history of life. Actin-like filament A (AlfA) is a bacterial actin involved in plasmid segregation in *Bacillus subtilis natto*, and it is encoded by plasmid pLS32. In this dissertation, I investigate AlfA and the AlfA-driven segregation system, which is composed of the cytomotive AlfA filaments, the DNA-binding protein AlfB and the centromeric DNA sequence *parN*. We obtained a near-atomic resolution structure of an AlfA filament in the

presence of AMP-PNP using cryo-electron microscopy (cryo-EM). We built an atomic model based on the electron density map and the sequence information to reveal the atomic details of filament formation. Sequence analysis suggested that AlfA is missing the canonical actin subdomain IIB, which we confirmed by our atomic model. Lack of subdomain IIB is compensated by increased lateral interaction surface area, which we confirmed by both cryo-EM and hydrogen-deuterium exchange mass spectrometry (HDX-MS). A comparison of AlfA structure with other actins revealed a unique nucleotide binding conformation, which causes AlfA to remain stable after nucleotide hydrolysis. In addition to the filament structure, we reconstituted the segresome (centromeric DNA-adaptor protein) complex *in vitro* and used it as a tool to investigate AlfA-AlfB interactions. We found that the segresome nucleates AlfA at low stoichiometric ratios while free AlfB increases the effective critical concentration by sequestering AlfA monomers. However, we found that both the segresome and free AlfB can prevent AlfA polymerization at the equimolar ratio and high stoichiometric ratios, respectively. Our crosslinking results suggest that AlfB interacts with AlfA through the same interaction surface to both sequester AlfA monomers and nucleate AlfA filaments.

TABLE OF CONTENTS

LIST OF FIGURES

LIST OF TABLES

ACKNOWLEDGEMENTS

First, I would like to express my sincere gratitude to my advisor Prof. Justin M. Kollman for being an inspiring scientist, whose research encouraged me to take the risk and travel over 6000 miles to follow his footsteps. I am thankful for his continuous support, patience, motivation, and immense knowledge. His feedback helped me immensely during my research and writing of this thesis. Besides my advisor, I would like to thank the rest of my thesis committee: Prof. Ning Zheng, Prof. Frank DiMaio, Prof. Linda Wordeman and Prof. David Veesler, for their insightful comments, but also for the hard question which stimulated for me to think about my research from various perspectives.

My sincere thanks also go to the previous and current members of Kollman Lab, especially Emeric Charles, Jesse Hensen, Shun Kai Yang, Prof. Julien Bergeron and Dr. Nancy Hom, for their help during my training, stimulating discussions, and all the fun we have had in the last four years. Also, I would like to thank my collaborators, Prof. Miklos Guttman, Alex Zelter and Evelynn Henry for their tremendous help and support. Their generosity and patience allowed me to learn more about different aspects of structural biology and revise my scientific knowledge.

From the very bottom of my heart, I would like to thank my friends Domnita Valeria Rusnac, Lexi Walls, Rachel Hutto, Eleanor Vane, Bobby Langan, Sami Naboulsi, Sean Gillespie, Sean Gagnon and Alex Porter for being there for me not only for the good times, but also for the hard times. They made Seattle home to me and became my family in the United States. I am grateful for all the memories we shared, proud of what they have achieved so far and excited for their accomplishments in the future. I wish I have more space to talk about how great and unique each of them is, but I can simply say that they inspired me to become a better person and a better

scientist. Being an international graduate student was not easy, combining the struggles of living in another country and graduate school. I would like to thank Leyla Welkin, who became my mentor in life and helped me to understand myself and my surroundings better. Moreover, many thanks to my small Turkish family in Seattle including Mediha Sorma, Omer Kazanci, Ece Sonmez, Onur Bakiner and Hazal Ercin for their support and empathy, which made living abroad much more comfortable and fun for me. Besides the support I received in the United States, I am grateful to have my dear, Galip Can Guclu, who showed the biggest support and patience to me while I was writing my thesis. He always found a way to make me laugh, feel stronger and look forward to the future.

I would like to thank University of Washington Department of Biochemistry for providing me all the opportunities to pursue in the field of my interest. Financially, I received support from The Scientific and Technological Research Council of Turkey, which I am honored to be a fellow of.

Last, I would like to thank my mother, Reyhan Usluer, for showing me how strong one can be. I am grateful to have a mother like her, especially when I think about how much she fought for her dreams while being kind and understanding. I learned from her how to keep learning, improve myself and turn the hardest times into the biggest lessons.

CHAPTER I - Introduction

1.1. Brief history of actin and its role in eukaryotic cells

In 1864, William Kühne extracted a viscous protein from muscle using a concentrated salt solution (Szent-Gyorgyi, 2004). Kühne called this protein "myosin" and proposed that myosin causes muscles to be in the rigor state. More than a half-century later, in 1939, Engelhardt and Lyubinova reported this "myosin" protein can bind to adenosine triphosphate (ATP), hydrolyze it and release inorganic phosphate (Huxley, 1974). A few years later, in 1943, Albert Szent-Gyorgyi found that Kuhne's myosin is composed of two distinct proteins that differ in viscosity. After joining Gyorgyi's lab, Bruno Ferenc Straub found that another protein called actin, which is responsible for the high viscosity of myosin (Straub, 1942). Straub developed a method to isolate actin from muscle sample and observed that actin transforms from globular form (G-actin) to filamentous form (F-actin) in the presence of a neutral salt, such as potassium chloride (KCl), or at lower pH (Hall & Jakus, 1946). Later, Straub and Feuer found that actin preparations usually contain ATP and actin utilizes this ATP to drive its polymerization (Straub & Feuer, 1950).

The study published by Thomas Schroeder in 1973 changed the perspective of actin as a protein involved only in muscle contraction. Schroeder confirmed the presence of actin filaments in the contractile ring, which forms at the last stage of cell division to separate the mother cell into two daughter cells (Schroeder, 1973). The discovery of actin in non-muscle cells and fluorescent labeling of actin filaments allowed identification of the cellular functions that involves actin and to follow its dynamics *in vivo* (Lazarides & Weber, 1974; Taylor and Wang, 1978).

Subsequent work has highlighted the central importance of actin and actin-related functions in eukaryotic cells, such as cellular motility, cell-shape determination and organelle positioning. Because actin is one of the most abundant and highly conserved proteins in eukaryotic cells and

involved in so many cellular functions, a better understanding of actin and its functions is an important area of research.

1.2. Actin structure and dynamics

The first crystal structure of actin was solved as a complex with DNAseI in 1990. Kabsch and his colleagues described the topology of globular (G-)actin as composed of two domains that can be divided into two subdomains each (IA, IB, IIA, and IIB) (Figure 1.1A) (Kabsch *et al.*, 1990). The nucleotide binding cleft is located in between domains I and II, located at the center of the monomer (dos Remedios *et al.*, 2003). A notable feature of the structure is a two-stranded "hinge" region at the base of domain II that allows the nucleotide binding cleft to open and close like a "clamshell" (Minehardt *et al.*, 2006).

The adenosine triphosphate (ATP)-dependent switch between G-actin and filamentous (F)-actin is crucial for actin functions within the eukaryotic cell (Figure 1.1). The first step towards actin polymerization is the formation of a nucleus, which is a stable multimer of actin monomers (Firat-Karalar & Welch, 2011). Spontaneous interactions between two actin monomers are fast, but not stable. Addition of a third actin monomer stabilizes the interactions between the molecules and makes the elongation favorable (Sept & McCammon, 2001). Due to the polarity of the filament structure, ATP-bound actin monomers are incorporated into the growing filament from both ends at different rates arising from affinities of monomeric actin for each end. This results in an intrinsic polarity in the filament, in terms of structure and dynamics. The end with a slow-growing rate is called the pointed (minus) end while the fast-growing end is called the barbed (plus) end (Carbadillo-Lopez, 2006). Conformational changes associated with actin polymerization increase the rate of hydrolysis of the gamma phosphate of ATP, which is irreversible (Pollard, 2016).

Following hydrolysis, dissociation of gamma phosphate from the polymerized actin is a very slow, reversible process. However, the affinity of the adenosine diphosphate (ADP)-actin filament for inorganic phosphate is very low. Upon release of inorganic phosphate, ADP-actin undergoes a conformational change that causes ADP-actin to dissociate from the filament ends. Since the pointed end has a slower growth rate than the barbed end, the pointed end has more time to hydrolyze ATP and release ADP-actin monomers back into solution (Bindschadler & McGrath, 2004) (Figure 1.2). There is net assembly of ATP-bound actin at barbed ends and net disassembly of ADP-bound subunits at pointed ends at steady-state. This flux of actin subunits from barbed end to pointed ends is called "treadmilling" (Kirschner, 1980).

In addition to nucleotide binding and hydrolysis, actin dynamics are tightly regulated by the action of a large number of actin-binding proteins (ABP) that can crosslink, nucleate, cleave, bundle, stabilize, or destabilize the filaments (Cooper & Schafer, 2000; Korn *et al.*, 1987; Schmidt & Hall, 1998). Actin-binding proteins can affect polymerization dynamics by directly interacting with either monomeric of filamentous actin (Pollard, 2016). Profilin is a crucial ABP that weakly binds to the barbed end of monomeric actin, preventing elongation from the pointed end while increasing the polymerization rate from the barbed end. Moreover, it catalyzes the exchange of ADP to ATP on actin and increases the concentration of ATP-bound actin that can contribute to elongation (Dominguez & Holmes, 2011). On the other hand, Thymosin-β4 binds to both ends of the actin monomer to cap the nucleotide binding cleft and sequester monomeric actin (Chereau *et al.* 2005). Cofilin is involved in recycling of actin monomers by binding to the sides of ADP-bound actin subunits with high affinity, thus severing the actin filaments (Dominguez & Holmes, 2011). Cofilin function is critical for cellular processes like membrane ruffling and cytokinesis, where rapid actin turnover is needed (Bernstain & Bamburg, 2010). Even though Thymosin-β4

counteracts nucleation by sequestering actin monomers, formin and Arp2/3 are used by eukaryotic cells to nucleate actin filaments and polymerize actin in a controlled manner (Pollard, 2007). Both formin and Arp2/3 are multimeric proteins that bind the sides of existing actin filaments and initiate new filaments from the barbed end of the filament. The Arp2/3 complex tethers the pointed end of the growing filament to the side of the mother filament while formin interacts with the barbed end of the filament and stabilizes actin monomers (Pollard, 2016). Higher order actin structures like microvilli and filopodia require physical connections between the actin filaments, which are provided by a range of crosslinking proteins such as fimbrin and fascin (Otto, 1994).

The various roles played by actin and the complex regulation of its dynamics put high evolutionary constraints on the actin sequence, resulting in actin being one of the most conserved eukaryotic protein sequences (Gunning *et al.*, 2015).

1.3. Discovery of actin homologs in prokaryotes

Before 1990, the presence of a cytoskeleton was thought of as one of the defining features that differentiates eukaryotes from prokaryotes. Bacteria were largely considered as "featureless bags of enzymes" that lack intracellular organization, while eukaryotic cells were known to be complex organisms with intracellular compartments and a dynamic cytoskeleton (Errington, 2003; Howard & Kruse, 2005).

In 1992, Bork and his colleagues developed a structure-based sequence alignment to discover the genes related to actin. They showed the ATPases of different protein families such as actin, hexokinase and hsp70 share similar three-dimensional structures composed of the two domains of similar fold with a large ATP-binding cleft in between the domains, which is called "actin fold' (Bork *et al.*, 1992; Kabsch, 1995). Aligning the structures of these proteins allowed them to probe

the common residues involved in ATP binding and hydrolysis. These residues are distributed in five sequence motifs (phosphate I, phosphate II, connect I, connect II and adenosine) (Figure 1.3). By comparing the amino acid properties of these motifs with other proteins in eukaryotes and prokaryotes, they discovered that proteins FtsA, MreB and StbA (now called ParM) are homologs of actin that exist in bacteria (Bork *et al.*, 1992). The most recent bioinformatics study that applied the same principles of homology search described in Bork's study detected more than 35 subfamilies of bacterial actins with both characterized and uncharacterized functions (Derman *et al.*, 2009).

Apart from the conserved residues of the actin fold, the sequence similarity within the bacterial actin family is quite low (often less than 15% sequence identity) (Derman *et al.*, 2009; Shaevitz & Gitai, 2010). However, both *in vitro* and *in vivo* studies showed that bacterial actins can form filaments in the presence of nucleotide (reviewed in Ozyamak *et al.*, 2013). Unlike in eukaryotes, where a single actin filament serves many functions through interactions with many different adaptors, bacteria evolved different actins for specific cellular functions: determination of cell shape (MreB), cell division (FtsA), organelle positioning (MamK) and DNA segregation (ParM) (Figure 1.4), among others (Garner *et al.*, 2004; Hussain *et al.*, 2018; Komeili *et al.*, 2006).

In addition to the divergence in protein sequence, the quaternary structures of actin homologs are quite different from each other. The variations in filament architectures of actin homologs in prokaryotes include changes in the twist, handedness, strand number and polarity (Figure 1.5) (Ozyamak *et al.*, 2013). ParM, for example, is a well-known actin-like protein that segregates plasmids with assembly dynamics that are similar to tubulin (Garner *et al.*, 2004). Recently solved structures of Crenactin, an archaeal actin involved in cell shape determination, revealed a filament architecture similar to F-actin (Izore *et al.*, 2014). It has been proposed that the variance in the

lateral and longitudinal contacts of actin homologs along the filament are the two parameters important for different filament architectures and dynamic properties observed (Gunning *et al.*, 2015).

The sequence diversity of the bacterial actins reflects a more relaxed evolutionary constraint on bacterial actin homologs, which might be related to the presence of fewer interaction partners for each bacterial actin (Gunning *et al.*, 2015). Like eukaryotic actin binding proteins, prokaryotic actin binding proteins regulate the dynamics and the function of the bacterial actins they interact with. MreB, which is involved in cell shape determination, interacts with the members of the cell wall elongation machinery such as MreC, MreD and RodZ that regulates MreB function (Gayathri, 2017). On the other hand, CbeA and CbtA interact with MreB to stabilize and destabilize MreB filaments, respectively (Tan *et al.*, 2011). Potential interactors of MamK filaments, which are involved in positioning of organelles called magnetosomes, are in the same genomic island as MamK (Draper *et al.*, 2011). MamJ and LimJ have been shown to affect MamK dynamics in vivo. However, it is not clear whether their interactions are direct or via other mediators. While MreB and MamK interact with other proteins to regulate their dynamics and function, FtsA interacts with tubulin-like FtsZ filaments in the divisome ring and other divisome components of the cell membrane (Szwedziak *et al.*, 2012).

1.4. Plasmid segregation systems

In addition to its ability to polymerize into filaments, directed polymerization of actin is essential for its functions that utilize force to move objects. If the polymerization is directed to an object, the growing actin filament will exert a pushing force onto the object. Reversely, depolymerization of the actin filament will apply a pulling force onto the object in the direction of

shortening. By pulling and pushing, actin is able to move objects, such as forming the leading edge during cellular migration and driving the cell membrane forward. In bacteria, a well-known example of actin polymerization directed to an object is the ParM-dependent segregation system that pushes low copy number R1 plasmids to the opposite ends of the mother cell during cell division (Gunning *et al.*, 2015).

Plasmids contain genes both useful for their own maintenance and the host's selective advantage such as initiation and control of plasmid replication, drug resistance, virulence factors, and production of toxins. Successful partitioning of plasmids into daughter cells during cell division is necessary for the reliable inheritance of these genes that provide evolutionary advantages to the host (Austin, 1988; Couturier *et al.*, 1988). A successful partitioning event requires cells to make sure that each daughter cell receives at least one copy of the plasmid. For plasmids that have a high-copy number, partitioning is carried out by the random distribution of the plasmids. However, low-copy number plasmids cannot rely on the random distribution, they must ensure their stable inheritance (Jensen & Gerdes, 1997). Thus, low-copy number plasmids require an active partitioning system. In general, segregation of low-copy number plasmids relies on the plasmid-encoded partitioning loci that include of three components; a force-generating protein, a centromere-binding protein and a centromere-like region on the plasmid (Aylett *et al.*, 2010). Even though they have the same type of components necessary for successful partition, plasmid segregation systems differ from each other based on the type of nucleotide triphosphatase (NTPase) they use (Popp *et al.*, 2010).

The first type of segregation system, type I, includes proteins that are Walker-type ATPases (Schumacher, 2008). Type I segregation systems can be divided into two subtypes, Ia and Ib, depending on the organization of partition loci (Gerdes *et al.*, 2000). In type Ia systems, the

centromere-like region is located downstream of Walker-type ATPase, whereas, in type Ib systems, the centromere-like region is upstream of the ATPase (Ebersbach & Gerdes, 2005). In addition to their roles as motor proteins, type Ia Walker-type ATPases contain an N-terminal helix-turn-helix (HTH) region that helps them to autoregulate the partition operon. In type Ib systems, this role is dedicated to centromere-binding proteins. (Shumacher, 2008).

Type II systems contain actin-like ATPases to segregate plasmids. Among bacterial actins involved in plasmid segregation, ParM is the most extensively studied. ParM forms filaments to segregate low copy number plasmids into opposite poles of the *E. coli* cells and it is encoded by the *par* operon of the R1 plasmid. The genetic organization of the *par* operon is similar to the type Ib system; the centromere-like region is located upstream of the cytomotive filament. Like type Ib segregation systems, the autoregulation of the type II segregations systems is provided by the centromere-binding proteins that can bind to DNA (Jensen & Gerdes, 1997). The majority of the plasmid segregation systems can be classified as either type I or type II. However, recent findings have shown a third type of segregation system encoded by *Bacillus thuringiensis* virulence plasmid pBtoxis that encodes a tubulin-like GTPase instead of an ATPase (Larsen *et al.*, 2007).

Plasmid segregation in bacteria can be described as a two-step process. The first step involves the formation of a nucleoprotein complex between the plasmid DNA and centromere-binding protein, called the segresome or partitioning complex. Most of the centromere-like regions consist of multiple DNA repeats for centromere-binding proteins to bind, but the composition of the centromeric regions are quite different from each other in terms of sequence, the number of repeats, length of each repeat and the spacing between each repeat. Formation of the segresome complex recruits the ctyomotive filament to the plasmids and activates the segregation process, which is the second step of plasmid partition (Ebersbach & Gerdes, 2005; Schumacher, 2008).

1.5. The AlfA-driven plasmid segregation system

Actin-like filament A (AlfA) is another bacterial actin involved in plasmid segregation, encoded by the *alf* operon in *Bacillus subtilis* plasmid pLS32. Like *par* operon, the *alf* operon contains three elements required for plasmid segregation: the actin-like ATPase AlfA, the adaptor protein AlfB, and the centromeric DNA sequence *parN* (Tanaka *et al.,* 2010). Even though they are both actin homologs that function in plasmid segregation, AlfA and ParM are significantly different from each other in terms of filament structure, dynamics and segregation mechanisms (Polka *et al.,* 2009). In the presence of ATP, ParM filaments quickly assemble and disassemble, stochastically alternating between growth and catastrophic disassembly (a process referred to as dynamic instability). ParM disassembly is inhibited upon binding to the ParR/*parC* complex, called the segresome. When both ends of a ParM filament are bound by a segresome, dynamic instability of the filament decreases and unidirectional polymerization of antiparallel ParM filament doublets pushes plasmids to the poles of the cell (Jensen *et al.,* 2003).

Unlike ParM, electron microscopy experiments showed that AlfA forms left-handed, highly twisted filaments that assemble into large bundles under physiological conditions. When observed by total internal reflection fluorescence microscopy (TIRF), AlfA showed bidirectional elongation with no apparent signs of dynamic instability (Polka *et al.,* 2009). Surprisingly, light scattering and electron microscopy results suggested a dual role for AlfB; the adaptor protein AlfB alone strongly inhibits AlfA polymerization and prevents the formation of AlfA filaments while it nucleates filaments when bound to *parN*. It has been shown that the AlfB-*parN* complex binds to one end of the filament and AlfA filaments polymerize unidirectionally. Based on these interactions, a plasmid segregation model for AlfA was proposed, which is largely different than that of ParM: i) AlfB/*parN* complex nucleates and promotes AlfA filament formation below its

critical concentration. ii) The AlfB/*parN* segresome complex remains processively bound to elongating AlfA filaments. iii) Filaments interact laterally to form bundles. iv) Antiparallel bundling of filaments allows them to segregate plasmids to the opposite poles of the cell as they elongate. v) AlfB provides AlfA monomers necessary for elongation of these mixed-polarity bundles by either promoting disassembly of segresome-free filaments or sequestering AlfA monomers. (Figure 1.6) (Polka *et al.*, 2014). However, the molecular mechanisms underlying the formation of dynamically stable filaments and the contradictory behavior of AlfB as an inhibitor or nucleator remained unclear. A high-resolution AlfA filament structure and determination of AlfA-AlfB interaction surfaces is necessary to better understand actin diversity and molecular mechanisms of DNA segregation.

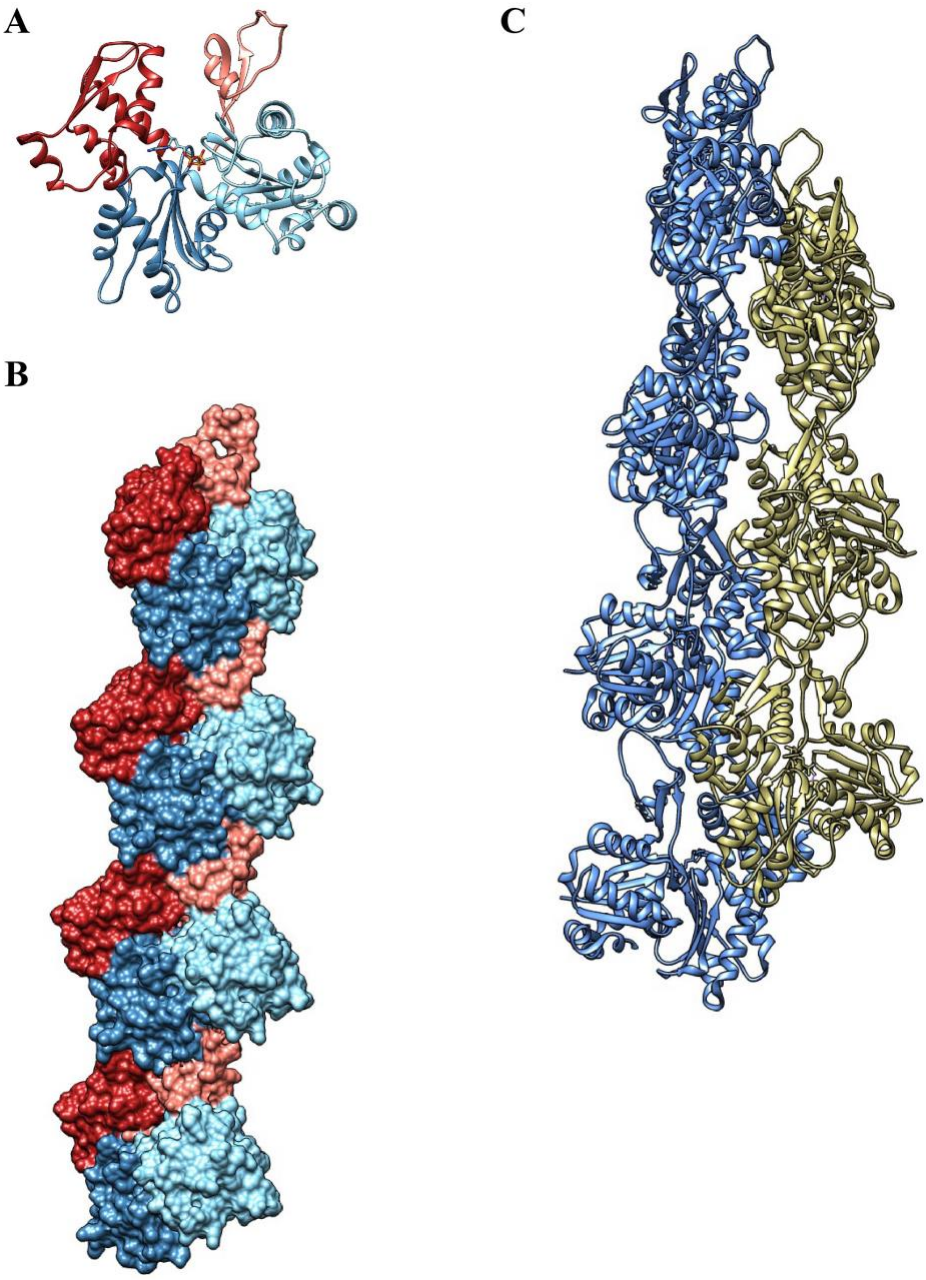

Figure 1.1: Actin monomers can polymerize into right-handed, double-stranded filaments. (A) The crystal structure of G-actin (1ATN) shows the actin fold which composed of two domains of similar fold (domain I and domain II). Each domain can be divided into two subdomains; subdomain IA (light blue), subdomain IB (pink), subdomain IIA (dark blue) and subdomain IIB (red). Actin contains an ATP-binding cleft in between the domains, closer to subdomain IA and IIA. ATP bound to the ATP-binding cleft shown in stick form. (B) Actin protofilament showing the interactions between the protomers. (C) The filament structure of actin (5JLF). Actin forms right-handed, double-stranded polar filaments upon nucleotide binding. Strands are shown in blue and yellow.

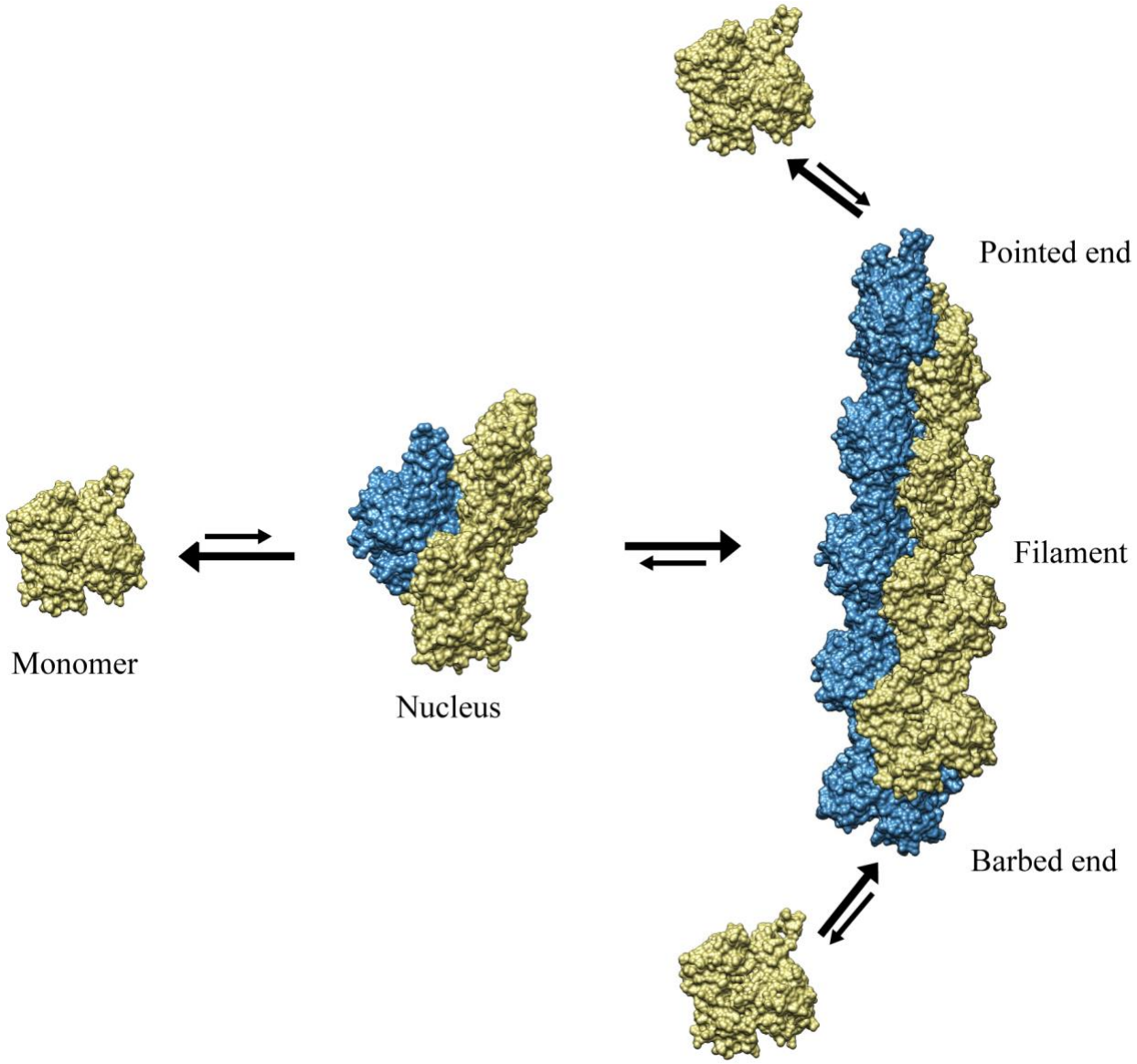

Figure 1.2: Actin polymerization dynamics. Formation of a stable nucleus composed of ATP-bound actin monomers is the rate-limiting step of the actin polymerization. Actin monomers interact spontaneously, but they dissociate faster relative to their association. When a third monomer interacts with an actin dimer, elongation from the nucleus becomes favorable. The intrinsic polarity of an elongating actin filament causes addition and hydrolysis-dependent dissociation of the actin monomers to be at different rates from each end. The pointed end has a smaller growth rate compared to barbed end, which the monomers are incorporated at a faster rate. Arrows are showing the rates of each step relative to each other.

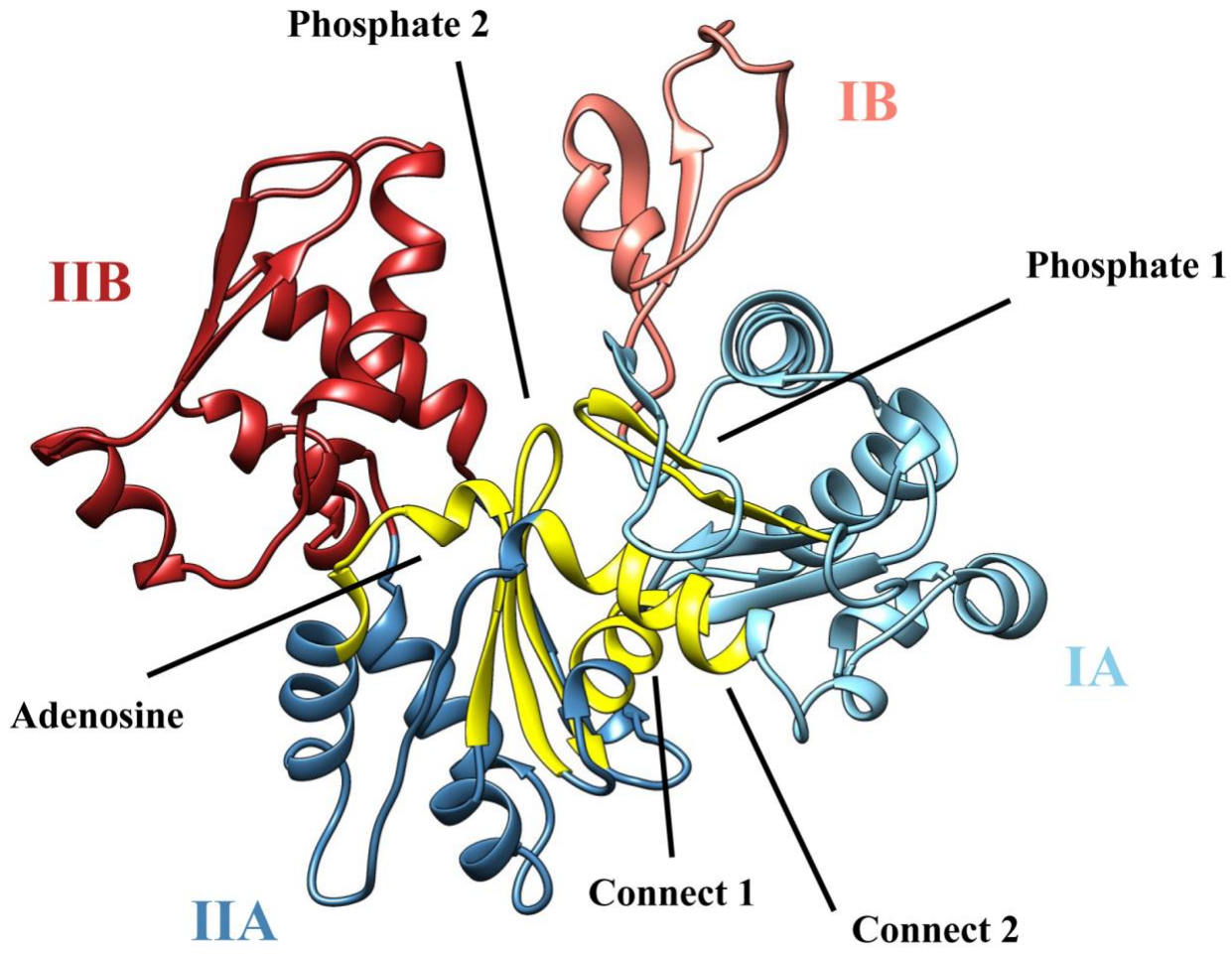

Figure 1.3: Five sequence motifs involved in ATP binding and hydrolysis. ATP binding pocket is located in the cleft between the domain I and II, close to the subdomain IA (dark blue) and IIA (light blue). Five conserved sequence motifs of the ATPases (phosphate 1, phosphate 2, connect 1, connect 2 and adenosine) that are involved in ATP binding and hydrolysis are shown in yellow. Sequence motifs phosphate 1, connect 1 and connect 2 are located in subdomain IA, while adenosine and phosphate 2 motifs are a part of subdomain IIA.

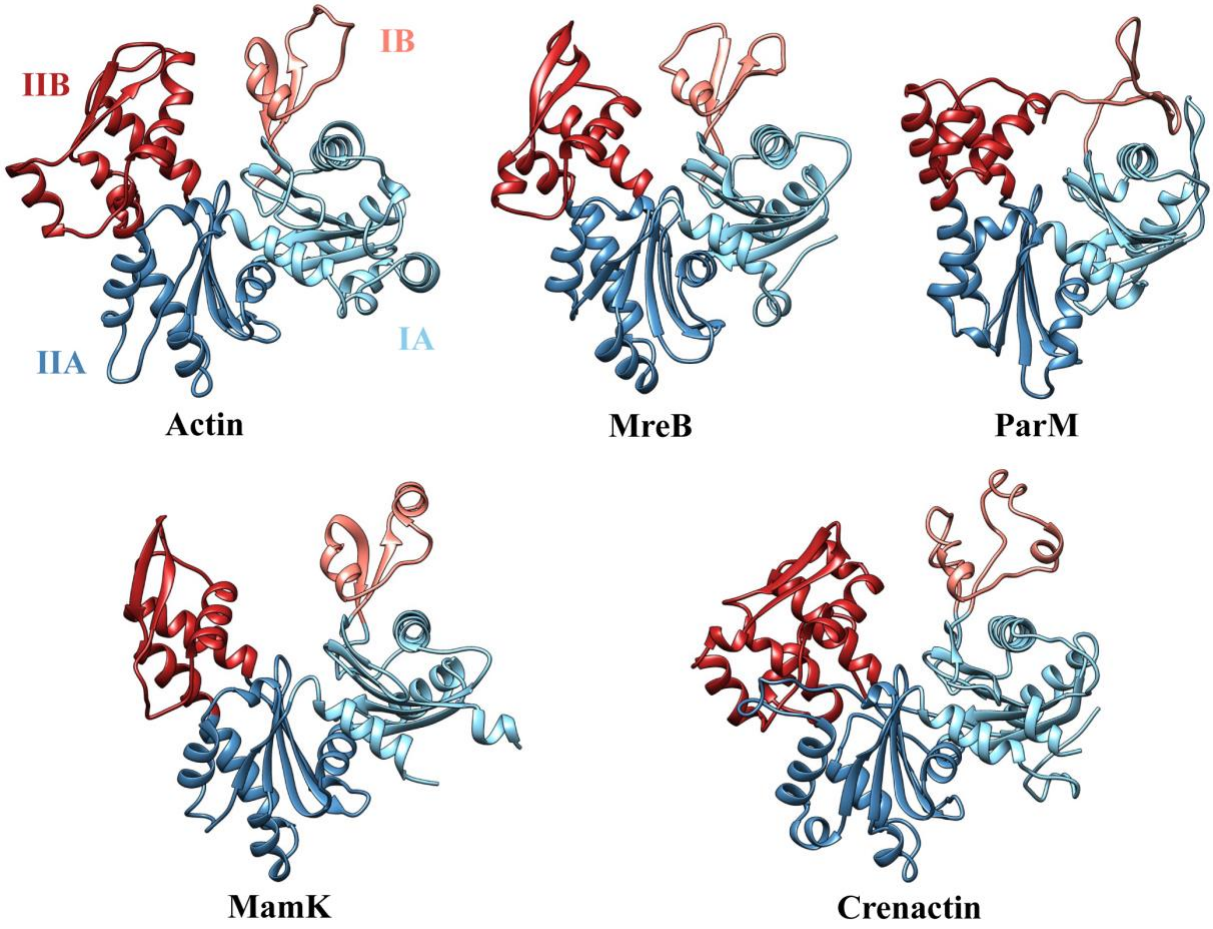

Figure 1.4: Conservation of actin fold in bacteria. Known crystal structures of actins show that bacterial actins share similarities with the actin fold, described by two domains that each can be divided into two subdomains: IA (light blue), IB (pink), IIA (dark blue) and IIB (red). PDB IDs: Eukaryotic actin (1ATN), MreB from Thermotoga maritima (1JCG), ParM from *Escherichia coli* plasmid R1 (1MWM), MamK from Magnetospirillum magneticum strain AMB-1 (5LJW) and Crenactin from Pyrobaculum calidifontis strain JCM (4CJ7).

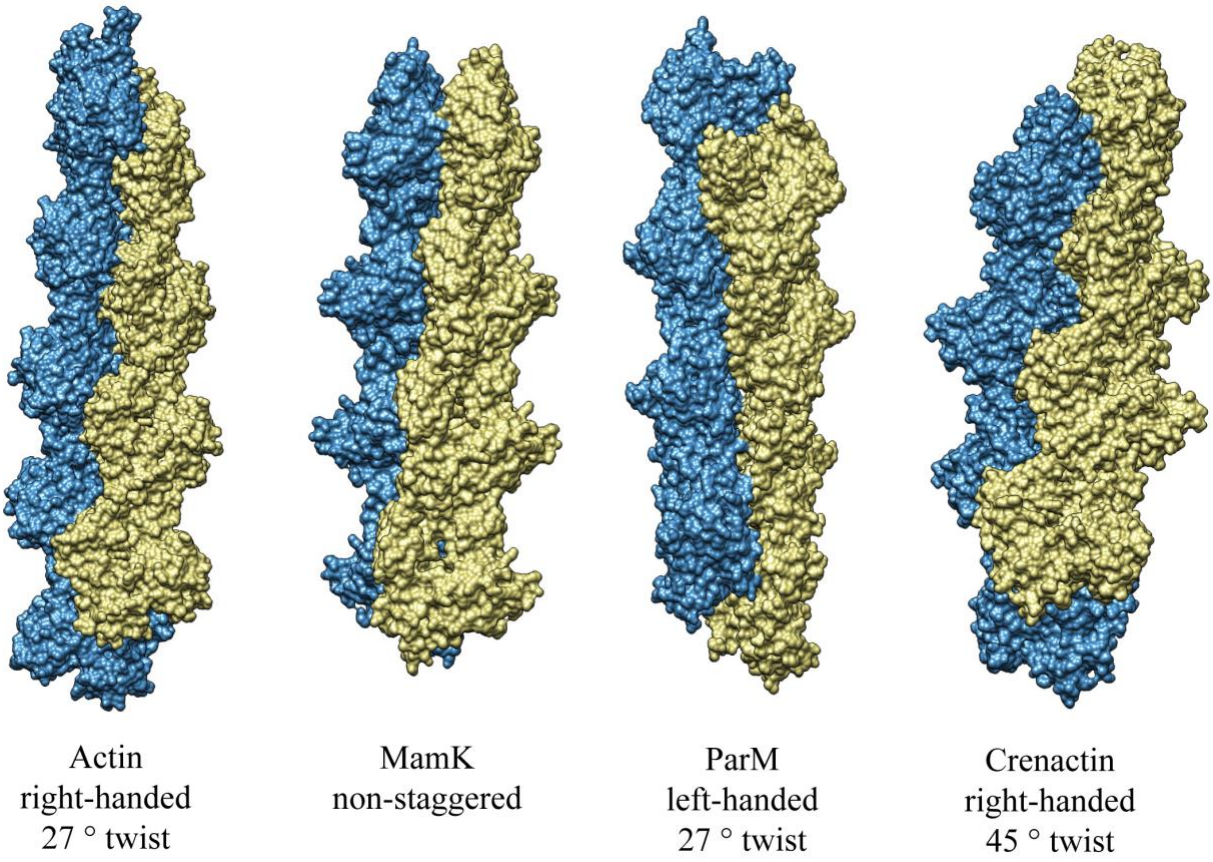

Figure 1.5: Diversity of actin filament architecture. Quarternary strcutures of the bacterial actin family members are different from each other and eukaryotic actin in terms of the degree of twist and handedness. Protein database identifications are 5JLF for actin, 5JLV for MamK, 5AEY for ParM and 5MW1 for Crenactin.

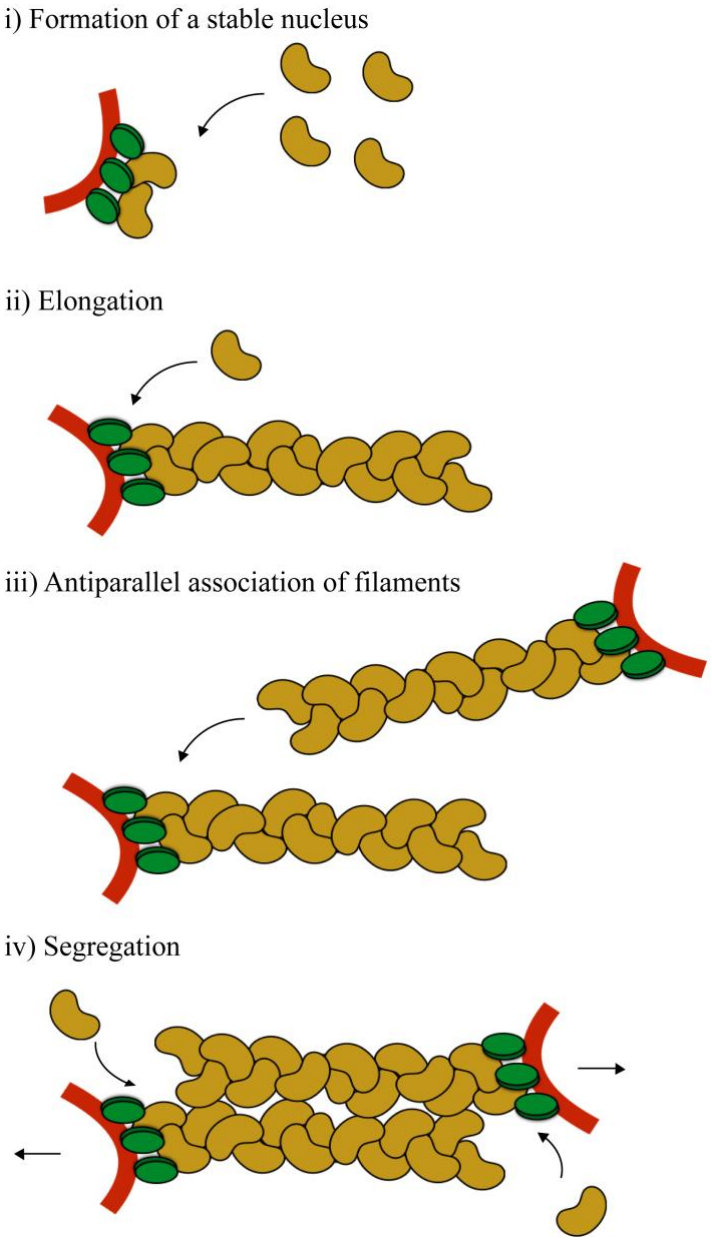

Figure 1.6: AlfA segregation model. i) AlfB (green) and *parN* (red) form the segresome complex and recruit AlfA (yellow) monomers to form a stable nucleus that can promote AlfA filament formation below its critical concentration. ii) The segresome complex remains processively bound to elongating AlfA filaments while elongation with the addition of new AlfA monomers. iii) Filaments interact laterally to form bundles. iv) Antiparallel positioning of filaments allows bundles to push the plasmids to the opposite poles of the cell as the filaments elongate.

CHAPTER II - Methods

2.1. Sequence comparison.

The sequence for AlfA was subjected to a BLAST search (Boratyn *et al.,* 2013), yielding only three matches of significant homology. These three matches were subjected to a second BLAST search, increasing the size of the pool of AlfA homologs missing subdomain IIb. The BLAST search process was repeated until no new homologs with the AlfA domain architecture were found. Multiple sequence alignments were calculated with MAFFT (Katoh *et al.,* 2002), using AlfA and the pool of close homologs and large representative samples of other bacterial actin families (MamK, MreB, ParM, Alp12, Alp7).

2.2. AlfA expression constructs

Previously described untagged expression constructs using a codon-optimized *alfa* gene were used to express wild-type (pJKP100) and non-bundling (pJKP102) AlfA (Polka *et al.,* 2009; Polka *et al.,* 2014). AlfA-F12A was generated by site-directed mutagenesis of pJKP100. For non-assembling mutants, the AlfA coding region was cloned into pSMT3-Kan (Mossessova & Lima, 2000), which inserted a His-SMT3/SUMO tag at the N terminus of AlfA. AlfC coding region from native *Bacillus subtilis* plasmids pBET131 cloned into pSMT-Kan (Mossessova & Lima, 2000) to insert a N-terminal His-SMT3/SUMO tag. The tag can be cleaved by ULP1 protease, leaving only two residual non-native residues at the N-terminus.

2.3. Site-directed mutagenesis

Primers were designed by using QuickChange Primer Design software (Agilent). 10 pM stock solutions of both forward and reverse primer were prepared in sterile water. Plasmid DNA

(pJKP100) was used as the DNA template while the primers were used to introduce the single point mutation (F12A) to wild-type AlfA and amplify the mutated product by polymerase chain reaction (PCR) (Mullis, 1990). After amplification was completed, 1µl DnpI (20,000 units/ml) was added to the 50 µl reaction mixture and incubated for 6 hours at 37 °C. Amplified products were purified by using EZ-10 Spin Column PCR Purification Kit (BioBasic). 10 µl of the purified product was transformed into Top10 competent cells for plasmid isolation and plated onto lysogeny broth (LB) agar media. Single colonies were picked and inoculated into LB media. Plasmids were purified from the culture grown overnight by using GeneJet Plasmid Miniprep Kit (Thermo Fisher). Isolated plasmids were stored at -20 °C. Presence of the mutation was confirmed by sequencing.

2.4. AlfA expression and purification

Plasmids carrying recombinant wild-type (pJKP100), non-bundling (pJKP102) and F12A mutant (GU001) AlfA constructs were transformed into C43 cells. The constructs were overexpressed via isopropyl-β-D-thiogalactopyranoside (IPTG)-inducible promoters overnight at 18 °C. Wild-type, non-bundling AlfA, and AlfA-F12A were purified using ATP cycling, a previously described method that uses cycling between polymerized and unpolymerized states (Polka *et al.*, 2009). Cell pellets were resuspended in polymerization buffer (25 mM Tris pH 7.5, 300 mM KCl) and lysed by sonication. The lysate was cleared by ultracentrifugation for 1 hour at 4 °C at 105,000 × g in a type 50.2 Ti rotor (Beckman Coulter). 5 mM ATP and 12 mM $MgCl_2$ were added into the cleared lysate to initiate polymerization of AlfA filaments and the reaction has been sustained for 30 minutes on ice. Same ultracentrifugation settings were used to pellet AlfA filaments at 4 °C for 1 hour. After discarding the supernatant, pelleted filaments were resuspended

in depolymerization buffer (25 mM Tris pH 7.5, 300 mM KCl, 5 mM EDTA). Resuspension was then dialyzed overnight against the depolymerization buffer. To remove any unpolymerized material remaining, ultracentrifugation was used as described above. The same polymerization-depolymerization cycle was repeated to increase the purity of the AlfA filaments in the sample. The final soluble AlfA sample was then applied to a Superdex 200 (10/300) size-exclusion column in polymerization buffer. Purity of each fraction was assessed by using 12% sodium dodecyl sulfate-polyacrylamide gel electrophoresis (SDS-PAGE). Peak fractions from the chromatography with the highest level of purity were pooled and concentrated by using 30 kDa molecular weight cutoff (MWCO) centrifugal filters (Millipore). The concentrated sample was flash-frozen in liquid nitrogen and stored at −80 °C or stored for up to a week at 4 °C.

2.5. AlfA non-polymerizing (R78D, K79D) mutant expression and purification

The plasmid carrying the AlfA R78D K70D (PJK008) mutant were transformed into C43 cells. Overexpression of the protein was induced by using IPTG and the cultures were grown overnight at 18 °C. Cell pellets were resuspended in lysis buffer (25 mM Tris pH 7.5, 300 mM KCl, 25 mM imidazole) and lysed by sonication. The lysate was cleared by centrifugation for 40 minutes at 4 °C at 14,000 × rpm in Fiberlite F14-14x50cy Fixed-Angle Rotor (Thermo Fisher). Cleared lysate was loaded into a prepacked Ni-NTA affinity resin column (Qiagen). GE Akta Start system was used to perform immobilized metal affinity chromatography (IMAC). Elution buffer (25 mM Tris pH 7.5, 300 mM KCl, 250 mM imidazole) was used to elute AlfA. Fractions of elute were collected and combined to cleave their SUMO-His tag by ubiquitin-like protein (ULP) protease. The protein concentration was measured using Bradford Assay and 1:100 ULP protease to protein mass ratio was used for cleavage. Cleavage performed overnight at 4 °C in

polymerization buffer. To separate SUMO-His tag and the protease from AlfA, the dialyzed sample was incubated with 2 ml of Ni-NTA resin for an hour at 4 °C by rocking. The mixture was transferred into a column and AlfA was separated using gravity column chromatography. To increase the purity of AlfA further, the flow-through was concentrated using a centrifugal filter and then applied to a Superdex 200 (10/300) size-exclusion column in polymerization buffer. The purity of each fraction was assessed by using 12% SDS-PAGE. Peak fractions from the size exclusion chromatography were pooled and concentrated in 30 kDa MWCO centrifugal filters (Milipore). The concentrated sample was flash-frozen in liquid nitrogen and stored at −80 °C.

2.6. AlfB expression and purification

6xHis tagged recombinant AlfB construct (pJKP104) was transformed into BL21 DE3 cells for protein expression. IPTG was used to induce overexpression of the protein overnight at 18 °C. Lysis buffer (50 mM Sodium phosphate at pH 8.0, 300 mM KCl, 10% glycerol and 25 mM imidazole) was used to lyse the cells with sonication and elution buffer (50 mM Sodium phosphate at pH 8.0, 300 mM KCl, 10% glycerol and 250 mM imidazole) was used to elute the protein bound to Ni-NTA resin. The same IMAC system was used for AlfB purification as the one described for AlfA non-polymerizing mutant to perform affinity chromatography. After protein concentration of the elute was measured, 1:100 TEV protease to protein ratio was used to cleave the tag. Cleavage was performed in 50 mM Hepes pH 7.6 and 50 mM KCl overnight at 4 °C. The tag and the protease were separated from AlfB using 2 ml Ni-NTA resin and gravity column chromatography, as previously described. AlfB was further purified by size exclusion chromatography on a Superdex 75 (10/300) size exclusion column in the dialysis buffer and the purity of each fraction was assessed on 15% SDS-PAGE. Fractions with the highest purity were pooled together and

concentrated in 3 kDa MWCO centrifugal filters (Milipore). The aliquots were flash frozen in liquid nitrogen and stored at -80 °C.

2.7. AlfC expression and purification

Recombinant SUMO-His AlfC construct (PJK054) was transformed into BL21(DE3)pLysS cells for protein expression. Since AlfC had not been purified before, the same sodium phosphate buffers and IMAC purification protocol used to purify AlfB were used for AlfC purification. After pooling the fractions eluted from the affinity column, protein concentration was determined by Bradford assay. ULP protease was added to the purified SUMO-His AlfC sample at 1:100 mass ratio to cleave the tag. Cleavage was performed overnight at 4 °C in 50 mM Hepes pH 7.6, 150 mM KCl buffer. The sample was incubated with 2 ml Ni-NTA resin for an hour and then gravity column chromatography was used to elute the unbound AlfC. 3 kDa MWCO centrifugal filters (Millipore) were used to concentrate the protein sample, which was further purified with Superdex 75 column (10/300) in 50 mM Hepes pH 7.6, 150 mM KCl buffer. 16% separating and 4% stacking polyacrylamide gels were used to assess the purity of AlfC by Tricine-SDS-PAGE (Schägger, 2006).

2.8. Negative staining electron microscopy

Wild-type and F12A AlfA mutant samples were polymerized for 15 minutes at room temperature in polymerization buffer with 1 mM nucleotide and 1 mM $MgCl_2$. Samples were applied to glow-discharged 400-mesh carbon-coated grids, and negatively stained with 0.7% uranyl formate (Ohi *et al.*, 2004). Images were obtained on an FEI Morgagni microscope operating at 100 kV, at 22,000× magnification, recorded on an Orious CCD camera (Gatan). For

quantification of assembly of wild-type and F12A mutants images were collected on an FEI Spirit microscope operating at 120 kV with an Ultrascan 4k × 4k CCD camera (Gatan). We used Leginon for automated data collection, acquiring images at random positions using the raster function for high magnification targeting (Suloway *et al.,* 2005).

AlfA was titrated with segresome and free AlfB in the presence of 50mM Hepes pH 7.6 and 50 mM KCl, 5 mM AMPPNP and 5 mM $MgCl_2$. Mixtures were incubated on ice for 15 minutes before they were applied to glow-discharged 400-mesh carbon-coated grids and negatively stained with 0.7% uranyl formate. Images were obtained on FEI Morgagni microscope at 22,000× magnification, and recorded on an Orius CCD camera (Gatan).

2.9. Cryo-electron microscopy data acquisition and image processing

Non-bundling AlfA was assembled at room temperature, using 5 μM protein in polymerization buffer with 5 mM AMPPNP and 5 mM $MgCl_2$ added. Samples were applied to glow-discharged C-FLAT 1.2/1.3–4C holey carbon grids (Protochips) and plunge-frozen in liquid ethane in a Vitrobot Mark IV vitrification device (FEI). Data were collected with an FEI Titan Krios microscope operated at 300 kV on a K2 Summit direct electron detector (Gatan) operating in superresolution mode with a pixel size of 0.5 Å per pixel. Movies were recorded for 7.2 s, with 0.2-s frames, 72 e−/Å2 total dose per movie. Leginon was used for automated data acquisition (Suloway *et al.,* 2005).

Movies were aligned, dose-weighted, and Fourier-binned using MotionCor2 (Zheng *et al.,* 2017). Defocus parameters were determined from the unweighted aligned sums using GCTF (Zhang, 2016). Filaments were automatically identified using RELION, and extracted in overlapping 448-Å boxes using a step size of 25 Å to match the AlfA helical rise (He & Scheres,

2017). This yielded 123,296 boxed segments. Helical segments were subjected to reference-free 2D classification in RELION, and poorly aligning segments were rejected from further processing, leaving a dataset of 113,222 segments for 3D processing.

An initial reconstruction was calculated using iterative helical real-space reconstruction in SPIDER, essentially as described previously (Bergeron *et al.,* 2017; Egelman, 2010; Sachse *et al.,* 2007). This model was low-pass–filtered at 60 Å and used as an initial model for helical refinement in RELION (He & Scheres, 2017; Kimanius *et al.,* 2016; Scheres 2012). After initial gold-standard helical refinement using a spherical mask yielded a structure at about 5-Å resolution, helical segments were subjected to the RELION particle polishing routine, and refinement was continued using a shape-based soft-edged mask enclosing six AlfA protomers (Figure 3.6B). The final reported resolution is from a Fourier shell correlation (FSC) curve corrected for masking artifacts.

2.10. Atomic model building and analysis

An initial structure of the AlfA protomer was generated asymmetrically using RosettaCM (Song *et al.,* 2013) for comparative modeling into the EM density map, using a diverse set of actin atomic structures as templates (PDB ID codes: 1JCE, 2FSJ, 2ZGY, 3I33, 3JS6, 4APW, 4B1Y, 4KBO, 4PL7, 4RTF, 4XE7, 4XHP, 5EC0, 5F0X, 5LJW). Several loop regions (residues 65–83, 36–44, 195–215) were then rebuilt in Rosetta in the context of the helical lattice. This was followed by automated refinement of the entire structure in Rosetta using helical symmetry constraints using the protocol described by Wang et al. (Wang *et al.,* 2016). Finally, some side-chain rotamers were adjusted manually to improve fit to density.

The sizes of interacting surfaces between domains in AlfA and other actin filaments were calculated using the PDBePISA server (Krissinel & Henrick, 2007). All cryo-EM structures and atomic models were visualized in Chimera (Goddard *et al.*, 2007).

2.11. Pelleting assays

Concentrated stock solutions of both AlfA, AlfB, and segresome were cleared via ultracentrifugation (Beckman Coulter Optima TLX) to remove any large aggregates prior to the assay. Ultracentrifugation was performed using a TLA 100 rotor at 90,000 rpm for 30 minutes at 4 °C. Supernatants were taken and their protein concentrations were determined by Bradford assay. For reactions that contain AlfA and AlfB, samples were prepared using polymerization buffer, as their final volume will be 50 µl. For reactions that contain AlfA and segresome reactions were prepared by using segresome formation buffer (50 mM Hepes pH 7.6, 50 mM KCl). Nucleotide and $MgCl_2$ added to each mixture at final concentrations of 5mM. Mixtures were incubated on ice for 15 minutes to start the assembly reaction. 5 µl samples were taken from each sample prior to ultracentrifugation for SDS-PAGE analysis. Ultracentrifugation was performed at 90,000 rpm for 30 minutes at 4 °C using a TLA 100 rotor. 5 µl sample from each supernatant was taken for SDS-PAGE analysis without disturbing the pellet. Each pellet was dissolved by using 95 µl depolymerization buffer and 5 µl sample was taken from each dissolved pellet for SDS-PAGE analysis. Electrophoresis was performed at 150V for an hour. Gels were stained by using staining solution (0.1% Coomassie Brilliant Blue, 50% methanol and 10% glacial acetic acid) and destained by using destaining solution (40% methanol and 10% glacial acetic acid).

Destained gels were scanned using a BIO-RAD Gel Doc imaging system and the intensity of each band was determined by using ImageJ. Protein concentrations in the pellet were calculated

by using the following formula; [pellet]=((I_{load}-I_{sup})/I_{load})x[load], where I_{load} is the band intensity of the pre-ultracentrifugation sample, I_{sup} is the band intensity of the post-ultracentrifuge supernatant and [load] is the initial concentration of the protein. Microsoft Excel was used to make the calculations and prepare the graph.

2.12. Reconstitution of the segresome complex

Custom synthesized *parN* oligos were ordered (Integrated DNA Technologies) as reverse complementing strands. 1 mM oligos were prepared in sterilized water. Each oligo was mixed with its reverse complementing strand at equimolar ratio and incubated 95 ℃ for 2 minutes and then at 25 ℃ for another 2 minutes to form 500 µM double-stranded oligos. Each double-stranded *parN* was mixed with purified AlfB to have a sample that contains 50 µM *parN* and 300 µM AlfB. The mixture was incubated on ice for 30 minutes and purified on a Superdex 200 (10/300) size exclusion column in 50 mM Hepes pH 7.6 and 50 mM KCl.

5% stacking and 10% separating polyacrylamide gels were prepared for analyzing the purified segresome complex by non-denaturing PAGE (Hellman & Fried, 2007). Gels were run at 180 V for 45 minutes by using 1X TAE buffer. After the run, gels were first stained with EtBr containing TAE buffer and then Coomassie stain for detection of DNA and protein, respectively.

2.13. Size exclusion chromatography coupled multi angle light scattering

1.1 mg/ml segresome complex sample was placed in a 4℃ autosampler that injected 25 µL sample onto a Superose 6 Increase 3.2/300 mm column (GE) equilibrated with the buffer that was used for the complex formation (50 mM Hepes, 50 mM KCl, pH 7.6). Size exclusion chromatography was performed on a GE AKTA Pure coupled to a Wyatt miniDAWN TREOS and

Optilab T-rEX differential refractive index detector. Molar mass was calculated from the Raleigh ratio based on multi-angle (static) light scattering and protein concentration from the change in refractive index (dn/dc = 0.185). Data analysis was performed using Wyatt ASTRA VI software.

2.14. Dynamic light scattering

Reactions were prepared in 1x PBS buffer at pH 7.4. 5 mM ATP and 5 mM $MgCl_2$ added into each reaction. Samples were incubated on ice for 15 minutes and 10 µl from each sample was transferred into a glass cuvette for the measurements. Ten acquisitions were made for each measurement using DynaPro Nanostar (Wyatt Technology). Raw data were exported from Dynamics 7.0.1 software and the plots were generated using Microsoft Excel.

2.15. Crosslinking mass spectrometry

190 µl crosslinking reactions were set for each condition. All the reagents were dissolved in 50 mM Hepes pH 7.6 and 50 mM KCl buffer. Final concentrations of DSS, ATP, and $MgCl_2$ were determined as they will be 0.5 mM, 5 mM and 5 mM, respectively. 35 µl samples were taken at 5 minutes, 10 minutes, 30 minutes and 45 minutes into the crosslinking reaction. Each sample taken were quenched with 91 mM ammonium bicarbonate. Quenched reactions were incubated at room temperature for 30 minutes and 12 µl of each quenched sample was used for SDS-PAGE analysis. Remaining samples were reduced with 5.4 mM Tris(2-carboxyethyl)phosphine) (TCEP) and 0.1% w/v PPS Silent Surfactant at 60 °C for 1 hour shaking. Samples were cooled down to room temperature and treated with 6.1 mM iodoacetamide for 20 minutes of alkylation at dark. Trypsin was added to a 1:15 enzyme to substrate ratio to initiate digestion. Digestion was performed at 37 °C for 4 hours with shaking. After digestion, the samples were kept at 4 °C

overnight. Before MS analysis, HCl was added to a concentration of 250 mM, and acidified samples were incubated at room temperature for an hour to cleave PPS Silent Surfactant. Samples were centrifuged at 20,000 g for 5 minutes to remove any aggregates before injection.

Mass spectrometry and data analysis were performed on a Q-Exactive Plus (Thermo Fisher Scientific) operated at data-dependent mode. A 150-µm Kasil fritted trap column packed with Reprosil-Pur C18-AQ silica (3-µm bead diameter) to a bed length of 2 cm was used to trap digested peptides (0.6-0.9 µg). The trap column was attached to a 75-µm i.d. Pico-Frit column (New Objective) self-packed with 30 cm of Reprosil-Pur C18-AQ (3-µm bead diameter) for separation of the peptides. Peptides were eluted from the column at 0.25 µL/min using a 120-min acetonitrile gradient of 2–60%.

Mass spectra were converted into mzML format using msconvert application from ProteoWizard software (Kessner *et al.,* 2008). Comet software was used to identify all detectable proteins in the sample by searching against whole-proteome databases (Eng *et al.,* 2013). Cross-linked peptides were identified using Kojak 1.4.3 and Percolator 2.08 was used to assign statistically meaningful q values to Kojak identifications (Umbreit *et al.,* 2014; Westermann *et al.,* 2006). Data were filtered to show target proteins that had a Percolator-assigned peptide-level q value of ≤0.01. Crosslinks were presented using proXL database and mapped onto the atomic model using Chimera (Goddard *et al.,* 2007; Zelter *at al.,* 2015)

2.15. Hydrogen-deuterium exchange mass spectrometry

0.5 mg/ml wild-type AlfA was incubated with 5 mM AMPPNP and 5 mM $MgCl_2$ at 25 °C, prior to hydrogen–deuterium exchange experiments. For apo state, the volume of AMPPNP and $MgCl_2$ within the stock solution replaced with the buffer (25 mM Tris pH 7.5, 100 mM KCl). 100X

Tetrapeptide PPPI standards were added to stock protein solutions as internal standards (Zhang *et al.,* 2012). To initiate exchange reactions, 5 µl 20X buffer, 5 µl 20X $MgCl_2$, 5 µl 20X AMPPNP and 75 µl D_2O (Cambridge Isotope Labs) were added into 10 µl stock solution of nucleotide-bound AlfA. For apo AlfA, 5 µl 20X buffer and 85 µl D_2O were used to initiate deuteration. Deuteration progressed for 3 seconds, 1 minutes, 30 minutes and 20 hours for both AMPPNP bound and apo states. Undeuterated samples were prepared using MS grade H_2O (Thermo Fischer) instead of D_2O. For fully deuterated samples, stock protein solutions were denatured with 7 M GdHCl and 1M DTT at 85 °C for 3 hours. 10 µl of the denatured sample was 10-fold diluted with 85 µl D_2O and 5 µl 20X buffer to have a final volume of 100 µl. Samples were quenched with an equal volume of ice-cold quench buffer (0.2% formic acid (FA), 0.1% trifluoroacetic acid (TFA), 8M urea, pH 2.5). Quenched samples were flash frozen by liquid nitrogen as soon as possible and kept at -80 °C until analyzed with mass spectrometry.

For mass spectrometry analysis, samples were thawed on ice for 5 min and injected onto a refrigerated Waters nanoAcquity H/DX-UPLC system coupled to a Synapt G2-S QTOF mass spectrometer (Waters). Peptides were digested on a Waters Enzymate BEH pepsin column and trapped on a XP VanGuard column (2.1 mm x 5 mm), followed by separation using an analytical column (ACQUITY UPLC CHS C18 1.7 µm, Waters) running a gradient of 5– 40% solvent B for 8 min (solvent A, 0.1% FA, 0.025% TFA, and 2% acetonitrile (ACN); solvent B, 0.1% FA, and 100% ACN) at 40 µl/min. The electrospray ionization source was operated in the positive ion mode and ion mobility was enabled for the instrument.

A subset of peptides obtained from tandem MS/MS of undeuterated apo AlfA sample was chosen to monitor the exchange throughout the entire AlfA sequence. Mass spectra and chromatographic elution profiles of the selected peptides were determined by using DriftScope

and MassLynx (Waters). Exact mass and retention time of each peptide were integrated into HX-Express within Microsoft Excel to determine mass shifts between the undeuterated sample and each time point (Weis et al., 2006). Percent deuterium exchange was calculated for each time point according to the following equation $\%RHDX = 100 \times [(m-m_{0\%})/(m_{100\%}-m_{0\%})]$, where m is the mass centroid of the fragment at a given tie point, $m_{0\%}$ is the mass centroid of the undeuterated fragment and $m_{100\%}$ is the mass centroid of the fully deuterated sample (Guttman, *et al.,* 2012). Binomial fitting was implemented for accurate determination of centroid mass and deconvolution of the bimodal spectra (Guttman, *et al.,* 2013)

After determining percent deuterium exchange rates for both apo and AMPPNP bound state, we calculated the percent changes in exchange rates of AMPPNP bound state relative to the apo state at 3 seconds of exchange using the following equation $\%\Delta RHDX = 100 \times (RHDX_{AMPPNP}/RHDX_{apo})$. Exchange rates were mapped onto the atomic model and the filament structure by using Chimera (Goddard *et al.,* 2007).

CHAPTER III - Revealing the molecular details of AlfA filament structure

(Adapted from Usluer, G. D. *et al.,* Cryo-EM structure of the bacterial actin AlfA reveals unique assembly and ATP-binding interaction and the absence of a conserved subdomain. *Proc. Natl. Acad. Sci. U.S.A.* **15,** 3356–3361 (2018))

3.1. Introduction

Actin is one of the most highly conserved eukaryotic proteins, with critical roles in processes as diverse as motility (Rottner & Stradal, 2011), cell shape (Heuser & Kirschner, 1980; Hussey *et al.,* 2006), organelle positioning (Pruyne *et al.*, 2004), and cell division (Pollard, 2010). Bacterial actins are involved in many of the same processes (Errington *et al.*, 2003; Komeili *et al.*, 2006; Margolin, 2009), and share evolutionarily conserved functional properties with eukaryotic actin: they form filaments whose assembly and disassembly is controlled by ATP binding and hydrolysis (Backer *et al.*, 2006; Derman *et al.*, 2009; Draper *et al.*, 2011; Garner *et al.*, 2004; Polka *et al.*, 2009; van den Ent *et al.*, 2002), their assembly dynamics are modulated by regulatory proteins (Draper *et al.*, 2011; Garner *et al.* 2007), and the filaments can serve as the basis for larger cellular structures (Polka *et al.*, 2009; Popp *et al.*, 2010; Salje *et al.*, 2009). Actins all share a conserved structural core that has a complex topology of two domains (I and II), each arranged as two subdomains (Ia, Ib, IIa, and IIb), with an ATP binding site between domains I and II (Kabsch *et al.*, 1990). Five conserved sequence motifs (phosphate 1, connect 1, phosphate 2, adenosine, connect 2) in domains Ia and IIa surround the ATP binding site and have served to define members of the family (Bork et *al.,* 1992). The fold is also shared with Hsp70 and sugar kinases, which bind and hydrolyze ATP but do not form filaments. All members of this broader family undergo

functionally important conformational changes upon ATP binding and hydrolysis that, in the actins, underlie assembly dynamics.

Despite these conserved features, bacterial actins exhibit far lower levels of sequence conservation than their eukaryotic counterpart. Unlike eukaryotic actin, where a single filament form has been adapted to multiple functions through a host of regulatory binding proteins, bacteria have evolved specialized actins for specific purposes that require fewer interaction partners. This has relaxed evolutionary constraints and allowed bacterial actins to explore a greater range of sequence diversity. The result is extensive divergence of bacterial actins at the sequence level, with corresponding variation in filament architecture, function, and dynamics.

A diverse subset of bacterial actins is involved in separation of plasmid DNA. Large, low-copy number plasmids often encode active segregation systems to ensure against stochastic loss when the host cell divides. Most segregation systems are composed of three elements encoded on the plasmid itself: a cytomotive filament to provide the force for plasmid movement, an adaptor protein that couples filament movement to the plasmid, and a centromere-like DNA region bound by the adaptor (Baxter & Funnel, 2014). Several different types of ATP-dependent cytomotive filaments have been adapted for plasmid segregation (Pan *et al.*, 2012; Sonkaria *et al.*, 2012; Taoka *et al.*, 2007), with bacterial actins among the most widely distributed (Derman *et al.*, 2009).

The most well studied actin-based segregation system is the par operon of the R1 multidrug resistance plasmid in *Escherichia coli*. ParM filaments are dynamically unstable: they assemble upon ATP binding and hydrolyze ATP with kinetics that lag behind assembly, so that when the hydrolysis front reaches the end of a growing filament it catastrophically disassembles due to reduced stability of the ADP-bound state (Garner *et al.*, 2004). ParM makes use of dynamic instability in a search and capture mechanism to segregate plasmids. Filaments nucleate

spontaneously, and those that fail to encounter an adaptor–DNA complex eventually disassemble. When the ends of ParM filaments do encounter adaptor–DNA complexes, their dynamic instability is suppressed, allowing processive growth that separates plasmids by pushing them toward opposite poles (Campbell & Mullins, 2007; Garner *et al.,* 2007).

The plasmid segregating actin AlfA, encoded by the *Bacillus subtilis* plasmid pLS32, was initially identified as an actin on the basis of the five conserved actin motifs, and like other actins AlfA forms ATP-dependent filaments both in vivo and in vitro (Beker *et al.,* 2006; Polka *et al.,* 2009). Unlike ParM, however, AlfA is not dynamically unstable, forming stable filaments that remain assembled indefinitely in the ADP-bound state (Polka *et al.,* 2009). Moreover, unlike ParM, which is structurally polar but grows at equal rates from both ends (Garner *et al.,* 2004), AlfA filaments grow unidirectionally (Polka *et al.,* 2014). AlfA filaments associate laterally into mixed polarity bundles, and extension of plasmid-bound filaments along bundles provides the mechanism of plasmid segregation. The adaptor protein AlfB regulates AlfA dynamics: free AlfB suppresses AlfA growth and promotes disassembly of ADP-bound filaments, while AlfB–DNA complexes nucleate AlfA filaments (Polka *et al.,* 2014). These combined activities suppress spontaneous nucleation and ensure that filaments grow primarily from plasmids. Consistent with its unusual dynamics, our initial low-resolution structural studies of AlfA filaments revealed an unusual filament architecture, more ribbon-like and twisted than other actins (Polka *et al.,* 2009). However, the relationship between this architecture and the dynamic properties of AlfA has remained unclear, as no high-resolution structures of the AlfA filament nor crystal structure of monomeric AlfA has been determined.

Here, we report the structure of AlfA filaments determined by electron cryo-microscopy (cryo-EM) at near-atomic resolution, which reveals the basis for its unique structural and

functional characteristics. We show that AlfA lacks the canonical actin subdomain IIb, which plays important structural and functional roles in all other actins. AlfA polymerization interfaces have diverged extensively from other actins, and AlfA binds ATP through completely novel interactions with the adenosine base. These unique features of AlfA explain how it assembles stable filaments despite the loss of subdomain IIb, and why the filaments remain stable after ATP hydrolysis.

3.2. Results

3.2.1. AlfA lacks subdomain IIb

In seeking clues to the unusual architecture from the AlfA sequence, we carried out extensive sequence searches and multiple sequence alignment with bacterial actins. While AlfA was clearly identified as an actin on the basis of the five conserved actin motifs (Becker *et al.*, 2006), sequence alignment of regions outside these motifs can be challenging due to the very low level of sequence identity. Beginning with alignments of only the closest relatives to AlfA and expanding the size of the sequence set, we were able to generate robust alignments showing that AlfA is missing the canonical subdomain IIb (Figure 3.1). The closest homologs, with an average identity of ~20% to AlfA, constitute a family defined by the lack of IIb, consisting of actins primarily from Gram-negative bacteria, and from several *Bacillus* phages (Figure 3.2). The relatively limited number of actins in this family suggests that they have experienced a deletion of IIb during their evolutionary divergence from other actins.

Subdomain IIb is critical for function in all other actins described to date. While IIb does not include any of the conserved ATP-binding motifs, it forms half of the binding pocket for the ATP adenosine base and contributes a significant fraction (17–35%) of the total surface area buried in filament assembly interfaces. In other actins, ATP binding allosterically regulates

polymerization by stabilizing a filament-bound ATP conformation whose major difference with the unbound conformation is the relative positioning of subdomains Ib and IIb (Figure 3.3). The importance of IIb assembly interactions is highlighted by their role in ParM dynamic instability, where structural changes associated with ATP hydrolysis break IIb interactions with neighboring protomers, destabilizing the filament (Galkin *et al.,* 2009). The integral role of IIb in actin filament structure and function raises several questions: How can AlfA bind ATP with half of the canonical binding site missing? How is it able to form stable filaments without the IIb assembly interfaces? And how does ATP binding trigger polymerization? To answer these questions, we determined the structure of the AlfA filament using cryo-EM.

3.2.2. AlfA filament structure

At physiological salt concentrations, AlfA filaments spontaneously assemble into bundles of variable thickness that are not well suited to high-resolution structure determination. However, bundles can be dissociated into single two-stranded filaments at high salt concentrations (Polka *et al.,* 2009). We initially attempted to determine the cryo-EM structure of single AlfA filaments in 1 M KCl, but background from high salt concentration limited the resolution of these reconstructions to about 12 Å. We turned to a mutant we had previously designed, (two pairs of lysines—K21,K22 and K101,K102—mutated to alanines) that forms single filaments that do not form bundles in vitro, except in the presence of high concentrations of crowding agents (Polka *et al.,* 2014). These mutants can be imaged as single filaments at lower salt concentrations, making the sample better suited to high-resolution structure determination (Figure 3.4).

We assembled the nonbundling AlfA mutant with the non-hydrolyzable ATP analog AMPPNP, and determined the structure of the filaments at 4.2-Å resolution by cryo-EM (Figure

3.5 and Figure 3.6). The refined helical symmetry of the two-stranded filament was 157.7° rotation and 24.4 Å rise per subunit, giving a repeat distance of 394 Å (Fig 3.5A). The two strands are parallel and offset by a half-subunit stagger. The repeat distance is considerably shorter than found in other actins, which range from 512 to 834 Å (Bergeron *et al.,* 2017; Bharat *et al.,* 2015; Izoré *et al.,* 2016; Löwe *et al.,* 2016; Ozyamak *et al.,* 2013; von der Ecken *et al.,* 2016), yielding a highly-twisted AlfA filament with only eight subunits per turn of the two-start helix. The filament has a left-handed two-start twist, confirming the previous determination of handedness by tomographic reconstruction of negatively stained AlfA filaments (Polka *et al.,* 2009).

Our cryo-EM map has a clearly defined secondary structure throughout, with bulky side-chains visible in some regions. We generated an atomic model using comparative modeling (Song *et al.,* 2013) followed by automated refinement (Wang *et al.,* 2016), which covers the entire AlfA sequence and includes bound AMPPNP (Figure 3.5 B and C and Figure 3.6 D and E). Comparison of our atomic model with other actins confirmed that subdomain IIb is missing, replaced by a short five-residue loop (Figure 3.5D). It is likely that the lack of IIb has reduced constraints on the helical symmetry of AlfA, making the more highly twisted architecture possible. The rest of the AlfA protomer has the typical actin fold, with subdomains Ia and IIa, each built by a pair of α-helices packed against a five-stranded mixed-polarity β-sheet, and subdomain Ib consisting of a small three-stranded antiparallel β-sheet and a short helix. Like ParM from the R1 (van den Ent *et al.,* 2001) and pSK41 (Popp *et al.,* 2010) plasmids, *Bacillus thurigensis* (Jiang *et al.,* 2016), and the archael actin Ta0853 (Roeben *et al.,* 2006), the subdomain Ib three-stranded β-sheet of AlfA wraps around helix1 (residues 82–99), making contacts with a pair of antiparallel β-strands inserted after helix2 (residues 128–143) and burying most of helix1. This similarity suggests that this group of

bacterial actins may share a more recent common evolutionary ancestor with each other than actins like MreB, MamK, crenactin, and eukaryotic actin that lack these features.

3.2.3. A nucleotide binding mode in the AlfA filament

The density for AMPPNP is clearly defined in the cryo-EM map (Figure 3.6E). The overall backbone configuration of AlfA in the ATP binding region is conserved with existing actin structures, with average RMSD of 1.8 Å for backbone atoms between AlfA and protomers of other actin filaments. The three phosphates of AMPPNP are bound as in other actin structures, interacting with residues of the phosphate 1, connect 1, and phosphate 2 motifs. Strikingly, however, the adenosine base is rotated ~120° from the position it occupies in all other actin structures (Figure 3.7A and Figure 3.8). Rather than packing against the adenosine motif in subdomain IIa, in AlfA the adenosine base is sandwiched between the phosphate 1 and connect 2 motifs in subdomain Ia. The ATP base stacks against the side-chain of Tyr255, while Phe12 packs against both the base and the ribose sugar (Figure 3.7B). Both Phe12 and Tyr255 appear to be unique to AlfA (Figure 3.7C). This ATP binding mode, with the base sandwiched between two parts of subdomain Ia, explains how AlfA binds ATP despite the lack of subdomain IIb.

AlfA has only a fourfold difference in critical concentration between ATP and ADP (Polka *et al.*, 2009), indicating that it does not distinguish strongly between di- and triphosphate nucleotides, and explaining why filaments remain assembled in the ADP-bound state. This is in stark contrast to ParM, which experiences dynamic instability and rapidly disassembles after ATP hydrolysis. We reasoned that the unique contacts AlfA makes with the ATP adenosine base provide the basis for its reduced discrimination between ATP and ADP. To test this, we generated a point mutant of Phe12 to alanine (AlfA-F12A) and tested its ability to assemble under different

nucleotide conditions (Figure 3.7D, Figure 3.9, and Table 1). The mutation increased the apparent critical concentration for assembly to about 4 μM from the previously reported value of 2.5 μM (Polka *et al.,* 2009). However, while wild-type AlfA assembles in ADP with a critical concentration of ~10 μM, no assembly was observed with ADP for AlfA-F12A up to 30 μM protein (Figure 3.9). This highlights the importance of Phe12 in nucleotide binding and suggests that the unique ATP binding mode in AlfA is linked to the increased stability of AlfA filaments in ADP.

3.2.4. AlfA assembly interactions

Actin filaments polymerize through two types of interface: head-to-tail longitudinal interactions that run along a single strand, and cross-strand lateral interactions. Longitudinal interactions define the structural polarity of actin filaments, with the two ends generally referred to as the "barbed end" (subdomains Ia and IIa) and the "pointed end" (subdomains Ib and IIb). In the AlfA filament, longitudinal interactions bury about 1,100 $Å^2$ of surface area per protomer, while cross-strand contacts bury about 1,400 $Å^2$ (Figure 3.10). Nearly all of the interaction surfaces are within subdomains Ib and IIa, with only very minor contributions from subdomain Ia, which plays a larger role in assembly of other actins (Figure 3.11). While the total interface area per protomer is lower for AlfA than other actins, the fraction of its total surface involved in interfaces (20%) is comparable. However, the distribution of interfaces across the surface of AlfA is strikingly different from other actins.

The lack of subdomain IIb means that AlfA longitudinal interfaces are less than half the size of the equivalent interfaces in other actins. Longitudinal interactions consist primarily of contacts between a loop (residues 37–45, the equivalent of the D-loop in vertebrate actin) and short α-helix in subdomain Ib (residues 59–65) in one protomer, and loops 162–164 and 179–188 in

subdomain IIa in an adjacent protomer. These include primarily hydrogen-bonding interactions, and a small hydrophobic cluster formed by Leu39 and Phe64 on one protomer and Ile180 and Met187 on the adjacent protomer.

To compensate for reduced longitudinal contacts due to the missing subdomain IIb, AlfA has greatly extended cross-strand interfaces, which are 50–100% larger than those of other actins. The cross-strand interface is also mostly a single large patch running across subdomains Ib and IIa, compared with the distributed contacts scattered across all four subdomains in other actin filaments (Figure 3.10A). The cross-strand interface is formed primarily between a loop in subdomain Ib (residues 69–82) of one protomer with a helix in subdomain IIa (residues 201–211). The aliphatic chains of lysines 206 and 210 on one side of the interface pack against Phe74 and Met82 on the other side of the interface, with the remainder of the contacts being primarily hydrogen-bonding interactions. The equivalent surfaces in other actin filaments are well separated, but the strong left-handed twist of the AlfA strands positions these regions closer to each other in the filament. Overall, both the lateral and longitudinal interfaces consist of primarily of hydrophobic and hydrogen bonding interactions; the lack of ionic interactions likely explains why AlfA filaments are stable under very high salt concentrations (Polka *et al.*, 2009).

To probe the local structural arrangements upon filament assembly, we used HDX-MS. AlfA was treated with D_2O in both apo and AMPPNP bound states and deuterium uptakes of pepsin-digested AlfA peptides after 3 seconds, 1 minute, 30 minutes and 20 hours of hydrogen to deuterium exchange were measured using mass spectrometry. A subset of peptides that covers 95% of AlfA sequence were selected for data analysis by HXExpress (Weis *et al.,* 2006). Hydrogen-deuterium exchange rates of the peptides in both apo and nucleotide bound states were calculated relative to their fully denatured and deuterated counterparts. When compared to each

other, some of the peptides can reach up to >90% deuteration even before 3 seconds of exchange while some stays at a deuteration level less than 50% after 20 hours of dueteration (Figure 3.12A). This suggests that "fast exchanger" peptides were more accessible to the solvent to exchange their hydrogen quickly while "slow exchanger" peptides were closer to the hydrophobic core (Kaltashov *et al.,* 2009). Over time, all the peptides reached to the exchange levels of the denatured sample, except one that contains residues from 93 to 115 (Figure 3.12B-E). When relative exchange rates of the peptides after 3 seconds of deuteration were mapped onto the atomic model, we observed the overall decrease in the exchange rate except the C-terminal region of the helix 1 and the beta strand that connects helix 1 to the N-terminus of helix 2 (Figure 3.12D, F).

To make a direct comparison between the apo and the nucleotide-bound state, we calculated the changes in relative exchange rates of each peptide in the nucleotide bound state compared to apo state at 3 seconds of exchange (Figure 3.13A). We observed a correlation between the regions with the largest decrease in the exchange rates on polymerization with the contacts observed in cryo-EM filament structure (Figure 3.13B, C). Additionally, we observed that phosphate 1 and phosphate 2 motifs of the actin fold in AlfA is more exposed to the solvent when nucleotide is bound, suggesting the opening of the nucleotide binding cleft in the presence of AMPPNP. Together, HDX-MS experiments confirm the conformational changes induced upon nucleotide binding and the accuracy of our atomic model of the AlfA filament.

In our collaborative work with Shun Kai Yang, we verified the AlfA assembly interfaces by generating mutations predicted to disrupt polymerization (Figure 3.14). The mutations were designed at an early stage of cryo-EM structure determination, with a preliminary structure at ~12-Å resolution and a simple homology model of AlfA built by mapping the AlfA sequence onto the structure of R1 ParM. The mutations had varying effects on filament assembly, ranging from no

effect to nearly complete inhibition of assembly, as assessed by filament pelleting assays and negative-stain EM (Figure 3.14C and D). Inspection of the mutation sites in the final high-resolution atomic model reveals that the severity of the effect on polymerization correlates with the position of the mutated residue relative to the interface (Figure 3.14B).

3.2.5. Conclusions

In other actins, the protomers are flattened in the filament relative to their free conformation, with the major change being a rotation between domains I and II around the connect 1 and connect 2 motifs. This conformational change results in large changes to the juxtaposition of subdomains Ib and IIb at the pointed end that would not be relevant in AlfA due to the loss of IIb (Figure 3.3). However, more subtle changes occur upon polymerization between Ia and IIa at the barbed end of the protomer. Assuming that AlfA undergoes a structural conversion similar to other actins, these smaller barbed-end changes may be relevant to promoting filament assembly. The detailed nature of polymerization-associated conformational changes in AlfA awaits a high-resolution structure of the unpolymerized AlfA protomer. AlfA is unusual in that it exhibits extreme kinetic polarity, elongating almost entirely from one end, although which is the growing end has not been established (Polka *et al.,* 2014). The structure of the filament provides a likely explanation for the asymmetry of subunit addition (Figure 3.15). In other actin filaments, assembly interactions involve both domains I and II, whether adding at the barbed or pointed end. Interaction of both domains with the end of the filament stabilizes the flattened filament conformation of newly added protomers at either end. Similarly, at the AlfA barbed end the terminal protomer is bound through both subdomains Ib and IIa, which would create a conformationally stable new helical addition site. However, the terminal protomer at the pointed end is bound only via

subdomain IIa. Being bound by only a single subdomain would potentially allow the terminal protomer to sample multiple conformational states and create a poorly defined, flexible helical addition site. This suggests that unidirectional growth of AlfA occurs at the barbed end, which would make it similar to actin, which grows more rapidly from the barbed than the pointed end, and distinct from ParM, which grows at indistinguishable rates from both ends (Garner *et al.*, 2004).

Another study, published simultaneously with ours, also reported the structure of the AlfA filament. This structure, at 3.4 Å resolution, is broadly consistent with ours, despite independent data processing and model building, strongly confirming our results. They reported 156.5 ° rotation and 24.9 Å rise, which are slightly different than the values we reported (157.7 ° rotation and 24.4 Å rise). However, their description of the filament topology was consistent with our study. Even though they used ParM crystal structure for 3D refinement and a homology model to guide atomic model building, they confirmed the lack subdomain IIB, which indicates the importance of near-atomic resolution cryo-EM data in de novo model building process. Like our filament structure, their filament structure provided strong density around the nucleotide binding pocket, showing the interactions between the conserved residues of the nucleotide binding pocket and the nucleotide (ADP). Additionally, they revealed the unique placement of the adenosine moiety of the nucleotide between residues Phe12 and Tyr255, which further supports our observations that AlfA shows reduced discrimination between ATP and ADP. Both AMPPNP and ADP-bound structures of AlfA showed that longitudinal interaction surface is decreased significantly due to missing subdomain IIb and it involves interactions between subdomain IB and IIA. On the other hand, lateral interaction surfaces of ADP-bound AlfA structure reported to be smaller than AMPPNP-bound AlfA structure, which might indicate arrangements in the lateral interactions surface upon

nucleotide binding. In addition, Szewczak-Harris & Löwe obtained >10Å structure of AlfA doublets, which showed the antiparallel arrangement of AlfA filaments to form higher order assemblies, consistent with the previous observations of Polka et al. (Polka *et al.,* 2008; Szewczak-Harris & Löwe, 2018).

The adaptor protein AlfB regulates AlfA dynamics, nucleating AlfA filaments from plasmid DNA while simultaneously suppressing spontaneous nucleation. Moreover, after nucleation AlfB processively tracks the growing end of AlfA filaments, providing the basis for plasmid segregation (Polka *et al.,* 2014). From the structural analysis of AlfA polarity above, which suggests filaments grow from the barbed end, we would also predict that AlfB binds at the barbed end. This would be similar to interaction between ParM and its adaptor ParR, which binds in a cavity between subdomains Ia and IIa that is only fully exposed at the barbed end. A comparable situation may exist for AlfB binding to AlfA, which has a cavity in the region corresponding to the ParR binding site that partially overlaps with a longitudinal assembly interface. A similar mechanism of insertional polymerization has also been proposed for ParM, in which transient dissociation of one of the multivalent adaptor–filament interactions allows for insertion of a new protomer on one filament strand while the adaptor remains bound to the second strand (Moller-Jensen *et al.,* 2003). Interactions between AlfB and the barbed end of AlfA protomers may be the key to the dual role of AlfB in both suppressing (through sequestration of AlfA monomers as free AlfB) and promoting (through AlfA end-binding when attached to the plasmid) AlfA polymerization; understanding the molecular mechanism of this activity will require further biophysical characterization of AlfA–AlfB interactions.

The combination of altered domain architecture and the mechanism of ATP binding give rise to the uniquely stable, highly twisted filament structure and unusual polymer dynamics of

AlfA. The lack of a canonical actin subdomain is not unprecedented among bacterial actins, as FtsA, part of the cell division machinery, lacks subdomain Ib (van den Ent & Lowe, 2000). However, in FtsA another domain is inserted at the barbed end of domain Ia, which makes contacts that compensate for the lost interaction surfaces (Szwedziak, *et al.* 2012). Instead of inserting another subdomain, AlfA has compensated through altered assembly interfaces, including a more extensive and continuous cross-strand interface. The divergent structure of AlfA highlights the extreme evolutionary plasticity of actin filament quaternary structure. This property has been exploited by bacteria to generate a broad range of actin filaments with unique dynamic and functional properties tuned to a wide variety of specific cellular functions. Given that only a small number of bacterial actins have been structurally and functionally characterized, it is likely that further functionally important variation in filament morphology and dynamics remains to be discovered.

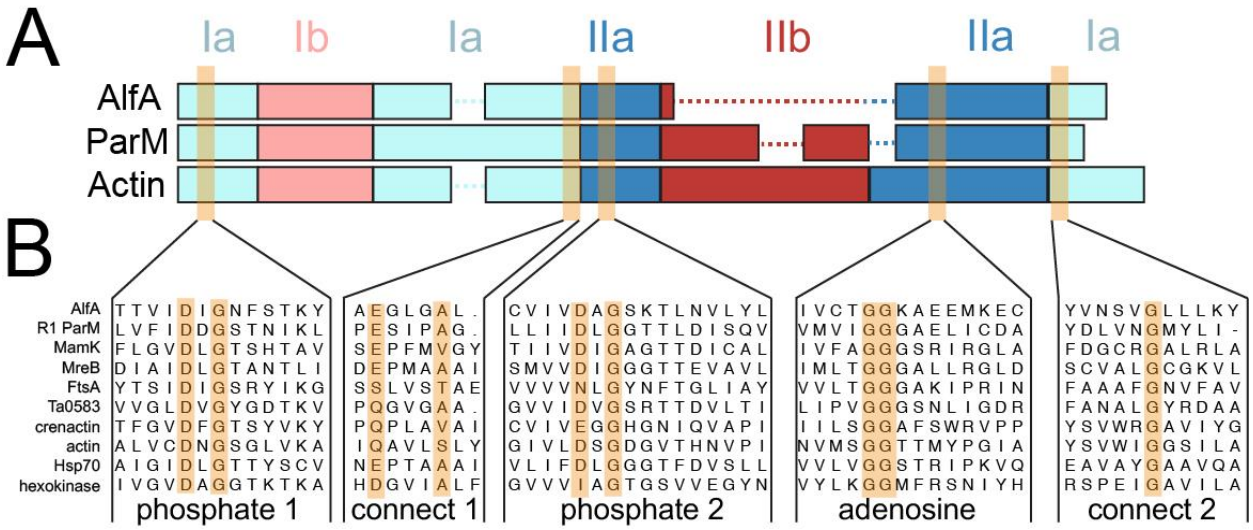

Figure 3.1: AlfA sequence conservation. (A) Diagram of domain arrangements for AlfA, the bacterial actin ParM from the E. coli R1 plasmid, and vertebrate actin. The five conserved actin sequence motifs surrounding the actin binding cleft are highlighted in orange. (B) Sequence alignments of AlfA with other actins, Hsp70, and hexokinase in the regions surrounding the five conserved motifs. Universally conserved residues in each motif are highlighted in orange.

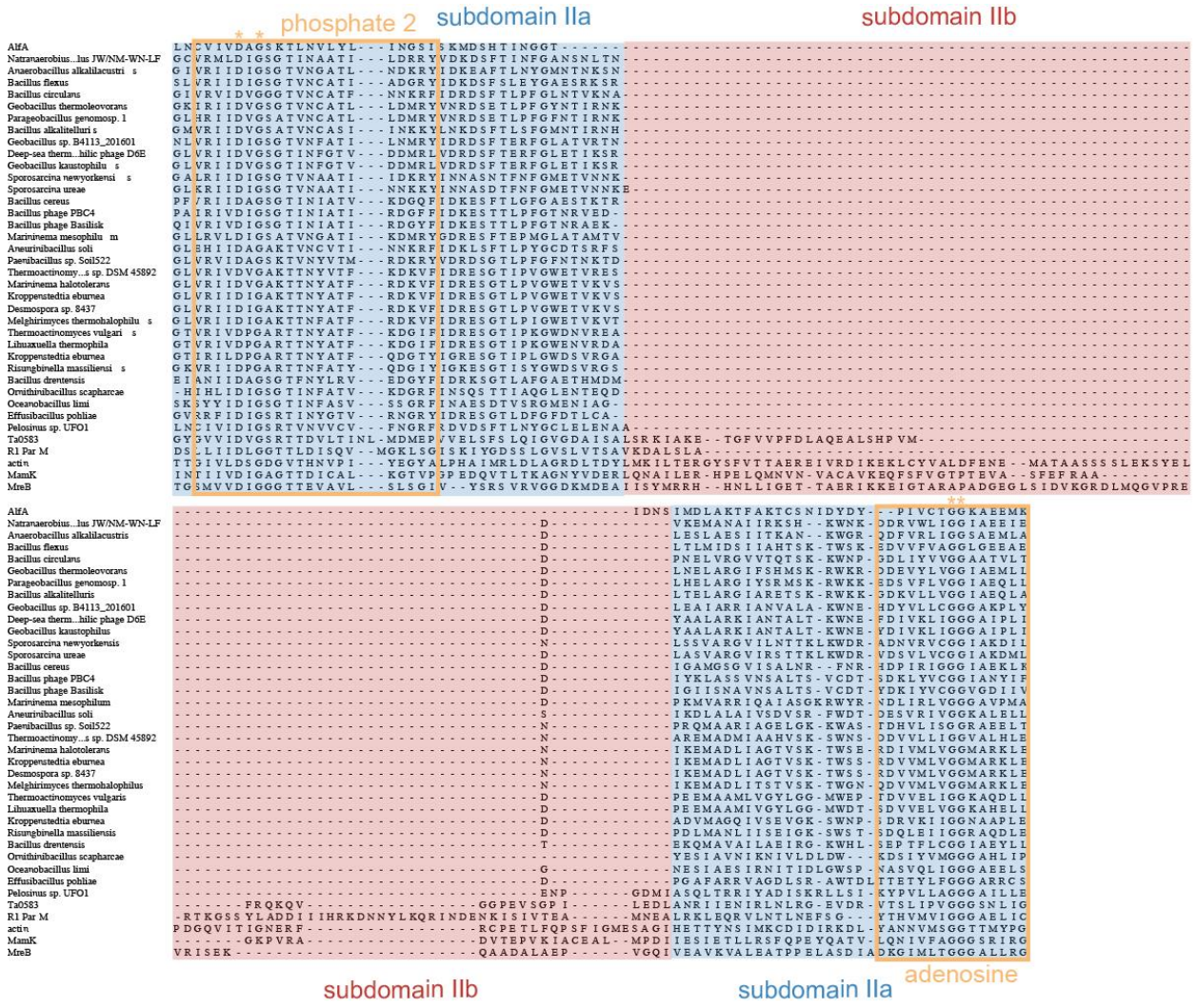

Figure 3.2: Sequence alignments of domain II. Multiple sequence alignment of subdomain IIb (red) and flanking regions in subdomain IIa (blue), demonstrates a family of bacterial and phage actins that lack subdomain IIb. The conserved phosphate 2 and adenosine motifs are outlined in orange and universally conserved residues highlighted with asterisks. The overall sequence identity between AlfA and other actins missing subdomain IIb is ~20%, while the identity to other bacterial actins is between 11% and 15%.

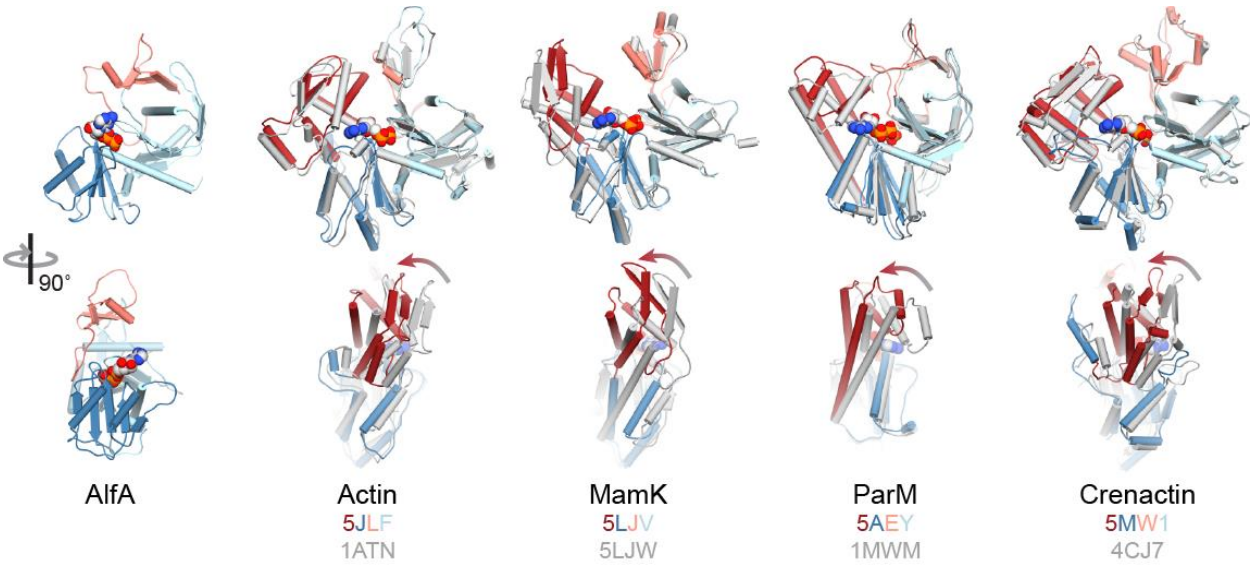

Figure 3.3: Conformational differences between free and filament-bound actins. Four different actins are show in their free conformations from crystal structures (gray) and filament-bound conformations from high-resolution cryo-EM reconstructions (color). In each case the major conformational change is a rotation of domains I and II relative to each other, yielding a flatter protomer in the filament. Arrows indicate the direction of the conformational change. The structure pairs were aligned on domain Ia in each case. PDB ID codes are indicated for both states.

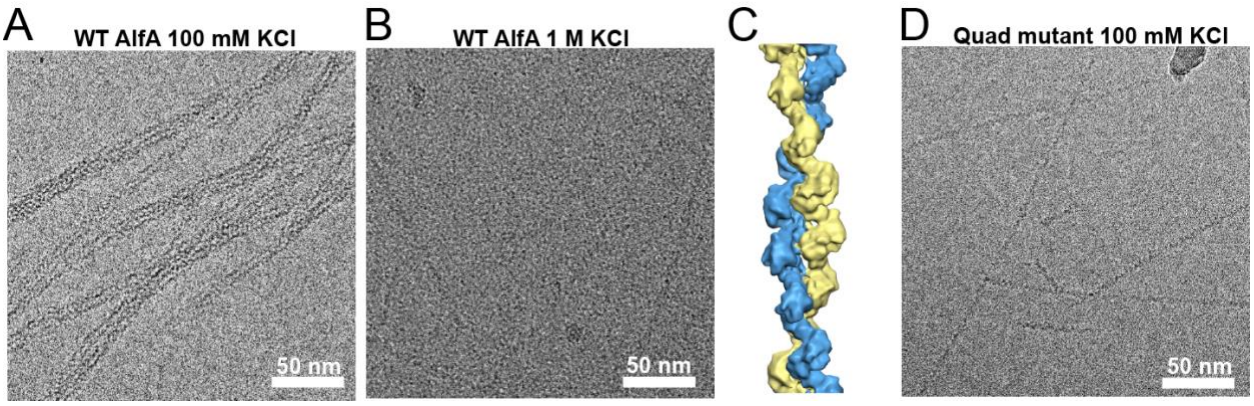

Figure 3.4: Optimization of AlfA cryo-EM samples. (A) Cryo-EM image of AlfA at 100 mM KCl, where single filaments laterally associate into bundles with irregular thickness. (B) Cryo-EM image of AlfA at 1 M KCl, where bundle formation is inhibited but increased solvent density reduces contrast with the filaments. (C) Reconstruction at 12-Å resolution of AlfA filaments in 1 M KCl. (D) Cryo-EM image of AlfA with four surface lysines (K21, K22, K101, K102) mutated to alanine (the "quad" mutant), which inhibits bundling at low salt concentration. Images in B and D are both at −1.5-μm defocus.

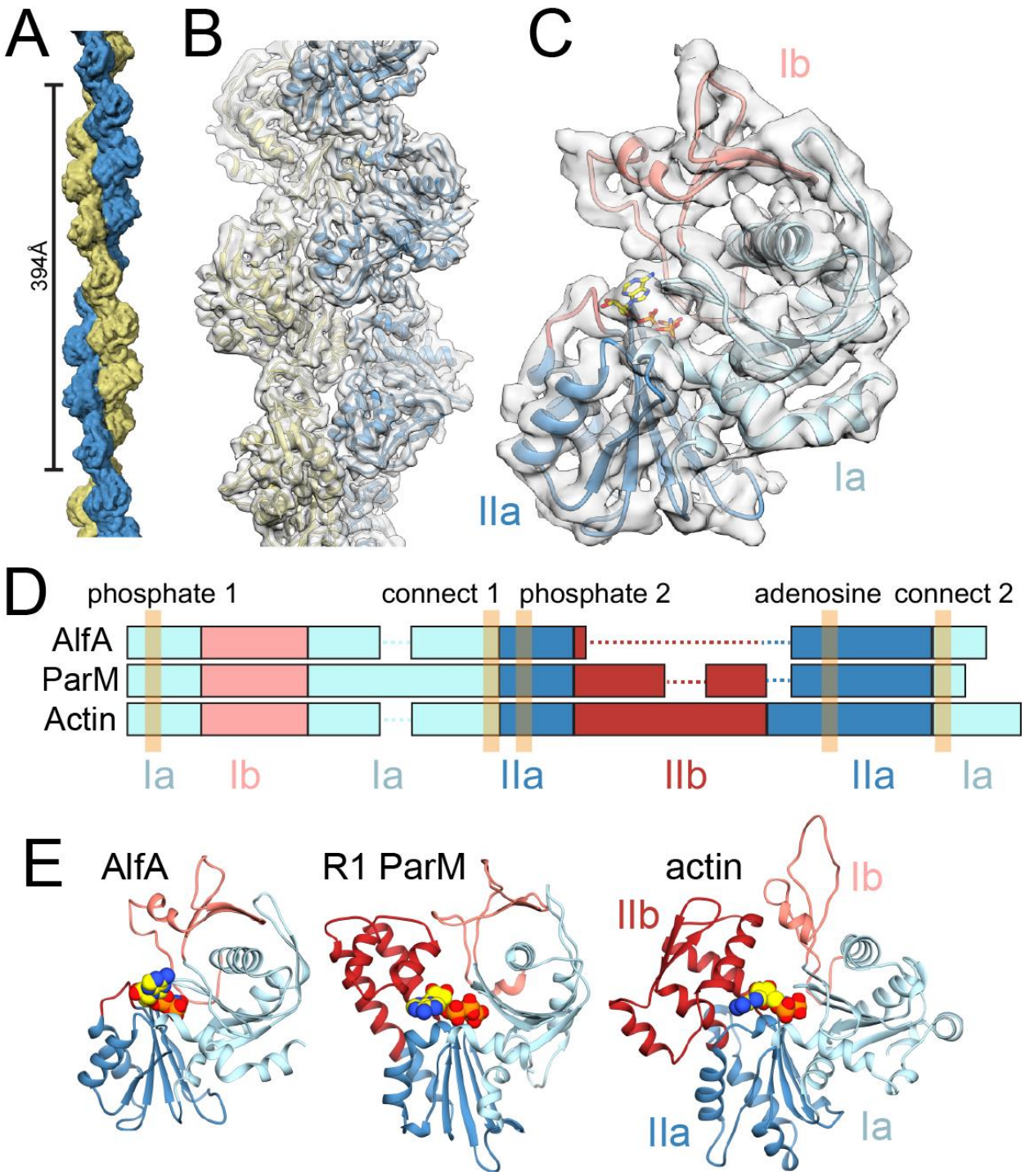

Figure 3.5: Cryo-EM structure of the AlfA filament. (A) The two-stranded AlfA filament with a pitch of 394 Å. The pointed end is at top and barbed end at bottom throughout all of the figures. (B) The atomic model fit into a segment of cryo-EM density. (C) A single AlfA protomer from the reconstruction colored by subdomain. (D) Protomers of different actin filaments, with bound nucleotides in yellow, share a conserved fold, but AlfA is missing subdomain IIb.

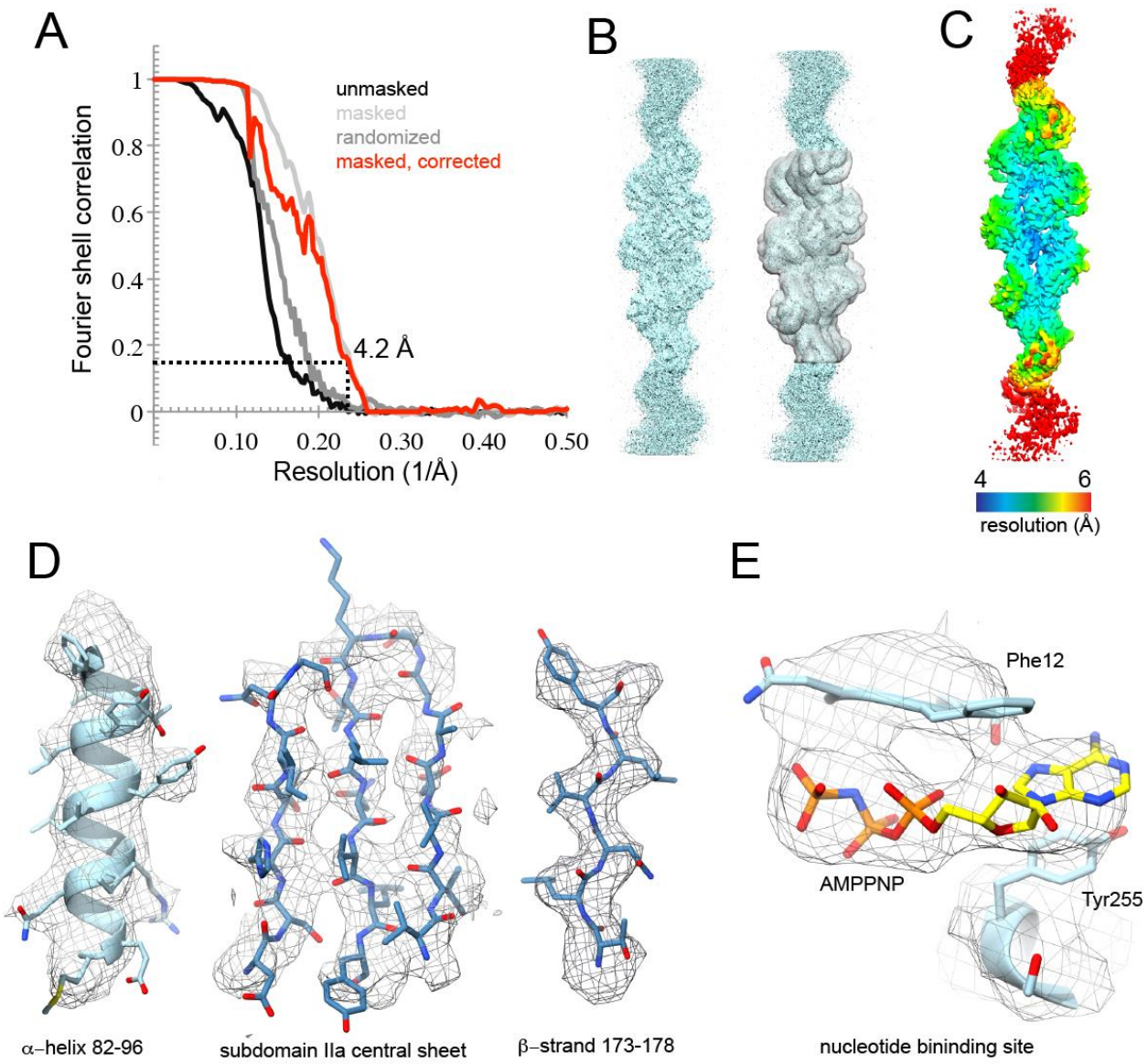

Figure 3.6: Cryo-EM reconstruction of AlfA. (A) FSC curves for final AlfA reconstruction. The final resolution calculated from the masked filament and corrected for masking effects is 4.2 Å. (B) One unfiltered half map from the final reconstruction, shown with the mask used for calculating the FSC curves in A (Right). (C) Local resolution estimate calculated in RELION. (D) Regions of representative density in the structure. (E) Cryo-EM density in the nucleotide binding site.

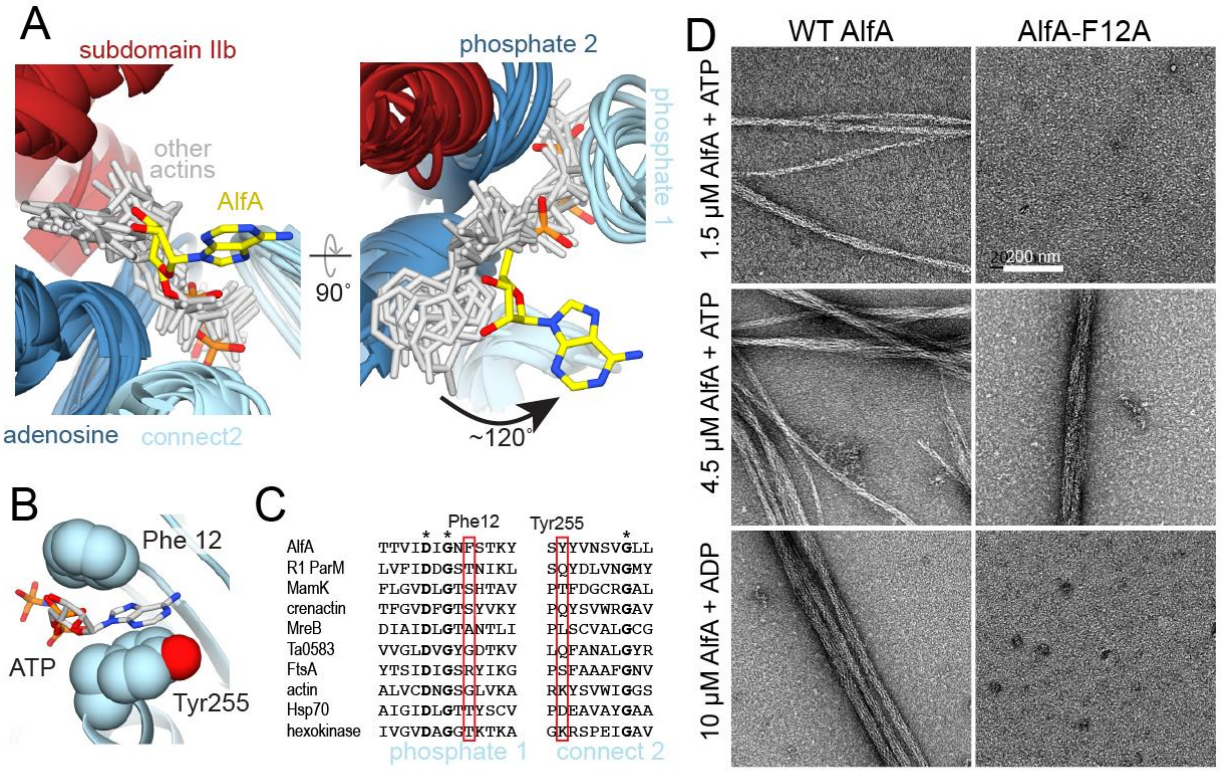

Figure 3.7: AlfA binds ATP through novel interactions. (A) Structural alignment of ATP binding sites of AlfA and other homologs of the actin/Hsp70/sugar kinase family bound to nucleotide, with the proteins rendered as ribbons (colored by subdomain as in Figure 1), and nucleotides rendered as sticks (gray and yellow). The aligned structures are from cryo-EM filament reconstructions (PDB ID codes: actin, 5JLF; MamK, 5JLV; R1 ParM, 5AEY; crenactin, 5MW1), and crystal structures (PDB ID codes: MreB, 4CZJ; Ta0583, 2FSN; FtsA, 1E4G; Hsp70, 3KVG; hexokinase, 2E2Q). Structural alignment was performed using just the regions around the conserved actin sequence motifs. (B) In the AlfA filament structure the adenosine base is sandwiched between Phe12 and Tyr255 in subdomain Ia. (C) Sequence alignment of the phosphate 1 and connect 2 actin motifs, with positions of Phe12 and Tyr255 highlighted in red. Invariant positions are marked with an asterisk. (D) Negative-stain electron micrographs of AlfA wild-type and F12A mutant in the presence of ATP and ADP. The F12A mutation is capable of assembling filaments but cannot maintain stable filaments in ADP.

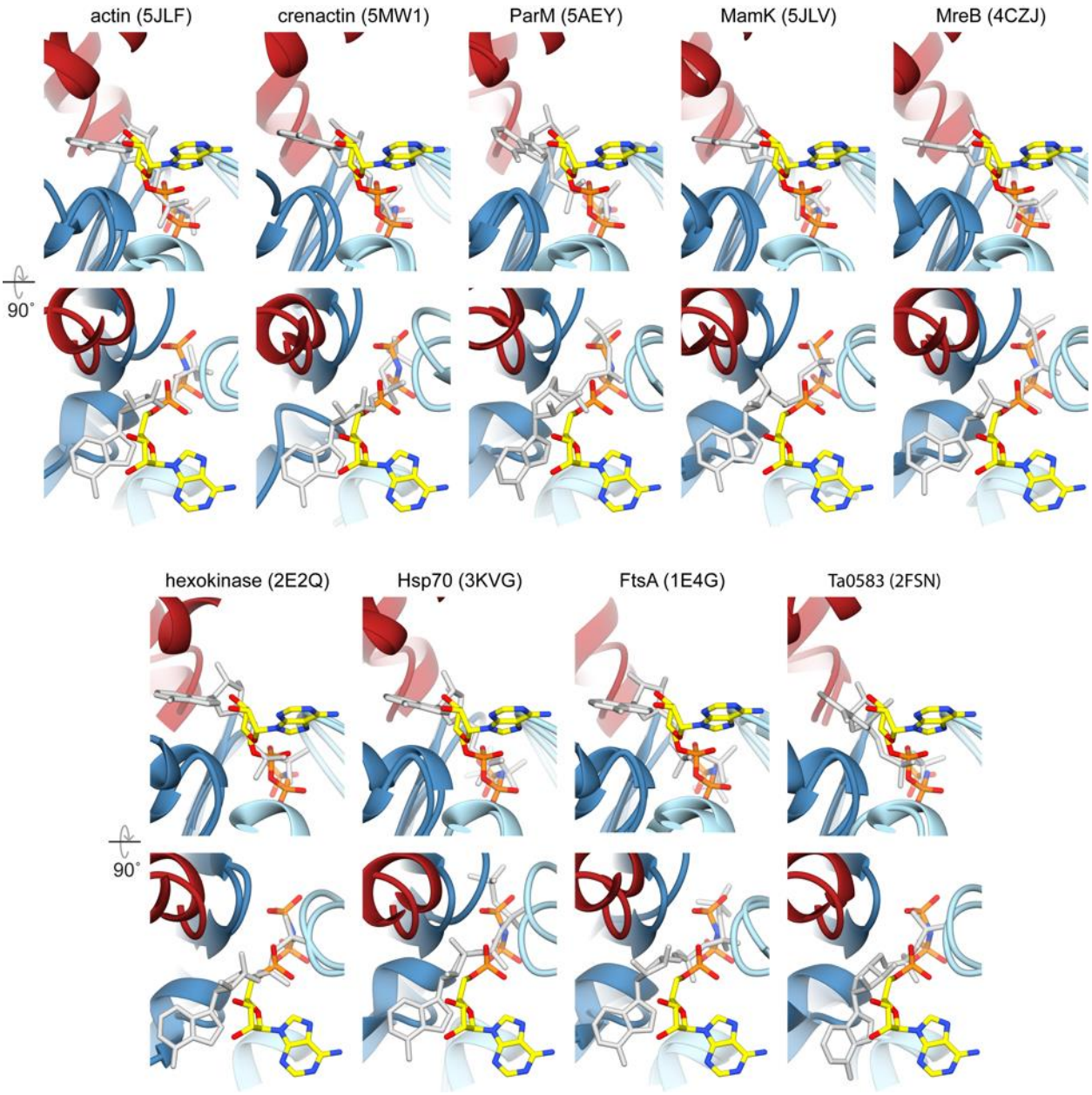

Figure 3.8: Comparison of AlfA ATP binding with other actin homologs. In each panel the AlfA ATP-binding site is superimposed on the binding site of an actin homolog. The coloring is as in Figure 3, with the AlfA ATP in yellow and the homolog ATP in gray.

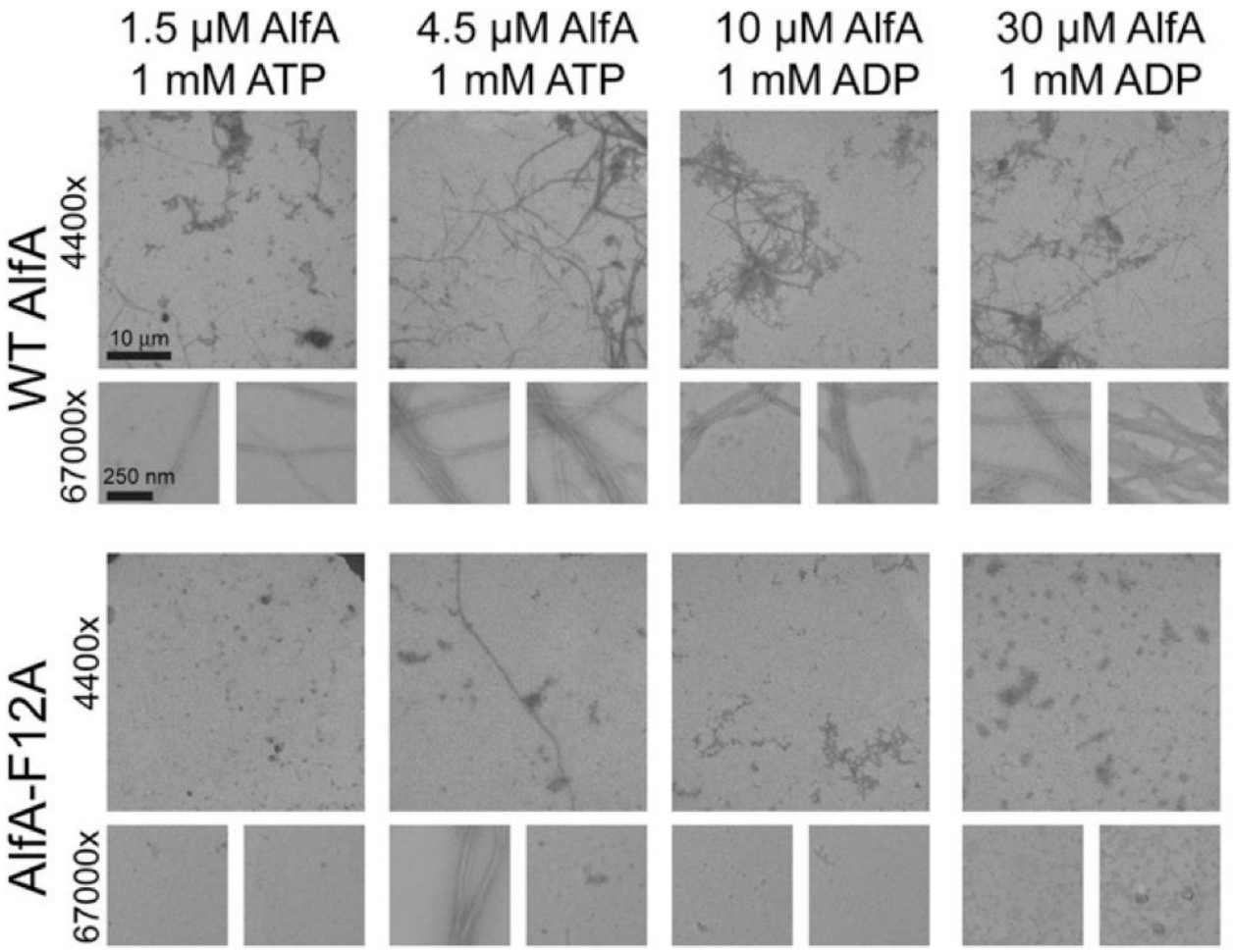

Figure 3.9: Analysis of AlfA-F12A assembly in the presence of ATP and ADP. Representative low-magnification (4,400×) and high-magnification (67,000×) images of negatively stained wild-type and F12A AlfA. For each condition a set of randomly targeted high-magnification images was acquired, and high-magnification images were scored as either having AlfA polymer or not, as quantified in Table S2.

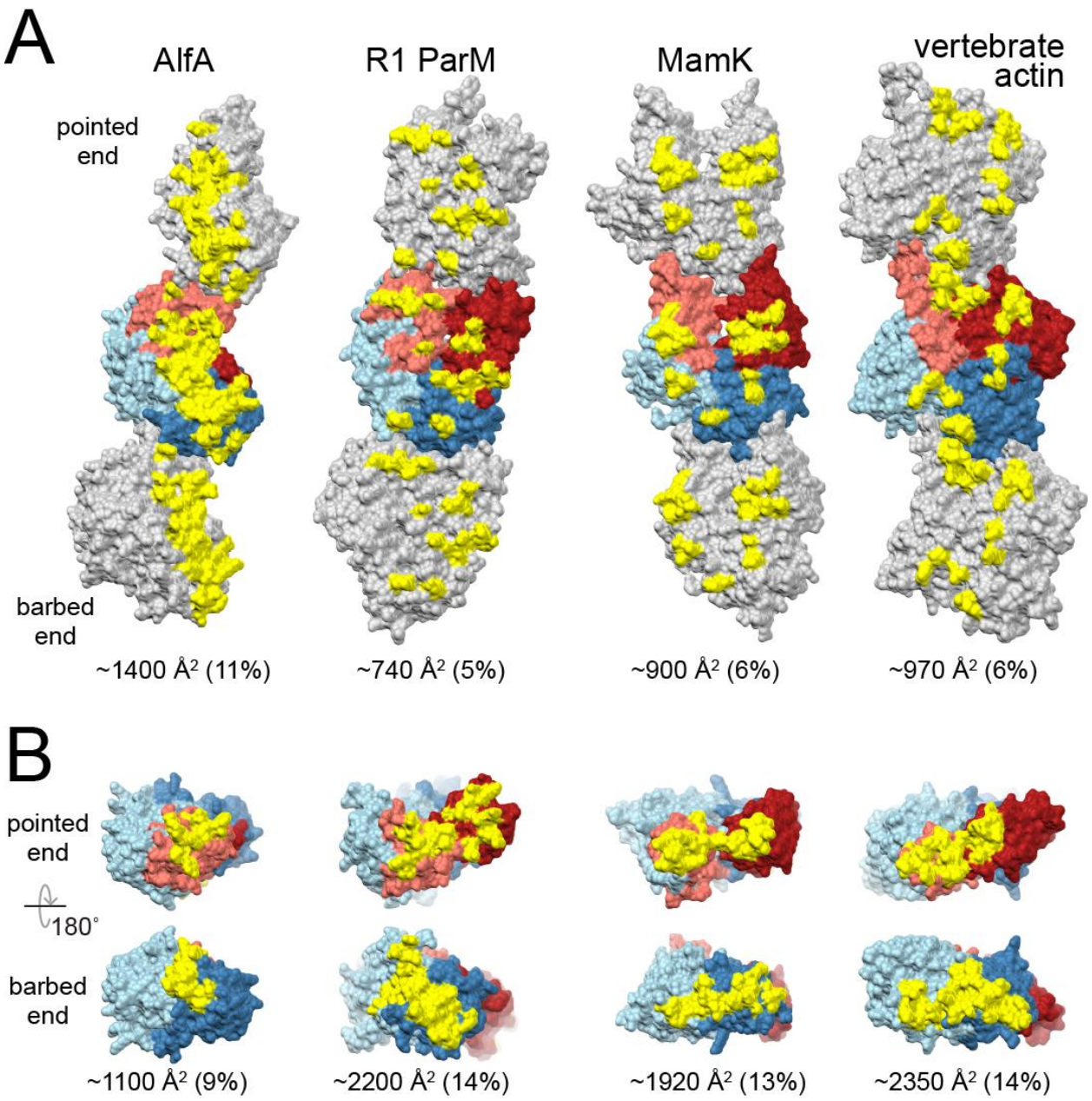

Figure 3.10: Increased AlfA interstrand contacts compensate for missing subdomain IIb interactions. (A) Three protomers from single strands of AlfA and three other actins are shown, with the central protomer colored as in Figure 1. Residues involved in cross-strand interaction surfaces are colored yellow. (B) Single protomers with residues involved in longitudinal interacting surfaces colored yellow. The size of each interface is given as both absolute area per protomer and as a fraction of the total surface area of the protomer.

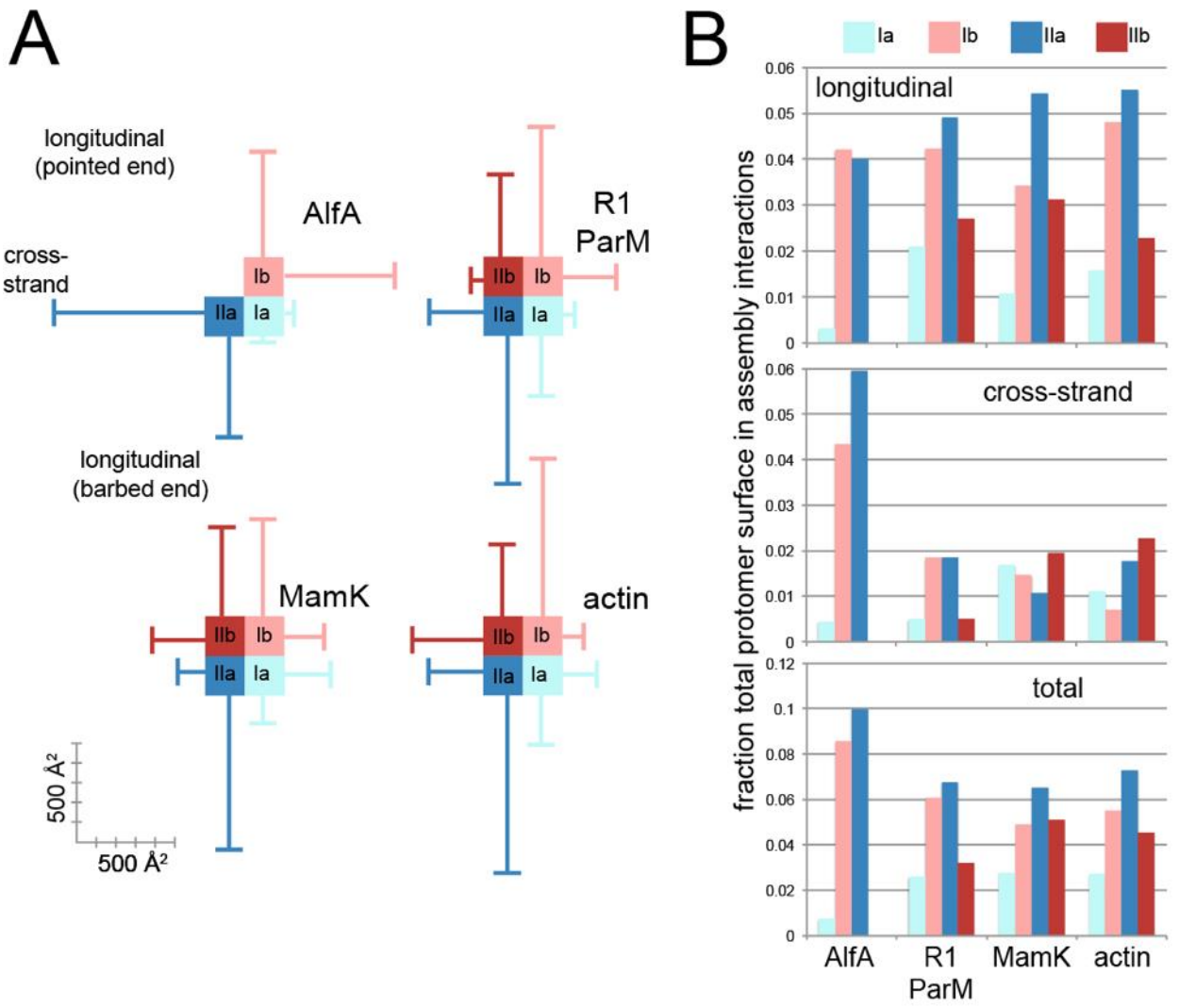

Figure 3.11: Evolutionary variation in the contribution of different subdomains to actin assembly interfaces. (A) For each actin the area of interaction surfaces for each subdomain is plotted, showing contributions to longitudinal (vertical lines) and cross-strand (horizontal lines) interfaces. Scale bar at the Bottom Left indicates size of interfaces in Å^2. (B) The relative size of assembly interfaces for each subdomain are plotted as a fraction of total protomer surface area.

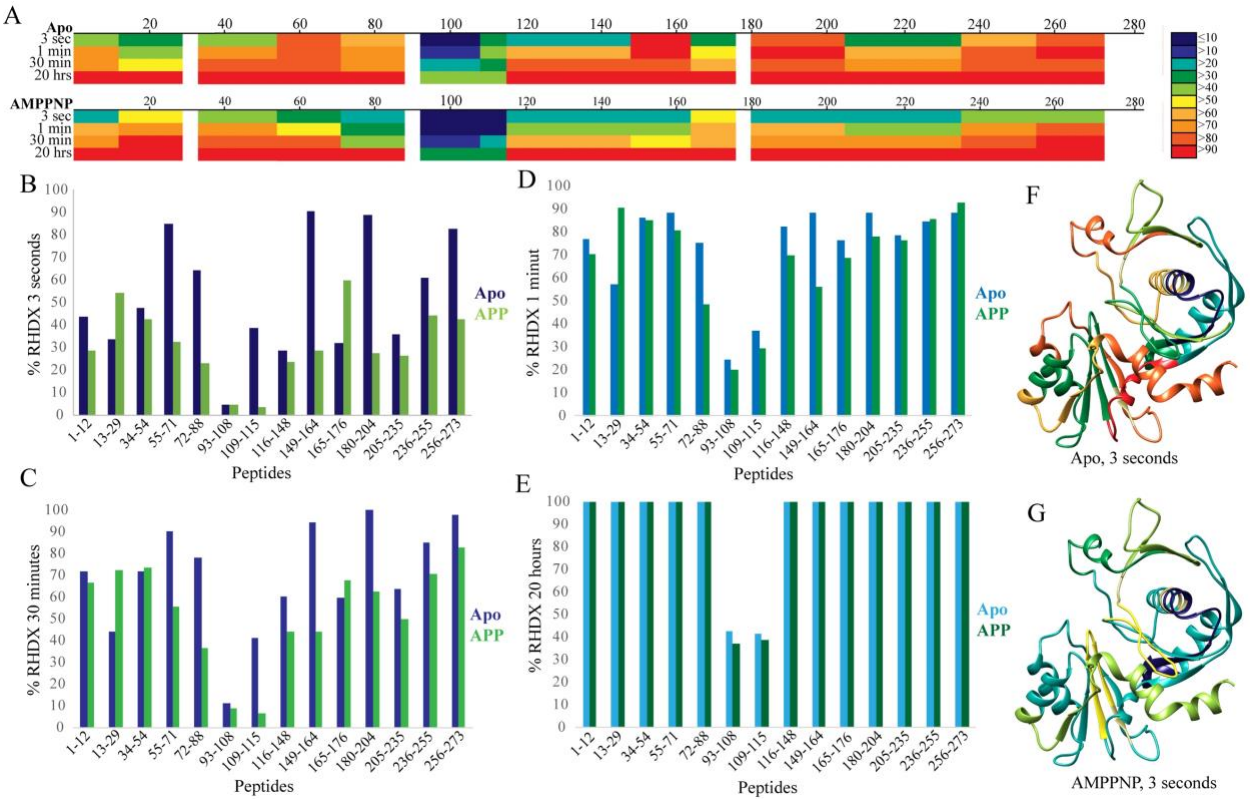

Figure 3.12: AlfA has different deuterium uptake in apo and ATP-bound states. AlfA was treated with D_2O in both apo and nucleotide-bound state. For both conditions, reactions were quenched after 3 seconds, 1 minute, 30 minutes or 20 hours. (A) Relative hydrogen-deuterium exchange rates (RHDX) of the selected subset of peptides are shown as a heat map for apo (top) and AMPPNP bound states (bottom). Relative exchange rates of each time point were calculated with respect to the undeuterated AlfA. 100% relative deuteration level was determined as the amount of deuterium that AlfA can uptake when denatured with heat and acid treatment. (B-E) Relative exchange rates of unbound (apo) and AMPPNP-bound (APP) state of AlfA at 3 seconds (B), 1 minutes (C), 30 minutes (D) and 20 hours (E) of exchange. (F) Relative exchange rates of AlfA after 3 seconds of exchange at apo state. (G) Relative exchange rates of AlfA at AMPPNP bound state after 3 seconds of exchange.

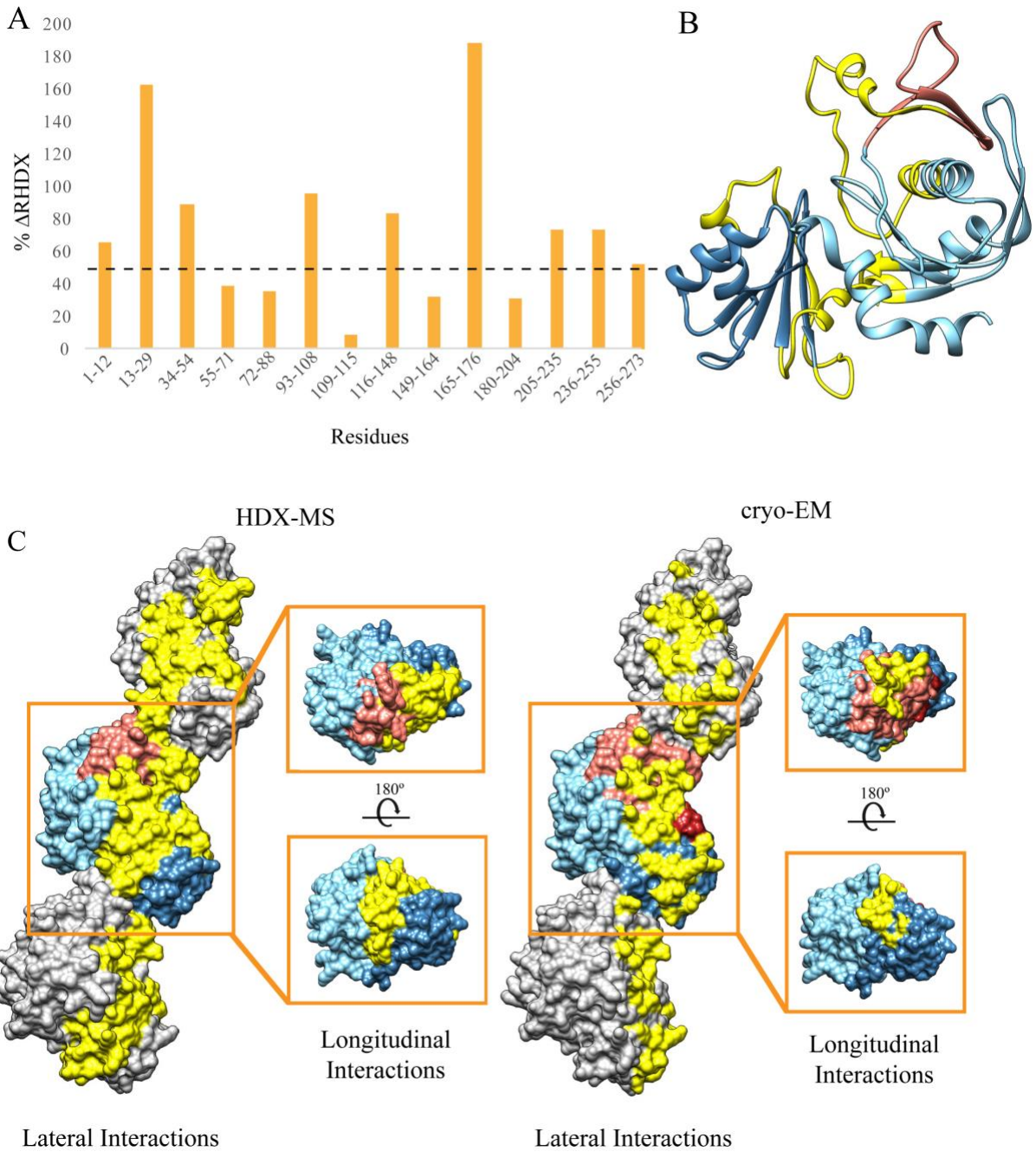

Figure 3.13: Regions of AlfA have different accessibility for hydrogen-deuterium exchange upon nucleotide binding. (A) Changes in relative exchange rates of AlfA in apo state and nucleotide bound state were compared with each other by using their relative exchange rates after 3 seconds. Dashed line shows 50% cutoff. Change in the exchange rate of nucleotide bound state relative to the exchange rate of apo state has been calculated for each peptide. (B) Five regions that have the largest decrease in the exchange rate upon nucleotide binding are mapped onto the atomic model of AlfA (yellow). Subdomains were colored as in Figure 1. (C) Regions are mapped on the filament structure and compared to the regions that are involved in lateral and longitudinal contacts that form the filament structure.

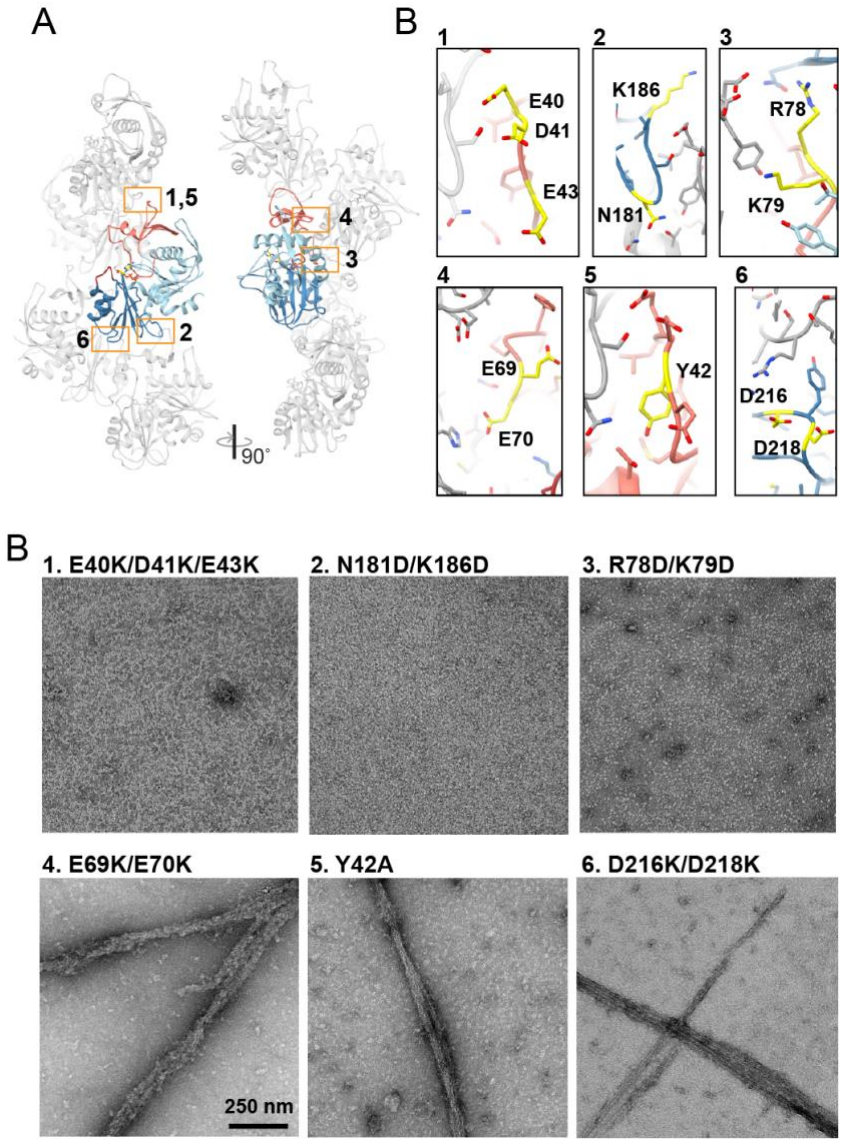

Figure 3.14: AlfA assembly mutants. Six assembly mutants were designed on the basis of and AlfA homology model fit into a preliminary 12-Å reconstruction of the AlfA filament. (A) Atomic model of the AlfA filament with a single protomer colored as in Figure 3.5, with locations of designed assembly mutants indicated by orange boxes. (B) Close-up views of the different designed mutations (yellow) in the final refined structure. (C) Quantification of mutant polymerization by filament pelleting assay. The fraction of each mutant pelleted by ultracentrifugation is plotted for each mutant (n = 5, error bars represent SEM). The severity of polymerization defects appears to correlate with the position of the residue with respect to the interface in the final structure. For example, while Tyr42 is close to the longitudinal interface, its side-chain is pointed away from the neighboring protomer in the final model and so its mutation to alanine has a negligible effect on polymerization. On the other hand, the side-chain of Lys79 is pointed directly across the interface at the neighboring protomer, explaining why mutation at this site severely inhibits polymerization. (D) Representative negative-stain images of AlfA designed assembly mutants.

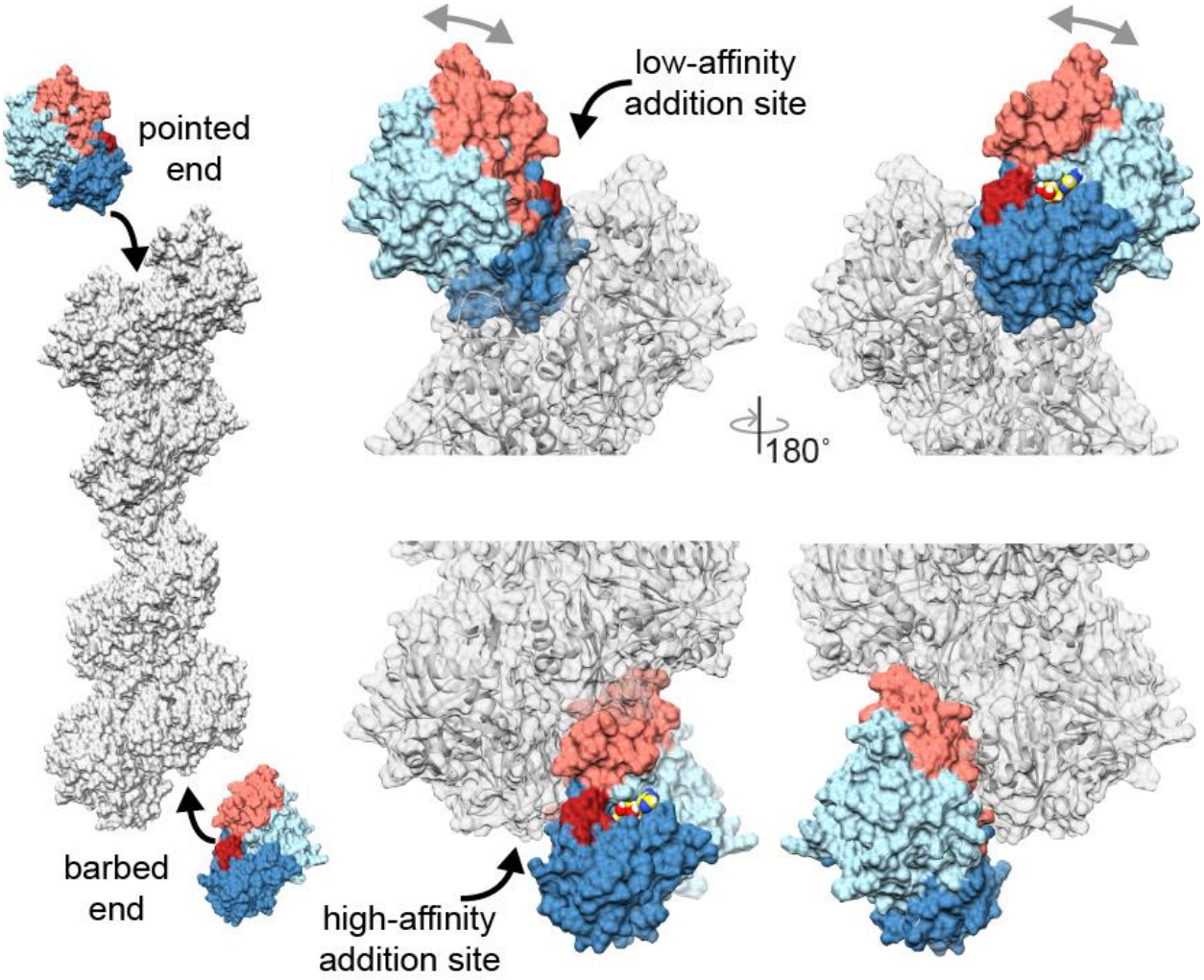

Figure 3.15: Structural differences between protomer addition at barbed and pointed ends. (A) New protomers would add to the pointed end only through interaction with subdomain IIa, which leaves domain I free to rotate relative to domain II (gray arrows). In contrast, addition at the barbed end involves interactions with both subdomains Ib and IIa, stabilizing a filament-bound conformation. Flexibility at the terminal pointed end protomer would create a very low-affinity addition site, while the more rigid conformation of the terminal protomer at the barbed end would create a more defined high-affinity site, potentially explaining the observed unidirectional elongation of AlfA.

CHAPTER IV - Interplay between the components of AlfA-driven segregation system

4.1. Introduction

Actin is essential for the survival of many organisms due to its central role in many cellular functions (Pollard & Cooper, 1986). Polymerizing into filaments and performing cellular functions like cell division, cellular migration and organelle positioning requires complex regulation of actin at many levels (Pollard & Cooper, 2009). Spatial and temporal regulation of filament nucleation, elongation, branching, bundling, and disassembly are essential for actin's cellular functions (Gunning *et al.,* 2015). This complex regulation of actin in eukaryotes is provided by a myriad of actin-binding proteins (ABPs) (dos Remedios *et al.,* 2013). The presence of more than 100 ABPs in budding yeast and many more in multicellular eukaryotes creates strong evolutionary constraints on actin sequence and allows actin filaments to serve as a universal scaffolding protein for many different cellular processes (Lappalainen, 2016).

Regulation of actin homologs in prokaryotes is quite different from eukaryotic actin due to relaxed evolutionary constraints. Having a smaller number of interaction partners allowed bacterial actins to have a larger exposed surface that can diverge into different filament structures specialized for different functions (Ozyamak *et al.,* 2013). This "one-filament-one-function" approach, which requires an actin homolog and a unique filament system for each associated biological function, allowed prokaryotes to maintain much simpler systems that can be regulated with only a few interaction partners (Gunning *et al.,* 2015).

Type II plasmid segregation systems contain a single actin-binding protein encoded by the plasmid itself (Campbell & Mullins, 2007). Actin-binding proteins of type II segregation systems serve as an adaptor between the motor protein and the centromere-like region on the plasmid for faithful segregation of the low-copy number plasmids during cell division or sporulation (Jensen

& Gerdes, 1997; Tanaka, 2010). The best-characterized type II segregation system is the *par* operon of *Escherichia coli* plasmid R1. The *par* operon contains the cytomotive filament ParM, centromere-binding protein ParR and centromere-like sequence *parC*. *parC* is the 160 bp centromere-like DNA sequence on E. coli R1 plasmid that consists of 10 tandem repeat sequences (Jensen *et al.,* 1998). Binding of ParR to the tandem repeats of *parC* via their ribbon-helix-helix (RHH) motif forms a protein-DNA complex called the segresome (Schumacher et. al, 2007). Dynamically unstable ParM filaments experience rapid cycles of growth and shrinking until they are stabilized by their interaction with the segresome. Upon binding to the segresome complex, ParM filaments decrease their dynamic instability. The rapid disassembly of the dynamically unstable cargo-free ParM filaments supplies free ParM monomers for the elongation of cargo-bound filaments. Insertional polymerization from the barbed end via a formin-like mechanism allows plasmids to be pushed to the opposite poles of the cells, which ensure that each daughter cell receives a copy of the plasmid upon cell division (Gayathri *et al.,* 2012).

Like the *par* operon, the *alf* operon of *Bacillus subtilis* plasmid pLS32 is composed of three elements; the cytomotive filament AlfA, the DNA-binding protein AlfB, and the centromere-like sequence *parN*. Unlike ParM, AlfA does not show signs of dynamic instability (Polka *et al.,* 2009; Polka *et al.,* 2014). The absence of dynamic instability requires AlfA filaments to be regulated with a mechanism that will ensure cargo-attachment and maintain the concentration of monomeric AlfA at a level that is sufficient to elongate cargo-attached filaments. The adaptor protein of the *alf* segregation system, AlfB, adapted a dual role to regulate AlfA dynamics: free AlfB suppresses AlfA growth and promotes disassembly of ADP-bound filaments, while AlfB–*parN* complexes nucleate AlfA filaments (Polka *et al.,* 2014). The dual activity of AlfB ensures that filaments grow primarily from plasmids and prevents spontaneous nucleation of the filaments to drive plasmid

segregation. At the molecular level, AlfB might perform its dual role in two different ways; i) AlfA interacts with both AlfB and the segresome using the same surface and the presence of *parN*-bound AlfB localizes AlfA monomers to form a nucleus ii) AlfB interacts with AlfA via different surfaces so it can bind to one surface to sequester AlfA monomers and another surface to promote assembly.

Here we investigate the dual role played by AlfB and how it affects AlfA filament dynamics using various biochemical and biophysical methods. We reconstituted the segresome complex *in vitro* and confirmed the expected stoichiometric ratio of AlfB and *parN* interaction. Using size exclusion chromatography (SEC) and size exclusion chromatography coupled with multi angle light scattering (SEC-MALS), we purified the segresome complex and determine its molecular weight. Electron microscopy and dynamic light scattering (DLS) allowed us to observe that segresome complex nucleates AlfA filaments at lower concentrations while preventing filament formation near equimolar ratios, suggesting that the segresome complex can sequester AlfA monomers. Our croslinking mass spectrometry (XL-MS) results showed that there is no significant difference between the AlfA monomer-AlfB interaction surfaces in free AlfB or the segresome complex. Finally, we purified the third protein of the *alf* operon, AlfC, and investigated its interactions with the other protein components of the system using pelleting assays, finding that AlfC does not directly interact with AlfA.

4.2. Results

4.2.1. Reconstitution of segresome complex *in vitro*

Previous studies have indicated that AlfB interacts with *parN* as a dimer, and this interaction between AlfB and *parN* reduces the critical concentration for AlfA assembly (Polka *et al.*, 2014). However, the effects of the segresome on AlfA dynamics were investigated by mixing

the components of the AlfA-driven segregation system together, rather than with a stoichiometrically purified, homogenous segresome complex (Polka *et al.,* 2014). We decided to reconstitute the segresome complex *in vitro* and use this predefined tool to further investigate the dual role played by AlfB.

We used a synthesized *parN* region with two base pair overhangs on each end to prevent the non-specific binding of AlfB to DNA. Assuming one AlfB dimer binds to each repeat of *parN*, we have reconstituted and purified the segresome complex by using the stoichiometric ratio of 1:6 (Figure 4.1A, B). Using both ethidium bromide (EtBr) and Coomassie stains enabled us to detect the DNA-protein complex using the same non-denaturing gel (Figure 4.1D). We used size exclusion chromatography coupled with multi-angle light scattering (SEC-MALS) for accurate determination of the molecular weight of the purified segresome complex. An 85 kDa complex detected by multi angle light scattering, aligned with our predictions (Figure 4.1C). However, native PAGE analysis indicated the presence of two species eluted at the same time from the chromatography column with a slight difference in the molecular weight (Figure 4.1D). We hypothesized that the difference in molecular weight might indicate a temporary dissociation of the complex due to low-affinity binding. *parN* contains two identical repeats (Repeat 1) and one repeat that differs by one base (Repeat 2). We decided to test how repeating sequences affect the integrity of the segresome complex by altering the repeating sequences of *parN*.

Without changing the overhangs and the sequences in between the repeats, we altered the repeating sequences to be either all Repeat 1 or all Repeat 2. Size exclusion chromatograms and native PAGE analysis of segresome complexes made with wt *parN*, all Repeat 1 *parN* and all Repeat 2 *parN* showed that there is no significant difference between the complexes, suggesting

that AlfB binds to the repeating sequences with similar affinity and the secondary band with the lower molecular weight might be due to a temporary release of an AlfB dimer (Figure 4.1E, F).

4.2.2. AlfA filament interactions with AlfB and segresome

It has been shown previously that AlfA interacts with both free and segresome-incorporated AlfB, and the segresome complex is bound mainly to the growing ends of AlfA filaments (Polka *et al.*, 2014). While previous studies have shown that free AlfB inhibits polymerization by sequestering AlfA monomers and rapidly disassembles the AlfA filaments assembled by ATP, we sought to test whether AlfB could bind to stabilized AlfA filaments using pelleting assays. The non-hydrolysable ATP analog, AMPPNP, was used to polymerize AlfA and test whether free AlfB can directly interact with AMPPNP-stabilized AlfA filaments. We titrated AlfB from 5 µM to 40 µM in solution while keeping the AlfA concentration constant at 10 µM. This allowed us to determine the amount AlfB interacting with AlfA filaments by pelleting AlfA and any associated AlfB using ultracentrifugation. The amount of AlfA pelleted in each reaction remained constant, while the amount of AlfB increased in the pellet as the concentration of AlfB used in each reaction increased (Figure 4.2A). In each reaction, ~ 7 µM of the AlfA used were pelleted. On the other hand, the amount of AlfB pelleted with the AlfA filaments increased as the concentration of AlfB added to the reaction increased, and reached the same amount of AlfA pelleted (Figure 4.2B). When 10 µM AlfA treated with 40 µM AlfB, we observed that AlfB interacts with AlfA at equimolar ratio, suggesting a stoichiometric binding of AlfB to AlfA filaments. We attempted to image AlfA-AlfB interactions under these conditions by negative stain electron microscopy, but the high protein concentrations required to see robust interaction made it difficult to detect binding in the crowded background (Figure 4.2C). Together, these results

support the previous findings that AlfB interacts with monomeric AlfA to sequester their incorporation into the filament and interacts with AlfA filaments to initiate disassembly upon ATP hydrolysis (Polka *et al.*, 2014).

We used the same experimental design to investigate the interactions between predefined segresome complex and AlfA filaments. Previous work showed that segresomes nucleate AlfA filament assembly at low stoichiometric ratios (Polka *et al.*, 2014). We sought to determine the effects of segresomes on AlfA dynamics at higher stoichiometric ratios and whether they could inhibit assembly. We used 10 µM AlfA and titrated AlfA with segresome (5 µM, 10 µM, 20 µM and 40 µM) in the presence of AMPPNP. We observed that the concentrations of segresome used in our pelleting assays strongly inhibits AlfA polymerization. Additionally, we observed all the segresome used stayed in the supernatant, independent from the concentration used (Figure 4.3). This suggests that at high stoichiometric ratios AlfB can inhibit polymerization in both its free form and in the segresome form (Polka *et al.*, 2014)

4.2.3. Effects of the segresome complex on AlfA polymerization dynamics

It has been previously shown that low concentrations of *parN* are able to nucleate AlfA filaments when added into a reaction mixture that contains AlfA below critical concentration and AlfB (Polka *et al.*, 2014). We have tested the effects of the predefined segresome complex on AlfA polymerization dynamics by using EM. The phenomenon previously observed by Polka *et al.*, has been recapitulated by using the predefined segresome complex below the critical concentration for AlfA assembly (Figure 4A, B). However, consistent with our pelleting assay results (Figure 4.3), further increase in the concentration of segresome caused heterogeneous particles to form instead of AlfA bundles (Figure 4C). Next, we used AlfA above its critical concentration to test the effects

of increasing concentrations of the segresome complex. Increasing concentration of segresome caused AlfA bundles to separate into individual filaments (Figure 4D), and equimolar ratio of AlfA and segresome caused these filaments to separate further into heterogeneous particles (Figure 4E). To ensure the observations we made by using EM were not an artifact of particle distribution on the grid or sample preparation, we used dynamic light scattering, which determines particle size and distribution in bulk solution (Stetefeld, 2016). We observed a shift in particle radii from a larger range (>1 μm) to a smaller range (≤10 nm) as the concentration of segresome increases in the reaction mixture (Figure 4G). Together with pelleting assays, these results suggest that at lower concentrations, segresomes act as nucleators of AlfA filaments by recruiting AlfA monomers to create a stable nucleus for elongation. However, increasing concentrations of segresome diminishes unbound AlfA pool and decrease the amount of free AlfA monomers that can contribute to elongation.

4.2.4 Investigation of the AlfA-AlfB interaction surfaces by crosslinking mass spectrometry

When AlfB is present alone, it increases the effective critical concentration of AlfA by sequestering AlfA monomers. However, when *parN* is present, the complex formed by AlfB and *parN* nucleates AlfA below its critical concentration (Polka *et al.,* 2014). We decided to investigate whether AlfB possesses these two different activities by utilizing different surfaces of AlfA or AlfB interacts the same surface of AlfA and the presence of *parN* localizes sequestered monomers to serve as a nucleus. We attempted to generate suitable AlfA-AlfB or AlfA-segresome complexes for structural analysis by negative stain or cryo-EM, but were unable to visualize bound AlfB, likely because the relatively weak interactions required high concentrations of AlfB that crowded the field of view.

As an alternative to determine the interaction surfaces between AlfA and AlfB, we decided to crosslink AlfA with AlfB or the segresome complex and analyze the crosslinked peptides using mass spectrometry. To maximize the number of crosslinked peptides and exclude the interference of filament formation, we decided to find conditions that AlfA has been mainly or entirely sequestered by AlfB dimers and the segresome. Since we already determined that equimolar ratio of AlfA and segresome prevents filament formation, we used the same methodology to determine the molar ratio that the filament formation prevented by AlfB alone. Using EM and DLS, we found that a molar ratio around 1:8 is necessary to completely suppress AlfA polymerization in the presence of ATP (Figure 4.5).

We crosslinked 2 µM AlfA with 20 µM AlfB monomers and 4 µM segresome (which contains 24 µM AlfB), respectively. Crosslinking was performed by using disuccinimidyl suberate (DSS) at different time intervals (5, 15, 30 and 45 minutes). Samples were taken from each crosslinking time point for SDS PAGE analysis (Figure 4.6A). We observed higher molecular weight species started to form around 15 minutes and decided to use this sample for mass spectrometry analysis. Using a 1% false discovery rate (FDR) cutoff, we found 131 unique distance restraints (UDRs) between AlfA and AlfB, while there were 96 UDRs between AlfA and the segresome (Figure 4.6B). We observed that all AlfA subdomains were crosslinked to AlfB. However, most of the residues of AlfA crosslinked with AlfB and segresome are located around domain I (Figure 4.6C). When AlfA residues crosslinked with AlfB or the segresome were mapped on the surface of the atomic model of AlfA, we did not see a significant difference between the interaction surfaces (Figure 4.6D). Together, this might indicate that AlfB does not change its interaction surface whether it is in free form or bound to *parN*.

4.2.5. Investigating the role of AlfC

It has been previously reported that the *alf* operon has another open reading frame for a third protein, AlfC. Loss of AlfC was shown to have a little effect on the plasmid stability (Polka *et al.*, 2014). However, AlfC has not been biochemically characterized before. First, we purified SUMO-His tagged AlfC using immobilized metal affinity chromatography and the SUMO-His tag was removed using ubiquitin-like protease (ULP) (Figure 4.7A). Size exclusion chromatography allowed us to remove impurities and obtain purified AlfC, analyzed by SDS PAGE (Figure 4.7B). We used pelleting assays to determine whether AlfC interacts with any of the other components of the AlfA-driven segregation system. We increased the concentration of AlfC from 20 µM to 40 µM while keeping AlfA concentration constant at 20 µM. Pelleting assays showed us that AlfC is not able to form larger assemblies by itself and it does not interact with the filamentous AlfA. When we incorporated AlfB into the reaction and mixed all the protein components of AlfA-driven segregation system at equimolar ratio, AlfC did not seem to contribute into any larger form of assembly (Figure 4.7C).

4.2.6. Conclusions

Stable interactions between the AMPPNP-polymerized AlfA filaments and AlfB supports the previously reported observation that AlfB cannot destabilize ATP-bound filaments. However, sequestration of AMPPNP-bound AlfA by high stoichiometric ratios of segresome complex suggests that free AlfB and the segresome complex might interact with AlfA monomers using the same interaction surface. Reconstitution of the segresome complex in vitro and observing its sequestering effects on AlfA allowed as to investigate sequestration of AlfA monomers and nucleation of AlfA filaments in detail. Crosslinking AlfA monomers with either excess amount of

free AlfB or excess amounts of the segresome complex showed us that the surface AlfA uses to crosslink with AlfB does not change. The large population of crosslinks located in subdomain Ia supports the previously stated argument that AlfB binds to AlfA monomers from the barbed end. The use of the same interaction surface to both nucleate and sequester suggests that *parN* serves as an anchor to localize AlfB dimers, which can recruit AlfA monomers and initiate elongation from the plasmid. Even though insertional polymerization from the barbed end proposed for AlfA elongation during plasmid segregation, it requires further investigation of AlfA-AlfB interactions.

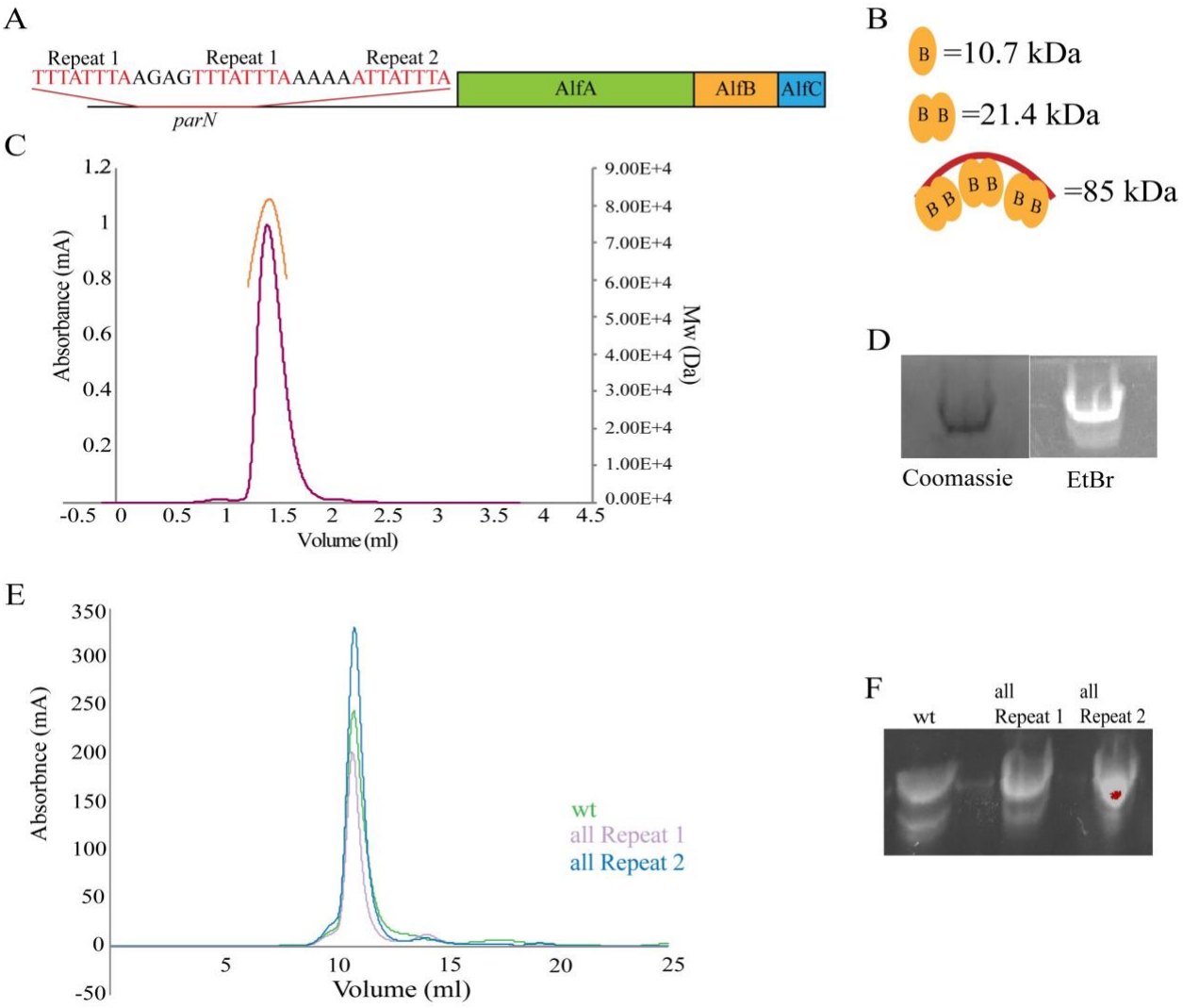

Figure 4.1: In vitro reconstitution of segresome complex. (A) The *alf* operon consists of actin-like protein AlfA, DNA-binding protein AlfB, AlfC of unknown function and the centromere-like DNA sequence *parN*. *parN* consists of three repetitive sequences that are 8 bp-long each. Two of these sequences (Repeat 1) are identical while the third one has one base pair difference (Repeat 2). (B) Complex was estimated to consist of three AlfB dimers binds to *parN* to form an 85 kDa complex. (C) Segresome was reconstituted by mixing purified AlfB and synthesized *parN*. Molecular weight of the complex has been determined around 85 kDa using SEC-MALS. (D) Non-denaturing gel has been stained with both Coomassie (left) and EtBr (right) to detect the protein-DNA complex. (E, F) Segresome complexes that contain either wild type, Repeat 1 or Repeat 2 repeats purified by using SEC and analyzed by using Native PAGE.

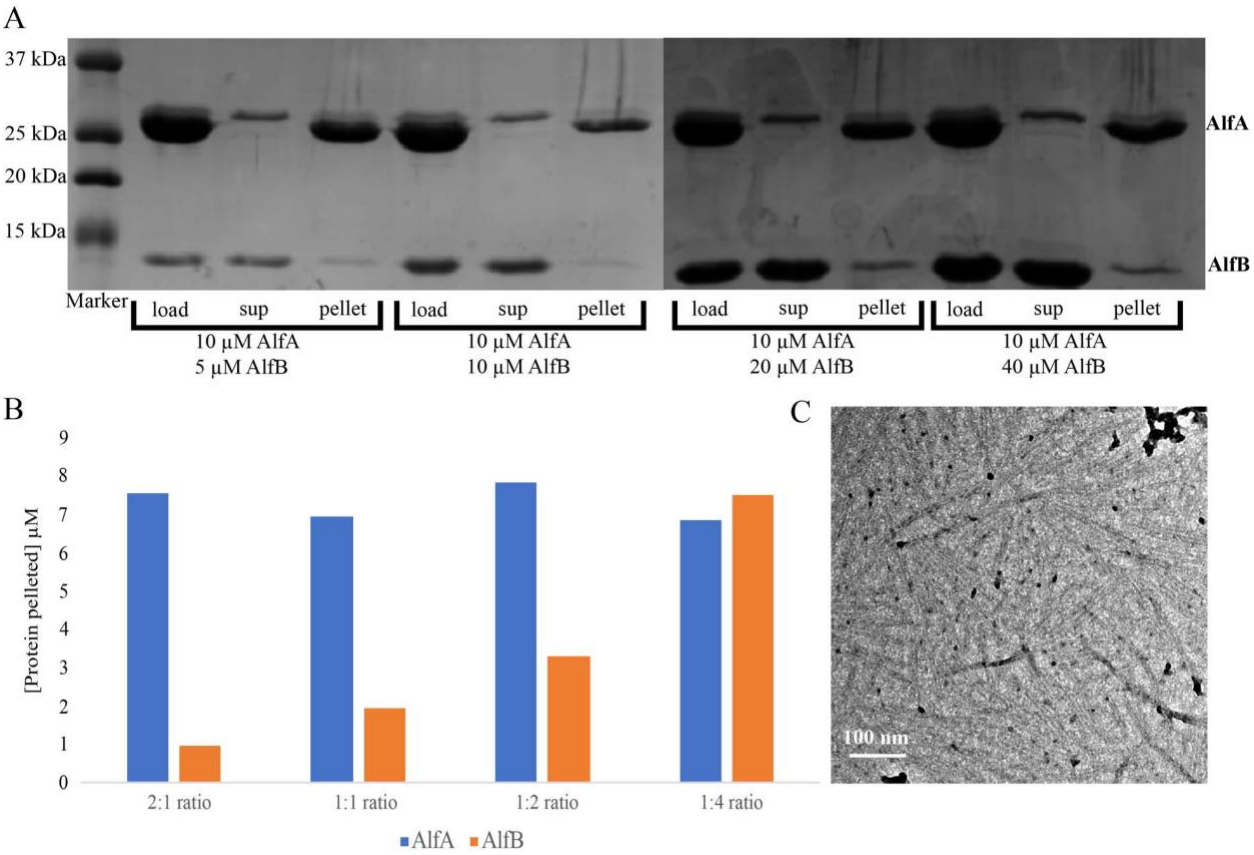

Figure 4.2: AlfB interacts with AlfA filaments. AlfA polymerized in the presence of 5 mM AMPPNP, 5 mM $MgCl_2$ and various concentrations of AlfB. (A) AlfA concentration has been kept constant (10 µM) while AlfB concentration has been increased (5 µM, 10 µM, 20 µM and 40 µM) in the reaction mixtures. Samples were taken from pre-centrifuge reaction mixtures (load) and supernatants (sup) for SDS-PAGE analysis. Pellets were dissolved using depolymerization buffer and samples were taken for SDS PAGE analysis. (B) Amount of AlfA and AlfB in each pellet were determined as the concentration of protein diminished from the load. (C) Negatively stained EM image of 3 µM AlfA and 15 µM AlfB were incubated in the presence of 5 mM AMPPNP and 5 mM $MgCl_2$.

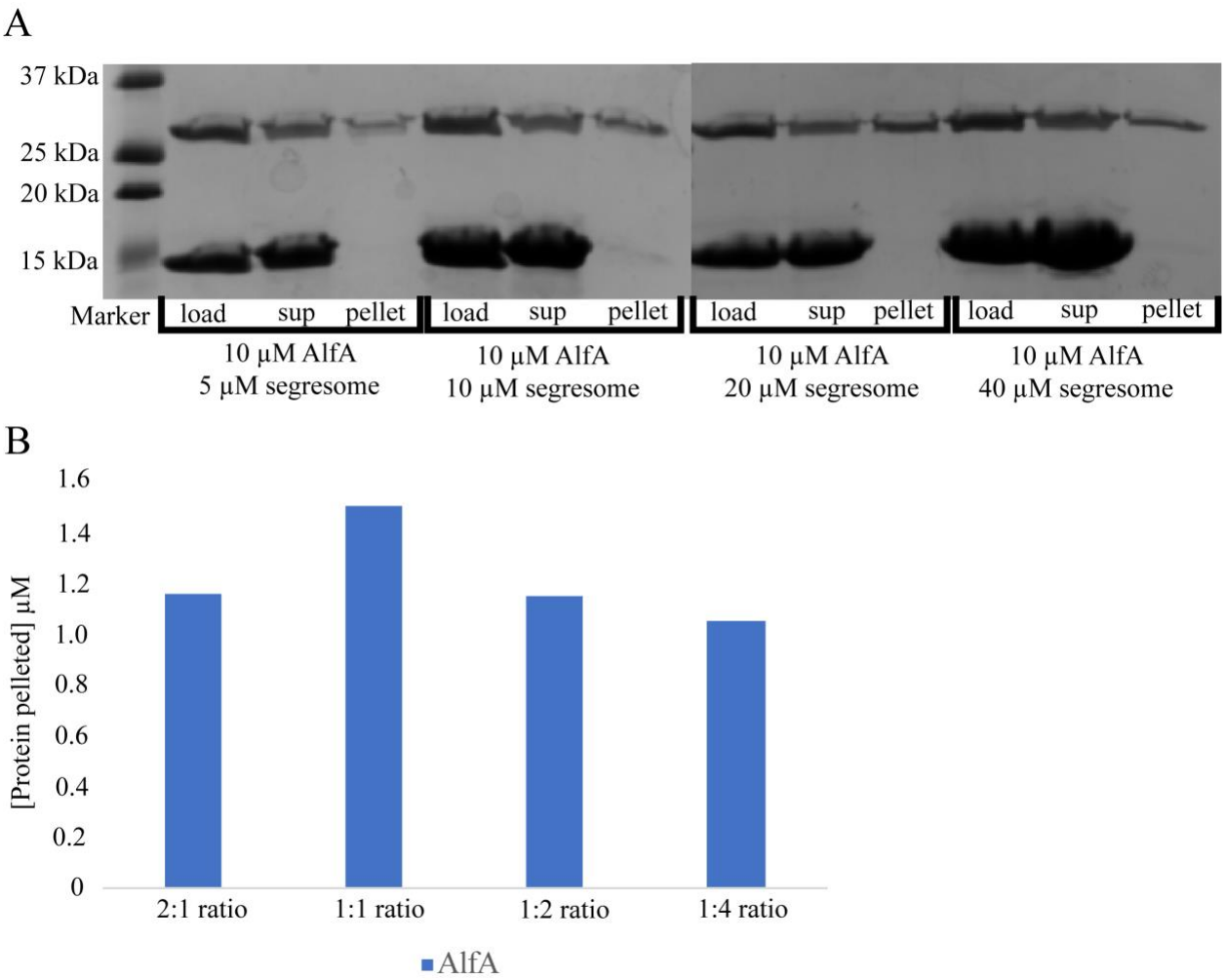

Figure 4.3: Segresome obstructs AlfA polymerization. AlfA polymerized in the presence of 5 mM AMPPNP, 5 mM $MgCl_2$ and various concentrations of segresome. (A) AlfA concentration has been kept constant (10 µM) while segresome concentration has been increased (5 µM, 10 µM, 20 µM and 40 µM) in the reaction mixtures. Samples were taken from pre-centrifuge reaction mixtures (load) and supernatants (sup) for SDS-PAGE analysis. Pellets were dissolved using depolymerization buffer and samples were taken for SDS PAGE analysis. (B) Amount of AlfA in each pellet were determined as the concentration of protein diminished from the load.

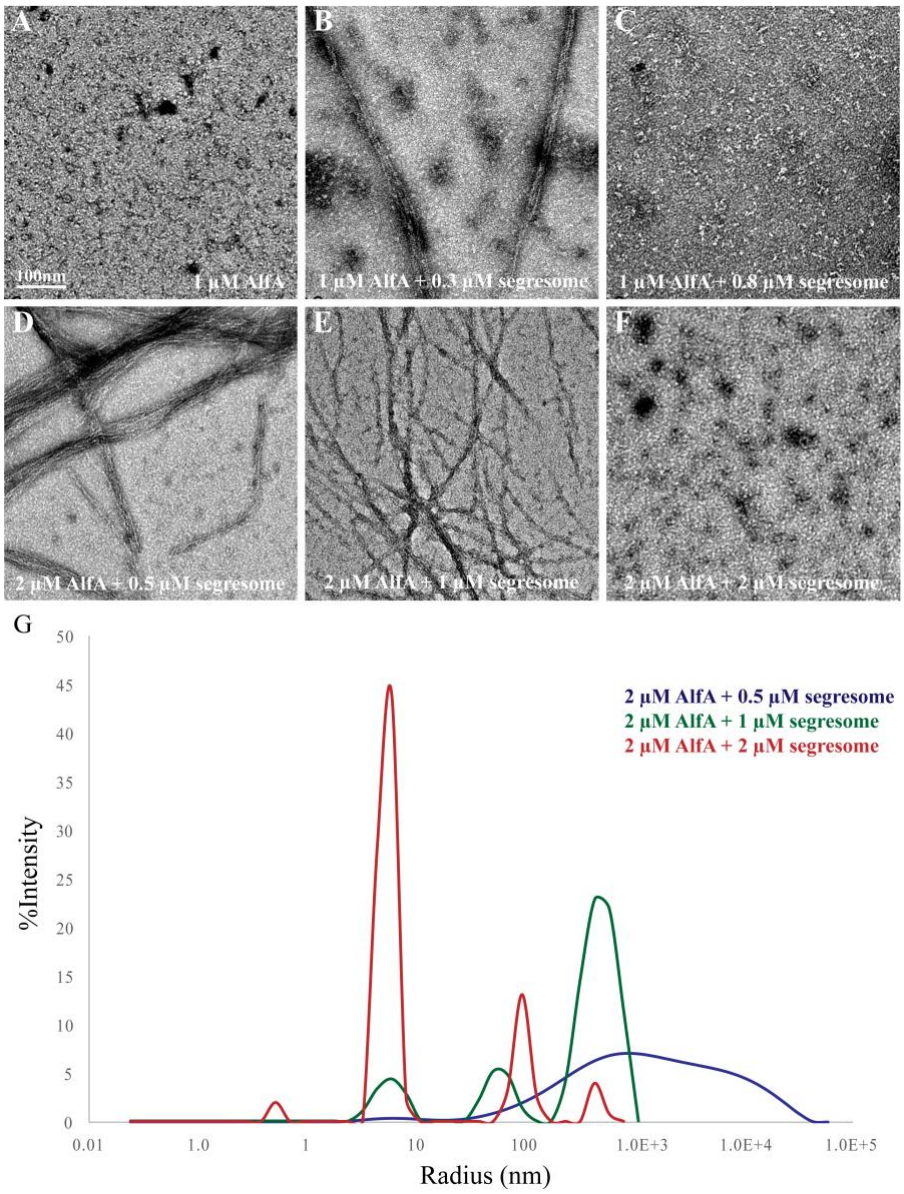

Figure 4.4: Increasing concentration of segresome can prevent AlfA polymerization. (A-C) AlfA has been titrated with segresome below critical concentration. (A) 1 µM AlfA does not yield any filaments in the presence of ATP. (B) When 0.3 µM segresome and 1 µM AlfA present in the reaction mixture, it has been observed that AlfA can form long AlfA bundles. (C) Adding 0.8 µM segresome in the reaction mixture that contains 1 µM AlfA prevented AlfA from forming filaments and yielded smaller, heterogenous particles. (D-G) AlfA concentration was increased to 2 µM to test the effects of segresome above the critical concentration by using EM and DLS. (D, G) When 2 µM AlfA was treated with 0.5 µM segresome, large bundles and particles with radii 100 nm-10 µm (dark blue) were observed. (E, G) Increasing the molar ratio of AlfA to segresome to 2:1 yielded smaller AlfA bundles and particles with radii smaller than 1 µM (blue). (F)The increase in segresome concentration cause AlfA filaments to get shorter and diminish at the equimolar ratio. (G) At the equimolar ratio of AlfA and segresome, we observed an increase in the particles with radii around 10 nm (light blue).

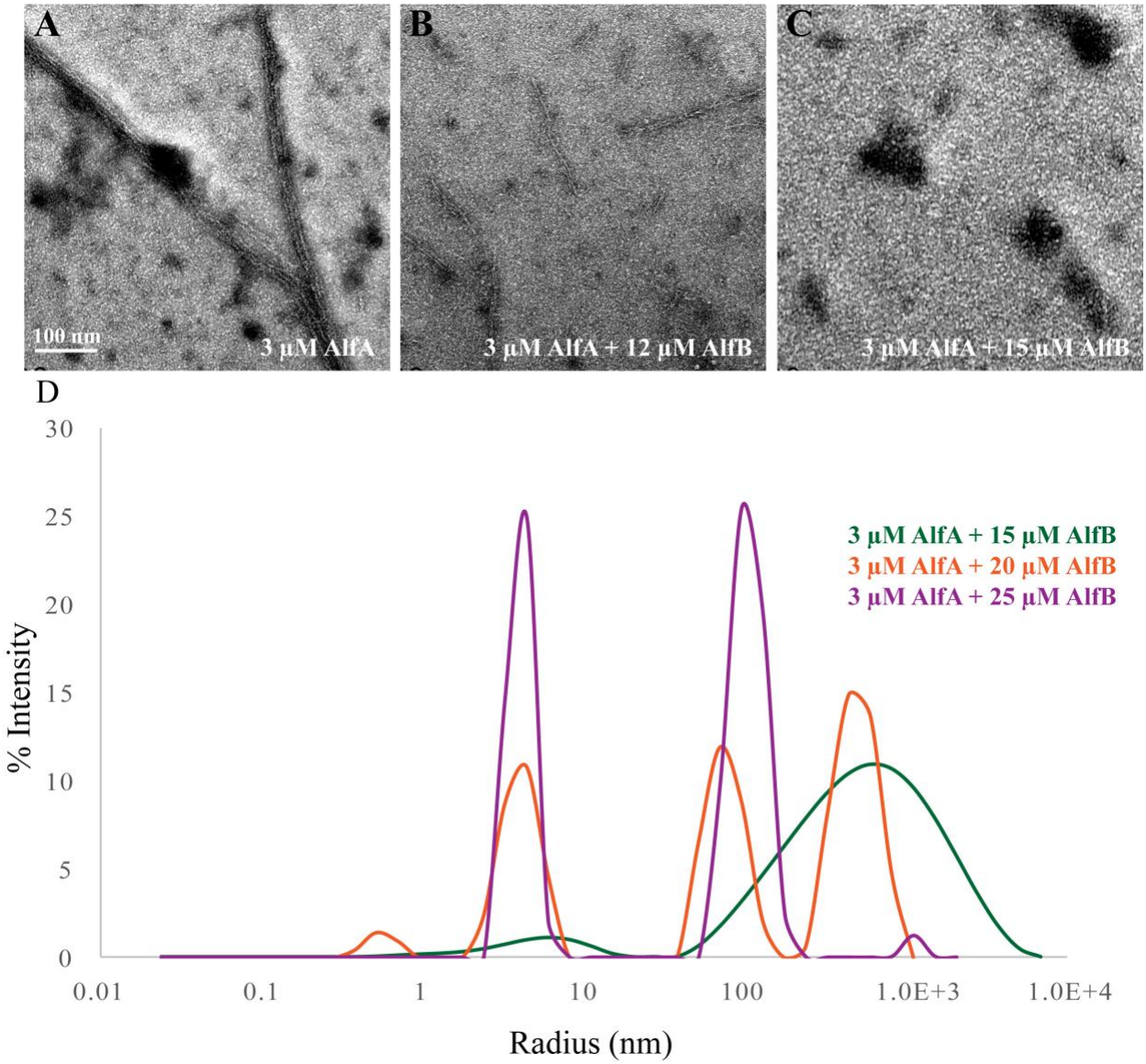

Figure 4.5: AlfB sequesters AlfA monomers to prevent polymerization. (A) 3 µM of AlfA forms filaments in the presence of ATP. (B) When 3 µM AlfA treated with 12 µM AlfB, it was observed that AlfA bundles to separate into individual short filaments. (C) Increasing AlfB concentration in the reaction mixture up to 15 µM caused AlfB to prevent filament formation. Same condition was tested for DLS experiment to ensure sequestering of AlfA. (D) Adding15 µM AlfB into reaction mixtures that contain 3 µM showed us that there are still particles in the mixture larger than 100 nm radii (dark green). After adding 20 µM (green) and 25 µM (light green) into reaction mixtures, particle size was decreased. However, a population composed of particles with radii around 100 nm was observed when 1 to 8 AlfA to AlfB ratio used.

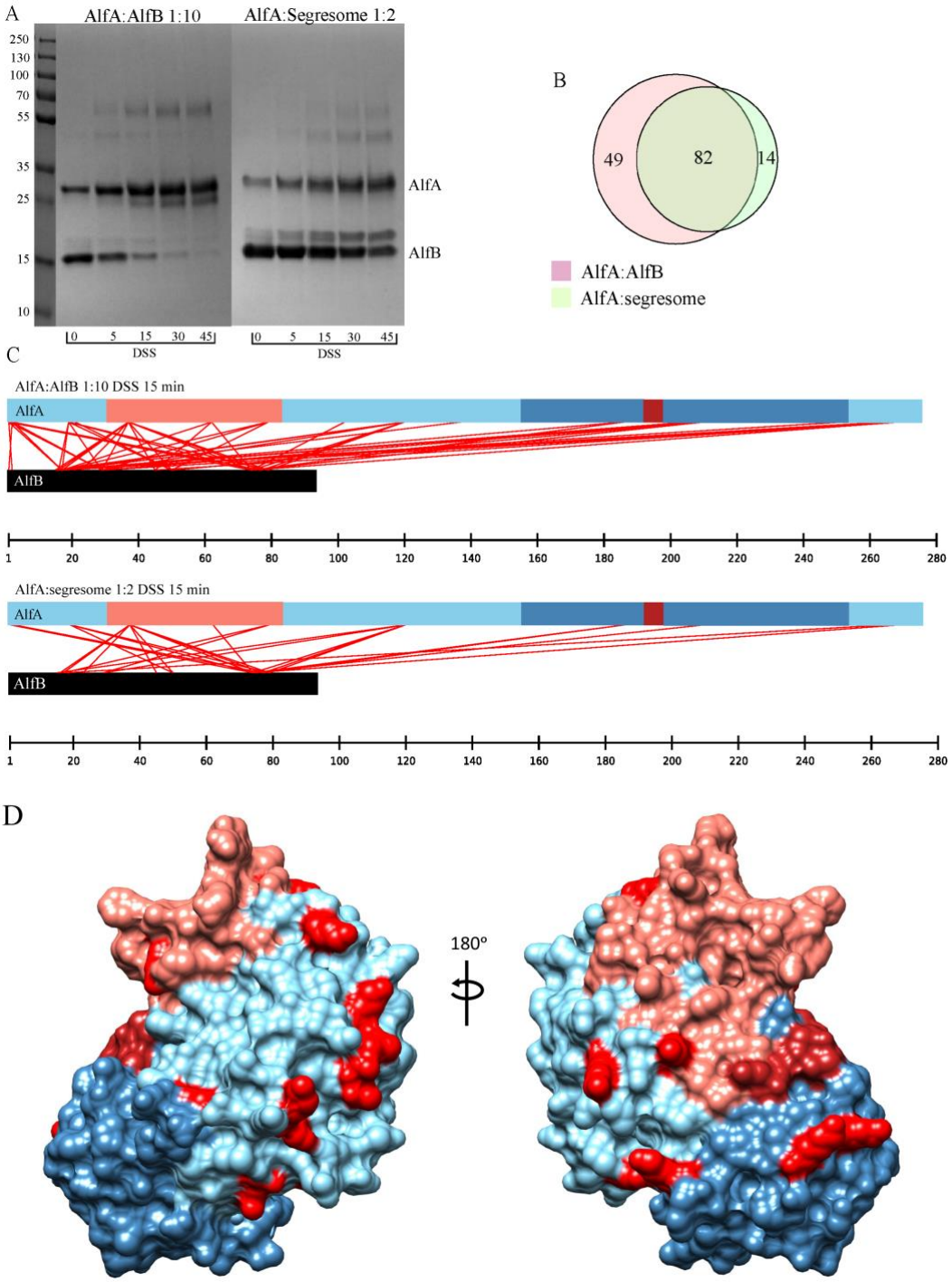

Figure 4.6: AlfA interacts with AlfB and segresome via the same surface. (A) 2 µM AlfA crosslinked with 20 µM AlfB and 4 µM segresome, respectively. 15-minute time point has been analyzed further by using MS. (B) 131 UDRs has been found in between AlfA and AlfB, while 96 UDR has been found in between AlfA and segresome. (C)All the subdomains of AlfA (Ia (light blue), Ib (salmon), (IIa, dark blue)) has been found as they crosslink with AlfB (black) as free dimer (top) and segresome (bottom). (D) Interaction surfaces in both case were found to be the same.

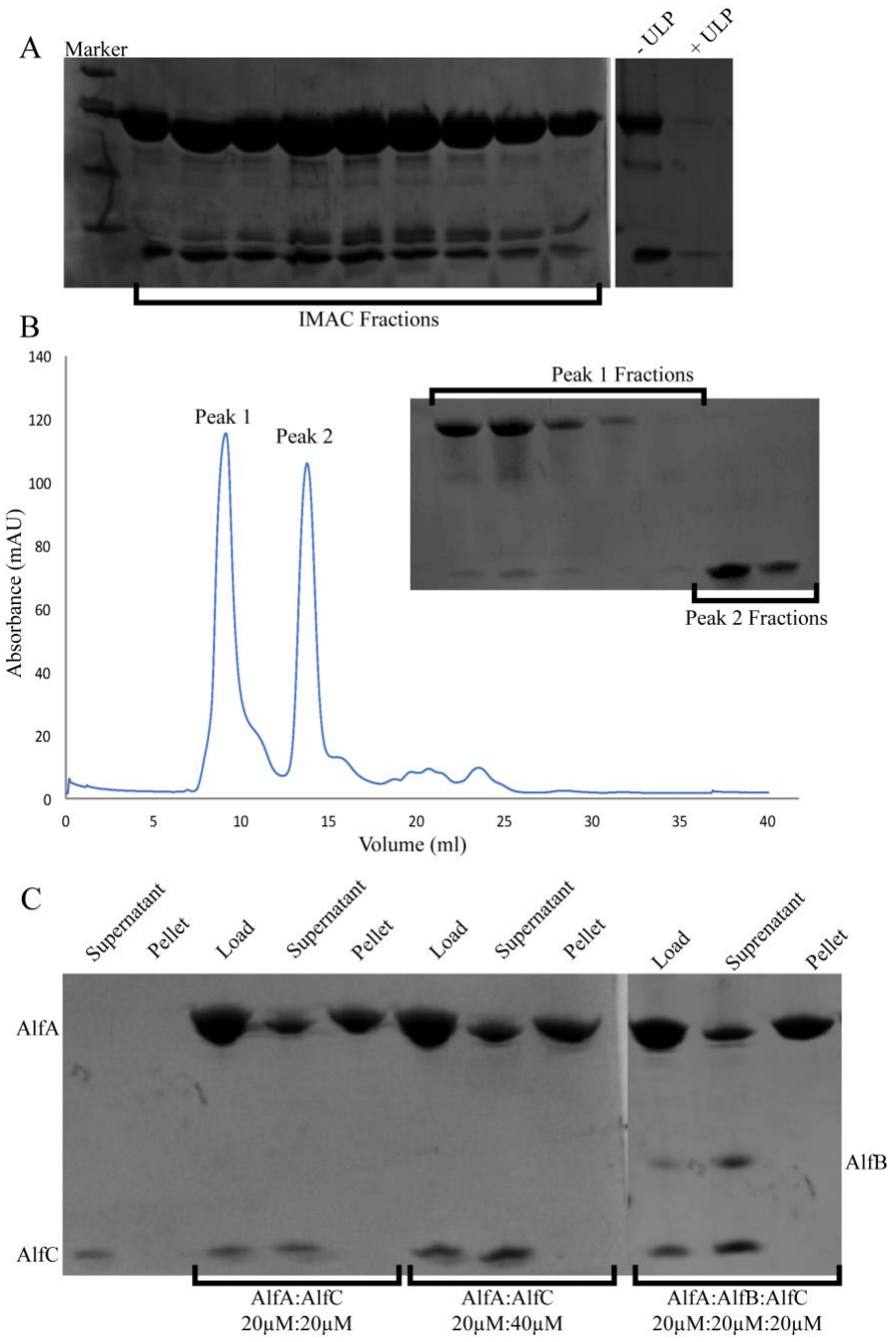

Figure 4.7: Purification of AlfC, the third protein of the *alf* operon, and its interactions with the other proteins of the segregation system. (A) AlfA polymerized in the presence of ATP, $MgCl_2$ and various concentrations of AlfC. AlfA concentration has been kept constant (10 μM) while AlfC concentration has been increased (5 μM and10 μM) in the reaction mixtures. Samples were taken from pre-centrifuge reaction mixtures (load) and supernatants (sup) for SDS-PAGE analysis. Pellets were dissolved using depolymerization buffer and samples were taken for SDS PAGE analysis. (B) AlfA polymerized in the presence of AlfB, AlfC, ATP and $MgCl_2$. Proteins were added at equimolar ratio into the raction mixture. Samples taken from load, supernatant and pellet were analyzed using SDS PAGE.

CONCLUSIONS AND FUTURE DIRECTIONS

Conclusions

By using various techniques in structural biology and biochemistry, we were able to obtain the single AlfA filament structure and understand its dynamics. We showed that AlfA is missing canonical actin subdomain IIB, and it uses a unique nucleotide binding mode and increased lateral interaction surface area to remain stable upon nucleotide hydrolysis. The filament structure suggests that AlfA filaments mainly grow from the barbed ends. By using predefined segresome complex and free AlfB, we gained more insight into the dual role that AlfB plays to regulate AlfA dynamics; nucleating AlfA filaments from plasmid DNA while simultaneously suppressing spontaneous nucleation. Sequestering of AlfA monomers by excess amounts of segresome complex and free AlfB suggested that AlfB might be utilizing the same interaction surface of AlfA in both the free and *parN*-bound form. Based on these results, we are able to propose a model for AlfA-driven plasmid segregation; the segresome complex nucleates AlfA filaments and filaments elongate unidirectionally from the barbed end via insertional polymerization. However, further investigation of the molecular details of segregation process is needed.

Future Directions

Even though high-resolution cryo-EM structures of single AlfA filaments were obtained and de novo atomic models were built for AlfA by using the cryo-EM data, a monomeric structure of AlfA can be obtained by using X-ray crystallography to improve the atomic accuracy of the filament models and explain the nature of lateral and longitudinal interactions between the protomers of the filament. It has been reported that attempts to crystallize AlfA yielded poorly diffracting crystals. Our model of the AlfA filament structure can be used to design mutations or deletions that might improve the quality of the crystals.

AlfA filaments stabilized by a non-hydrolysable analog of ATP showed that there is a stoichiometric interaction between AlfA filaments and AlfB. However, our direct observations of the AlfA filaments bound to AlfB by EM showed that the concentration range used in the experiment is not suitable for detecting any morphological changes in the AlfA filament structure. Samples prepared for that experiment can be diluted to prepare less crowded samples to obtain AlfA filaments interacting with AlfB and direct interaction of AlfA filaments with AlfB can be investigated by EM.

Using HDX-MS, we were able to detect a decrease in the solvent accessibility of the regions of AlfA that are involved in lateral and longitudinal interactions. This technique can be used to investigate the conformational changes at different stages of nucleotide binding and hydrolysis. AlfA mutant R78D K79D, which contains two cross-strand mutations that inhibit polymerization, can be utilized as a tool to investigate nucleotide dependent conformational changes using HDX-MS without the interference of filament assembly related conformational changes.

We decided to investigate AlfA-AlfB interactions at sequestering levels of both free AlfB and *parN*-bound AlfB using HDX-MS. We designed our experiments to parse out the changes in deuterium uptake levels of AlfA upon nucleotide binding, AlfB binding, and segresome binding. Since the sequestration by AlfB or the segresome requires the use of more than ten-fold molar excess of AlfB to AlfA, we could not detect peptides corresponding to AlfA due to suppression of AlfA peptide intensities by AlfB peptides (data not shown). As an alternative, non-polymerizing (R78D K79D) mutant of AlfA can be used at lower stoichiometric ratios since it prevents filament formation and the prevents the interference of the polymerization-related changes in the deuterium uptake levels. However, this requires a comparison of wild-type AlfA and non-polymerizing mutant by HDX-MS.

In parallel to investigation of AlfA-AlfB interactions by HDX-MS, we decided to use predefined segresome complexes to nucleate AlfA filaments and obtain AlfA filaments that are bound to the segresome complex to investigate interactions between AlfA and AlfB by using cryo-EM. We showed that AlfA is required to be below its critical concentration to ensure nucleation from segresomes, and using low concentrations of AlfA yielded suboptimal vitrified cryo-EM samples. Multiple rounds of sample application and blotting prior freezing can be used to obtain samples to investigate segresome-bound AlfA filament ends. On the other hand, we attempted to crystallize AlfB alone and co-crystallize AlfA with AlfB. Our initial screens did not yield crystals but we observed phase separation, which suggests that the screening conditions and protein concentrations can be optimized further.

It has been reported previously that AlfA filaments interact with each other in an antiparallel fashion and a structure of an AlfA doublet has been obtained at >10 Å resolution. However, recent advancements in cryo-electron tomography yielded structures at subnanometer resolution using subtomogram averaging, and this approach may prove useful in determining the structure of AlfA bundles.

Lastly, we made pelleting assays to detect assembly of AlfC into larger complexes, interactions of AlfC with the other protein components of the *alf* operon. Even though no direct interaction between the protein components of the system has been detected, the effects of AlfC on AlfA dynamics have not been investigated. A combination of EM and DLS experiments can be used to investigate the effects of AlfC on AlfA polymerization dynamics.

APPENDIX

Table 1: Cryo-EM data collection and refinement statistics

Data Collection and Refinement	Statistics
Data Collection	
Microscope	Titan Krios
Voltage (kV)	300
Detector	K2 summit, superresolution
Exposure ($e^-/Å^2$)	72
Frames per exposure	36
Pixel size (Å)	0.5
Defocus range (μm)	0.7-2.5
Reconstruction	
Refined helical rotation (°)	157.7
Refined helical rise (Å)	24.4
Helical segments	132,222
Resolution (0.143 FSC), Å	4.2
Model composition	
Protein residues	275
Ligands	1 (AMPPNP)
Model Statistics	
Clash score	7.77
Molprobity score	2.1
Ramachandran favored, %	84
Ramachandran outliers, %	6
Structure deposition	
EMDB ID (cryo-EM map)	EMD-7134
PDB ID (atomic model)	6BQW

Table 2: Fractions of micrographs containing polymer under different conditions

AlfA (μM)	Nucleotide	Wild-type (n)	F12A (n)
1.5	ATP	0.34 (245)	0 (109)
4.5	ATP	0.97 (74)	0.10 (231)
10	ATP	0.20 (97)	0 (225)
30	ADP	0.56 (160)	0 (131)

Table 3: AlfA peptides used for HDX-MS data analysis

Precursor MH+ (Da)	Charge (z)	Peak MW (Da)	Start	End	Sequence
1324.6912	2	1324.69	1	12	(-)MTLTTVIDIGNF(S)
1991.1066	2.94	1991.0983	13	29	(F)STKYAYKDKKQIKVGSF(P)
2544.1536	2.76	2544.1428	34	54	(L)HSYKPLEDYEGMERVEYNGLD(Y)
2129.0103	2.56	2129.0012	55	71	(D)YYVGETVKNFYFGREEQ(M)
2038.0219	2.91	2038.0133	72	88	(Q)MYFGNTRKGHMEGQIRL(V)
1944.093	2.55	1944.0864	93	108	(L)YTIFKETGKKEFNLIL(T)
830.307	1.01	830.3063	109	115	(L)TCPYESM(V)
3941.0728	4.65	3941.0728	116	148	(M)VTDKKYFVQHFEGEREVIVEGKSFKFTVHNIVM(A)
1581.7222	1.99	1581.7191	149	164	(M)AAEGLGALNFSDSLNC(V)
1215.6952	1.97	1215.6945	165	176	(C)VIVDAGSKTLNV(L)
2633.2666	2.79	2633.2556	180	204	(L)INGSISKMDSHTINGGTIDNSIMDL(A)
3428.614	3.64	3428.5996	205	235	(L)AKTFAKTCSNIDYDYPIVCTGGKAEEMKECL(E)
2131.9775	2.13	2131.9688	236	255	(L)ENVGYSTVSSAELGEDKPSY(Y)
2146.1472	2.92	2146.1382	256	273	(Y)YVNSVGLLLKYGRKFEEM(F)

Table 4: Plasmids used in this study

Name	Plasmid	Backbone/ Source	Reference
pJKP100	Codon-optimized AlfA	pET20b	Polka *et al.*, 2014
pJKP102	AlfA KK21AA KK101AA mutant	pET20b	Polka *et al.*, 2014
pJKP104	6His-AlfB	pETM11	Polka *et al.*, 2014
GU001	AlfA with F12A mutation	pET20b	This study
PJK008	AlfA R78D K79D mutant	pSMT3	This study
pJK054	AlfC	pSMT3	This study

Table 5: Oligos used in this study

Name	Sequence
parN	5’-aa**tttattta**agag**tttattta**aaaa**attattta**cg-3’
parN Repeat 1	5’-aa**tttattta**agag**tttattta**aaaa**tttattta**cg-3’
parN Repeat 2	5’-aa**attattta**agag**attattta**aaaa**attattta**cg-3’
AlfA F12A	5'-gtccttatatgcgtacttcgtagaggcgttaccaatatcaattacagtagtc-3'

Table 6: Proteins sequences of the *alf* segregation system

Protein	Sequence
AlfA	MTLTTVIDIG NFSTKYAYKD KKQIKVGSFP SILHSYKPLE DYEGMERVEY NGLDYYVGET VKNFYFGREE QMYFGNTRKG HMEGQIRLVY ALYTIFKETG KKEFNLILTC PYESMVTDKK YFVQHFEGER EVIVEGKSFK FTVHNIVMAA EGLGALNFSD SLNCVIVDAG SKTLNVLYLI NGSISKMDSH TINGGTIDNS IMDLAKTFAK TCSNIDYDYP IVCTGGKAEE MKECLENVGY STVSSAELGE DKPSYYVNSV GLLLKYGRKF EEMFA
AlfB	MSREDNFMYQ INWNKKKYPE ICKALEDAKN RTGGIAWYLR ELIQKDLEEK RGGVVRSTPV YETVDQEVQN DPPKPSKAKI ETIELPDDSGGFL
AlfC	MKIEIKEKDL LEIQDLIMRS YSFIKDGPVP ELEKELYETV HKIDRIIRNE E

BIBLIOGRAPHY

Austin, S. J. (1988). Plasmid partition. *Plasmid, 20*(1), 1-9.

Aylett, C. H., Wang, Q., Michie, K. A., Amos, L. A., & Lowe, J. (2010). Filament structure of bacterial tubulin homologue TubZ. *Proc Natl Acad Sci U S A, 107*(46), 19766-19771.

Bamburg, J. R., & Bernstein, B. W. (2010). Roles of ADF/cofilin in actin polymerization and beyond. *F1000 Biol Rep, 2*, 62.

Baxter, J. C., & Funnell, B. E. (2014). Plasmid Partition Mechanisms. *Microbiol Spectr, 2*(6).

Becker, E., Herrera, N. C., Gunderson, F. Q., Derman, A. I., Dance, A. L., Sims, J., . . . Pogliano, J. (2006). DNA segregation by the bacterial actin AlfA during Bacillus subtilis growth and development. *EMBO J, 25*(24), 5919-5931.

Bergeron, J. R., Hutto, R., Ozyamak, E., Hom, N., Hansen, J., Draper, O., . . . Kollman, J. M. (2017). Structure of the magnetosome-associated actin-like MamK filament at subnanometer resolution. *Protein Sci, 26*(1), 93-102.

Bharat, T. A., Murshudov, G. N., Sachse, C., & Lowe, J. (2015). Structures of actin-like ParM filaments show architecture of plasmid-segregating spindles. *Nature, 523*(7558), 106-110.

Bindschadler, M., & McGrath, J. L. (2004). Formin' new ideas about actin filament generation. *Proc Natl Acad Sci U S A, 101*(41), 14685-14686.

Bork, P., Sander, C., & Valencia, A. (1992). An ATPase domain common to prokaryotic cell cycle proteins, sugar kinases, actin, and hsp70 heat shock proteins. *Proc Natl Acad Sci U S A, 89*(16), 7290-7294.

Boratyn GM, et al. (2013) BLAST: A more efficient report with usability improvements. Nucleic Acids Res 41:W29–W33.

Campbell, C. S., & Mullins, R. D. (2007). In vivo visualization of type II plasmid segregation: bacterial actin filaments pushing plasmids. *J Cell Biol, 179*(5), 1059-1066.

Carballido-Lopez, R. (2006). The bacterial actin-like cytoskeleton. *Microbiol Mol Biol Rev, 70*(4), 888-909.

Chereau, D., Kerff, F., Graceffa, P., Grabarek, Z., Langsetmo, K., & Dominguez, R. (2005). Actin-bound structures of Wiskott-Aldrich syndrome protein (WASP)-homology domain 2 and the implications for filament assembly. *Proc Natl Acad Sci U S A, 102*(46), 16644-16649.

Cooper, J. A., & Schafer, D. A. (2000). Control of actin assembly and disassembly at filament ends. *Curr Opin Cell Biol, 12*(1), 97-103.

Couturier, M., Bex, F., Bergquist, P. L., & Maas, W. K. (1988). Identification and classification of bacterial plasmids. *Microbiol Rev, 52*(3), 375-395.

Derman, A. I., Becker, E. C., Truong, B. D., Fujioka, A., Tucey, T. M., Erb, M. L., . . . Pogliano, J. (2009). Phylogenetic analysis identifies many uncharacterized actin-like proteins (Alps) in bacteria: regulated polymerization, dynamic instability and treadmilling in Alp7A. *Mol Microbiol, 73*(4), 534-552.

Dominguez, R., & Holmes, K. C. (2011). Actin structure and function. *Annu Rev Biophys, 40*, 169-186.

dos Remedios, C. G., Chhabra, D., Kekic, M., Dedova, I. V., Tsubakihara, M., Berry, D. A., & Nosworthy, N. J. (2003). Actin binding proteins: regulation of cytoskeletal microfilaments. *Physiol Rev, 83*(2), 433-473.

Draper, O., Byrne, M. E., Li, Z., Keyhani, S., Barrozo, J. C., Jensen, G., & Komeili, A. (2011). MamK, a bacterial actin, forms dynamic filaments in vivo that are regulated by the acidic proteins MamJ and LimJ. *Mol Microbiol, 82*(2), 342-354.

Ebersbach, G., & Gerdes, K. (2005). Plasmid segregation mechanisms. *Annu Rev Genet, 39*, 453-479.

Egelman EH (2010) Reconstruction of helical filaments and tubes. Methods Enzymol 482:167–183.

Eng, J. K., Jahan, T. A., & Hoopmann, M. R. (2013). Comet: an open-source MS/MS sequence database search tool. *Proteomics, 13*(1), 22-24.

Errington, J. (2003). Dynamic proteins and a cytoskeleton in bacteria. *Nat Cell Biol, 5*(3), 175-178.

Errington, J., Daniel, R. A., & Scheffers, D. J. (2003). Cytokinesis in bacteria. *Microbiol Mol Biol Rev, 67*(1), 52-65.

Firat-Karalar, E. N., & Welch, M. D. (2011). New mechanisms and functions of actin nucleation. *Curr Opin Cell Biol, 23*(1), 4-13.

Galkin, V. E., Orlova, A., Rivera, C., Mullins, R. D., & Egelman, E. H. (2009). Structural polymorphism of the ParM filament and dynamic instability. *Structure, 17*(9), 1253-1264.

Garner, E. C., Campbell, C. S., & Mullins, R. D. (2004). Dynamic instability in a DNA-segregating prokaryotic actin homolog. *Science, 306*(5698), 1021-1025.

Garner, E. C., Campbell, C. S., Weibel, D. B., & Mullins, R. D. (2007). Reconstitution of DNA segregation driven by assembly of a prokaryotic actin homolog. *Science, 315*(5816), 1270-1274.

Gayathri, P., Fujii, T., Moller-Jensen, J., van den Ent, F., Namba, K., & Lowe, J. (2012). A bipolar spindle of antiparallel ParM filaments drives bacterial plasmid segregation. *Science, 338*(6112), 1334-1337.

Gayathri, P. (2017). Bacterial Actins and Their Interactors. *Curr Top Microbiol Immunol, 399*, 221-242.

Gerdes, K., Moller-Jensen, J., & Bugge Jensen, R. (2000). Plasmid and chromosome partitioning: surprises from phylogeny. *Mol Microbiol, 37*(3), 455-466.

Goddard, T. D., Huang, C. C., & Ferrin, T. E. (2007). Visualizing density maps with UCSF Chimera. *J Struct Biol, 157*(1), 281-287.

Gunning, P. W., Ghoshdastider, U., Whitaker, S., Popp, D., & Robinson, R. C. (2015). The evolution of compositionally and functionally distinct actin filaments. *J Cell Sci, 128*(11), 2009-2019.

Guttman, M., Kahn, M., Garcia, N. K., Hu, S. L., & Lee, K. K. (2012). Solution structure, conformational dynamics, and CD4-induced activation in full-length, glycosylated, monomeric HIV gp120. *J Virol, 86*(16), 8750-8764.

Guttman, M., Weis, D. D., Engen, J. R., & Lee, K. K. (2013). Analysis of overlapped and noisy hydrogen/deuterium exchange mass spectra. *J Am Soc Mass Spectrom, 24*(12), 1906-1912.

Hall, C. E., Jakus, M. A., & Schmitt, F. O. (1946). An investigation of cross striations and myosin filaments in muscle. *Biol Bull, 90*, 32-50.

He, S., & Scheres, S. H. W. (2017). Helical reconstruction in RELION. *J Struct Biol, 198*(3), 163-176.

Hellman, L. M., Fried, M. G. (2007). Electrophoretic mobility shift assay (EMSA) for detecting protein-nucleic acid interactions. *Nat Protoc, 2*(8), 1849-1861.

Heuser, J. E., & Kirschner, M. W. (1980). Filament organization revealed in platinum replicas of freeze-dried cytoskeletons. *J Cell Biol, 86*(1), 212-234.

Hussain, S., Wivagg, C. N., Szwedziak, P., Wong, F., Schaefer, K., Izore, T., . . . Garner, E. C. (2018). MreB filaments align along greatest principal membrane curvature to orient cell wall synthesis. *Elife, 7*.

Hussey, P. J., Ketelaar, T., & Deeks, M. J. (2006). Control of the actin cytoskeleton in plant cell growth. *Annu Rev Plant Biol, 57*, 109-125.

Huxley, A. F. (1974). Muscular contraction. *J Physiol, 243*(1), 1-43.

Howard, M., & Kruse, K. (2005). Cellular organization by self-organization: mechanisms and models for Min protein dynamics. *J Cell Biol, 168*(4), 533-536.

Izore, T., Duman, R., Kureisaite-Ciziene, D., & Lowe, J. (2014). Crenactin from Pyrobaculum calidifontis is closely related to actin in structure and forms steep helical filaments. *FEBS Lett, 588*(5), 776-782.

Izore, T., Kureisaite-Ciziene, D., McLaughlin, S. H., & Lowe, J. (2016). Crenactin forms actin-like double helical filaments regulated by arcadin-2. *Elife, 5*.

Jensen, R. B., & Gerdes, K. (1997). Partitioning of plasmid R1. The ParM protein exhibits ATPase activity and interacts with the centromere-like ParR-parC complex. *J Mol Biol, 269*(4), 505-513.

Jensen, R. B., Lurz, R., & Gerdes, K. (1998). Mechanism of DNA segregation in prokaryotes: replicon pairing by parC of plasmid R1. *Proc Natl Acad Sci U S A, 95*(15), 8550-8555.

Jiang, S., Narita, A., Popp, D., Ghoshdastider, U., Lee, L. J., Srinivasan, R., . . . Robinson, R. C. (2016). Novel actin filaments from Bacillus thuringiensis form nanotubules for plasmid DNA segregation. *Proc Natl Acad Sci U S A, 113*(9), E1200-1205.

Kabsch, W., Mannherz, H. G., Suck, D., Pai, E. F., & Holmes, K. C. (1990). Atomic structure of the actin:DNase I complex. *Nature, 347*(6288), 37-44.

Kabsch, W., & Holmes, K. C. (1995). The actin fold. *FASEB J, 9*(2), 167-174.

Kaltashov, I. A., Bobst, C. E., & Abzalimov, R. R. (2009). H/D exchange and mass spectrometry in the studies of protein conformation and dynamics: is there a need for a top-down approach? *Anal Chem, 81*(19), 7892-7899.

Katoh K, Misawa K, Kuma K, Miyata T (2002) MAFFT: A novel method for rapid multiple sequence alignment based on fast Fourier transform. Nucleic Acids Res 30: 3059–3066.

Kirschner, M. W. (1980). Implications of treadmilling for the stability and polarity of actin and tubulin polymers in vivo. *J Cell Biol, 86*(1), 330-334.

Kessner, D., Chambers, M., Burke, R., Agus, D., & Mallick, P. (2008). ProteoWizard: open source software for rapid proteomics tools development. *Bioinformatics, 24*(21), 2534-2536.

Komeili, A., Li, Z., Newman, D. K., & Jensen, G. J. (2006). Magnetosomes are cell membrane invaginations organized by the actin-like protein MamK. *Science, 311*(5758), 242-245.

Korn, E. D., Carlier, M. F., & Pantaloni, D. (1987). Actin polymerization and ATP hydrolysis. *Science, 238*(4827), 638-644.

Krissinel E, Henrick K (2007) Inference of macromolecular assemblies from crystalline state. J Mol Biol 372:774–797.

Lappalainen, P. (2016). Actin-binding proteins: the long road to understanding the dynamic landscape of cellular actin networks. *Mol Biol Cell, 27*(16), 2519-2522.

Larsen, R. A., Cusumano, C., Fujioka, A., Lim-Fong, G., Patterson, P., & Pogliano, J. (2007). Treadmilling of a prokaryotic tubulin-like protein, TubZ, required for plasmid stability in Bacillus thuringiensis. *Genes Dev, 21*(11), 1340-1352.

Lazarides, E., & Weber, K. (1974). Actin antibody: the specific visualization of actin filaments in non-muscle cells. *Proc Natl Acad Sci U S A, 71*(6), 2268-2272.

Lowe, J., He, S., Scheres, S. H., & Savva, C. G. (2016). X-ray and cryo-EM structures of monomeric and filamentous actin-like protein MamK reveal changes associated with polymerization. *Proc Natl Acad Sci U S A, 113*(47), 13396-13401.

Margolin, W. (2009). Sculpting the bacterial cell. *Curr Biol, 19*(17), R812-822.

Minehardt, T. J., Kollman, P. A., Cooke, R., & Pate, E. (2006). The open nucleotide pocket of the profilin/actin x-ray structure is unstable and closes in the absence of profilin. *Biophys J, 90*(7), 2445-2449.

Moller-Jensen, J., Borch, J., Dam, M., Jensen, R. B., Roepstorff, P., & Gerdes, K. (2003). Bacterial mitosis: ParM of plasmid R1 moves plasmid DNA by an actin-like insertional polymerization mechanism. *Mol Cell, 12*(6), 1477-1487.

Mossessova E, Lima CD (2000) Ulp1-SUMO crystal structure and genetic analysis reveal conserved interactions and a regulatory element essential for cell growth in yeast. Mol Cell 5:865–876.

Mullis, K. B. (1990). Target amplification for DNA analysis by the polymerase chain reaction. *Ann Biol Clin (Paris), 48*(8), 579-582.

Ohi M, Li Y, Cheng Y, Walz T (2004) Negative staining and image classification - Powerful tools in modern electron microscopy. Biol Proced Online 6:23–34.

Otto, J. J. (1994). Actin-bundling proteins. *Curr Opin Cell Biol, 6*(1), 105-109.

Ozyamak, E., Kollman, J., Agard, D. A., & Komeili, A. (2013). The bacterial actin MamK: in vitro assembly behavior and filament architecture. *J Biol Chem, 288*(6), 4265-4277.

Pan, W., Xie, C., & Lv, J. (2012). Screening for the interacting partners of the proteins MamK & MamJ by two-hybrid genomic DNA library of Magnetospirillum magneticum AMB-1. *Curr Microbiol, 64*(6), 515-523.

Pruyne, D., Legesse-Miller, A., Gao, L., Dong, Y., & Bretscher, A. (2004). Mechanisms of polarized growth and organelle segregation in yeast. *Annu Rev Cell Dev Biol, 20*, 559-591.

Polka, J. K., Kollman, J. M., Agard, D. A., & Mullins, R. D. (2009). The structure and assembly dynamics of plasmid actin AlfA imply a novel mechanism of DNA segregation. *J Bacteriol, 191*(20), 6219-6230.

Polka, J. K., Kollman, J. M., & Mullins, R. D. (2014). Accessory factors promote AlfA-dependent plasmid segregation by regulating filament nucleation, disassembly, and bundling. *Proc Natl Acad Sci U S A, 111*(6), 2176-2181.

Pollard, T. D., & Cooper, J. A. (1986). Actin and actin-binding proteins. A critical evaluation of mechanisms and functions. *Annu Rev Biochem, 55*, 987-1035.

Pollard, T. D. (2007). Regulation of actin filament assembly by Arp2/3 complex and formins. *Annu Rev Biophys Biomol Struct, 36*, 451-477.

Pollard, T. D., & Cooper, J. A. (2009). Actin, a central player in cell shape and movement. *Science, 326*(5957), 1208-1212.

Pollard, T. D. (2010). Mechanics of cytokinesis in eukaryotes. *Curr Opin Cell Biol, 22*(1), 50-56.

Pollard, T. D. (2016). Actin and Actin-Binding Proteins. *Cold Spring Harb Perspect Biol, 8*(8).

Popp, D., Narita, A., Ghoshdastider, U., Maeda, K., Maeda, Y., Oda, T., . . . Robinson, R. C. (2010). Polymeric structures and dynamic properties of the bacterial actin AlfA. *J Mol Biol, 397*(4), 1031-1041.

Popp, D., Xu, W., Narita, A., Brzoska, A. J., Skurray, R. A., Firth, N., . . . Schumacher, M. A. (2010). Structure and filament dynamics of the pSK41 actin-like ParM protein: implications for plasmid DNA segregation. *J Biol Chem, 285*(13), 10130-10140.

Roeben, A., Kofler, C., Nagy, I., Nickell, S., Hartl, F. U., & Bracher, A. (2006). Crystal structure of an archaeal actin homolog. *J Mol Biol, 358*(1), 145-156.

Rottner, K., & Stradal, T. E. (2011). Actin dynamics and turnover in cell motility. *Curr Opin Cell Biol, 23*(5), 569-578.

Sachse, C., Chen, J. Z., Coureux, P. D., Stroupe, M. E., Fandrich, M., & Grigorieff, N. (2007). High-resolution electron microscopy of helical specimens: a fresh look at tobacco mosaic virus. *J Mol Biol, 371*(3), 812-835.

Salje, J., Zuber, B., & Lowe, J. (2009). Electron cryomicroscopy of E. coli reveals filament bundles involved in plasmid DNA segregation. *Science, 323*(5913), 509-512.

Sept, D., & McCammon, J. A. (2001). Thermodynamics and kinetics of actin filament nucleation. *Biophys J, 81*(2), 667-674.

Schagger, H. (2006). Tricine-SDS-PAGE. *Nat Protoc, 1*(1), 16-22.

Schmidt, A., & Hall, M. N. (1998). Signaling to the actin cytoskeleton. *Annu Rev Cell Dev Biol, 14*, 305-338.

Schroeder, T. E. (1973). Actin in dividing cells: contractile ring filaments bind heavy meromyosin. *Proc Natl Acad Sci U S A, 70*(6), 1688-1692.

Schumacher, M. A., Glover, T. C., Brzoska, A. J., Jensen, S. O., Dunham, T. D., Skurray, R. A., & Firth, N. (2007). Segrosome structure revealed by a complex of ParR with centromere DNA. *Nature, 450*(7173), 1268-1271.

Schumacher, M. A. (2008). Structural biology of plasmid partition: uncovering the molecular mechanisms of DNA segregation. *Biochem J, 412*(1), 1-18.

Shaevitz, J. W., & Gitai, Z. (2010). The structure and function of bacterial actin homologs. *Cold Spring Harb Perspect Biol, 2*(9), a000364.

Song, Y., DiMaio, F., Wang, R. Y., Kim, D., Miles, C., Brunette, T., . . . Baker, D. (2013). High-resolution comparative modeling with RosettaCM. *Structure, 21*(10), 1735-1742.

Sonkaria, S., Fuentes, G., Verma, C., Narang, R., Khare, V., Fischer, A., & Faivre, D. (2012). Insight into the assembly properties and functional organisation of the magnetotactic bacterial actin-like homolog, MamK. *PLoS One, 7*(5), e34189.

Stetefeld, J., McKenna, S. A., & Patel, T. R. (2016). Dynamic light scattering: a practical guide and applications in biomedical sciences. *Biophys Rev, 8*(4), 409-427.

Straub FB (1942) Actin. *Stud Inst Med Chem Univ Szeged* II:3–15.

Straub, F. B., & Feuer, G. (1950). [Adenosine triphosphate, the functional group of actin]. *Kiserl Orvostud, 2*(2), 141-151.

Suloway C, et al. (2005) Automated molecular microscopy: The new Leginon system. J Struct Biol 151:41–60.

Szent-Gyorgyi, A. G. (2004). The early history of the biochemistry of muscle contraction. *J Gen Physiol, 123*(6), 631-641.

Szewczak-Harris, A., & Lowe, J. (2018). Cryo-EM reconstruction of AlfA from Bacillus subtilis reveals the structure of a simplified actin-like filament at 3.4-A resolution. *Proc Natl Acad Sci U S A, 115*(13), 3458-3463.

Szwedziak, P., Wang, Q., Freund, S. M., & Lowe, J. (2012). FtsA forms actin-like protofilaments. *EMBO J, 31*(10), 2249-2260.

Tan, Q., Awano, N., & Inouye, M. (2011). YeeV is an Escherichia coli toxin that inhibits cell division by targeting the cytoskeleton proteins, FtsZ and MreB. *Mol Microbiol, 79*(1), 109-118.

Tanaka, T. (2010). Functional analysis of the stability determinant AlfB of pBET131, a miniplasmid derivative of bacillus subtilis (natto) plasmid pLS32. *J Bacteriol, 192*(5), 1221-1230.

Taoka, A., Asada, R., Wu, L. F., & Fukumori, Y. (2007). Polymerization of the actin-like protein MamK, which is associated with magnetosomes. *J Bacteriol, 189*(23), 8737-8740.

Taylor, D. L., & Wang, Y. L. (1978). Molecular cytochemistry: incorporation of fluorescently labeled actin into living cells. *Proc Natl Acad Sci U S A, 75*(2), 857-861.

Zelter, A., Bonomi, M., Kim, J., Umbreit, N. T., Hoopmann, M. R., Johnson, R., . . . Davis, T. N. (2015). The molecular architecture of the Dam1 kinetochore complex is defined by cross-linking based structural modelling. *Nat Commun, 6*, 8673.

Zhang K (2016) Gctf: Real-time CTF determination and correction. J Struct Biol 193: 1–12.

Zhang, Z., Zhang, A., & Xiao, G. (2012). Improved protein hydrogen/deuterium exchange mass spectrometry platform with fully automated data processing. *Anal Chem, 84*(11), 4942-4949.

Zheng SQ, et al. (2017) MotionCor2: Anisotropic correction of beam-induced motion for improved cryo-electron microscopy. Nat Methods 14:331–332.

Umbreit, N. T., Miller, M. P., Tien, J. F., Ortola, J. C., Gui, L., Lee, K. K., . . . Davis, T. N. (2014). Kinetochores require oligomerization of Dam1 complex to maintain microtubule attachments against tension and promote biorientation. *Nat Commun, 5*, 4951.

von der Ecken, J., Heissler, S. M., Pathan-Chhatbar, S., Manstein, D. J., & Raunser, S. (2016). Cryo-EM structure of a human cytoplasmic actomyosin complex at near-atomic resolution. *Nature, 534*(7609), 724-728.

van den Ent, F., & Lowe, J. (2000). Crystal structure of the cell division protein FtsA from Thermotoga maritima. *EMBO J, 19*(20), 5300-5307.

van den Ent, F., Amos, L. A., & Lowe, J. (2001). Prokaryotic origin of the actin cytoskeleton. *Nature, 413*(6851), 39-44.

van den Ent, F., Moller-Jensen, J., Amos, L. A., Gerdes, K., & Lowe, J. (2002). F-actin-like filaments formed by plasmid segregation protein ParM. *EMBO J, 21*(24), 6935-6943.

Wang, R. Y., Song, Y., Barad, B. A., Cheng, Y., Fraser, J. S., & DiMaio, F. (2016). Automated structure refinement of macromolecular assemblies from cryo-EM maps using Rosetta. *Elife, 5*.

Weis, D. D., Engen, J. R., & Kass, I. J. (2006). Semi-automated data processing of hydrogen exchange mass spectra using HX-Express. *J Am Soc Mass Spectrom, 17*(12), 1700-1703.

Westermann, S., Wang, H. W., Avila-Sakar, A., Drubin, D. G., Nogales, E., & Barnes, G. (2006). The Dam1 kinetochore ring complex moves processively on depolymerizing microtubule ends. *Nature, 440*(7083), 565-569.